



**LIBRARY  
Michigan State  
University**

This is to certify that the  
dissertation entitled

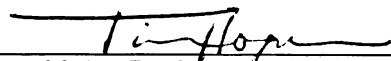
**FABRICATION AND SITE SPECIFIC GROWTH OF  
NANOWIRES**

presented by

**CHUN-I WU**

has been accepted towards fulfillment  
of the requirements for the

Ph.D. degree in Electrical Engineering



Major Professor's Signature

4/14/06

Date



**PLACE IN RETURN BOX** to remove this checkout from your record.  
**TO AVOID FINES** return on or before date due.  
**MAY BE RECALLED** with earlier due date if requested.

DATE DUE	DATE DUE	DATE DUE
JUN 21 2007	JAN 22 2008	

**FABRICATION AND SITE SPECIFIC GROWTH OF NANOWIRES**

**By**

**Chun-I Wu**

**A DISSERTATION**

**Submitted to  
Michigan State University  
in partial fulfillment of requirements  
for the degree of**

**DOCTOR OF PHILOSOPHY**

**Department of Electrical and Computer Engineering**

**2006**

**ABSTRACT**

**FABRICATION AND SITE SPECIFIC GROWTH OF**

**NANOWIRES**

**By**

**Chun-I Wu**

Nanotechnology has the promise to affect many areas of study including structural, materials, biological, and electrical sensors and circuits. In this presentation, fabrication routes to growing whiskers and nanowires of various materials will be presented. The materials investigated include gallium arsenide (GaAs), indium antimonide (InSb), a clathrate material  $\text{Sr}_8\text{Ga}_{16}\text{Ge}_{30}$ , and germanium (Ge). The experiments were designed to utilize the vapor-liquid-solid (VLS) growth mechanism, where a metal catalyst is used to mitigate the growth of the nanowires. The results for germanium, however, show a strong enhancement of growth upon the exposure of the samples to air while at the growth temperature. The role of oxide assisted (OA) growth in combination with the VLS mechanism will be discussed.

Nanowires of GaAs, InSb, and  $\text{Sr}_8\text{Ga}_{16}\text{Ge}_{30}$  showed compositions that were deficient in the more volatile elements. Volume confinement studies will also be presented for the clathrate material.

Growth of germanium dioxide ( $\text{GeO}_2$ ) whiskers and nanowires was found to be highly selective to the locations of the metal catalyst (gold). Examples of site specific growth of the  $\text{GeO}_2$  wires will be presented to show nanobridges on silicon substrates, and nanowire bundles inside tapered micropipette structures. The growth technique is relatively simple, and applicable for scaleup procedures. Images of the whiskers and nanowires were taken with SEM and TEM.

Copyright by  
Chun-I Wu  
2006



**To my parents and my sisters.**

## **ACKNOWLEDGEMENTS**

I would like to express my sincere gratitude to my advisor, Dr. Tim Hogan. This work won't have been possible without his guidance, constant encouragement and continuing support. Besides academics, his goodness, dedication, honesty and equal respect for everyone have deeply moved me. I would also like to thank my committee members, Dr. Ayres, Dr. Grotjohn, and Dr. Fan for their valuable comments on the project.

Finally I would like to express my gratitude to my parents and family members for their patience, unconditional support and confidence in my abilities.

# TABLE OF CONTENTS

<b>LIST OF TABLES.....</b>	<b>ix</b>
----------------------------	-----------

<b>LIST OF FIGURES.....</b>	<b>x</b>
-----------------------------	----------

<b>Introduction.....</b>	<b>1</b>
--------------------------	----------

## **Chapter 1 Theory**

1.1 Different growth method.....	6
1.1.1 Chemical vapor deposition.....	6
1.1.2 Physical Vapor Deposition.....	9
1.2 Pulsed Laser Deposition.....	25
1.2.1 History and Fundamental of pulsed laser deposition.....	25
1.2.2 Pulsed Laser Deposition: Mechanisms of Ablation.....	27
1.2.2.1 Collisional.....	31
1.2.2.2 Thermal Evaporation .....	32
1.2.2.3 Electronic sputtering .....	33
1.2.2.4 Exfoliation.....	34
1.2.2.5 Hydrodynamic Sputtering .....	35
1.2.3 Particulates Generate By Pulsed Laser Deposition.....	38
1.3 Thermodynamics and Chemical potential.....	43
1.3.1 Binary solution.....	46
1.3.1.1 The Gibbs Free Energy of Binary Solutions.....	47
1.3.2 Chemical potential .....	48
1.4 Growth mechanism .....	50
1.4.1 Vapor-Liquid-Solid (VLS) growth mechanism .....	50
1.4.2 Solid-liquid-solid .....	57
1.4.3 Oxide-Assisted Growth .....	58
1.5 Vacuum Sciences.....	60
1.5.1 Rate at Which Molecules Strikes a Surface.....	62
1.5.2 Ideal Gas Law Pressure.....	65
1.6 Gas Flow and Conductance.....	71

## **Chapter 2 Growth of III-V Semiconductor Nanowires (GaAs)**

2.1 Introduction.....	73
2.2 Experiments.....	74
2.3 Discussion.....	99
2.4 Conclusion.....	102

## **Chapter 3 Growing nanowires from $\text{Sr}_8\text{Ga}_{16}\text{Ge}_{30}$**

3.1 Introduction.....	103
3.2 Experiments.....	104

3.3 Discussion.....	123
<b>Chapter 4 Growth nanowires from germanium</b>	
4.1 Introduction.....	125
4.2 Experiments.....	127
4.3 Theory.....	155
4.4 Discussion.....	157
4.5 Conclusion.....	157
<b>Chapter 5 Gold Pattern experiment</b>	
5.1 Introduction.....	159
5.2 Experiment.....	160
5.3 Gold Deposited at Room Temperature.....	160
5.4 Gold Deposited at High Temperature.....	165
5.5 Conclusion.....	170
<b>Chapter 6 Nanobridge</b>	
6.1 Introduction.....	172
6.2 Experiments.....	174
6.3 Conclusion.....	189
<b>Chapter 7 Conclusions.....</b>	<b>190</b>
<b>Chapter 8 Scanning Electron Microscope.....</b>	<b>193</b>
<b>Chapter 9 System Set Up.....</b>	<b>207</b>
<b>Appendix A.....</b>	<b>213</b>
<b>Appendix B.....</b>	<b>217</b>
<b>Appendix C.....</b>	<b>218</b>
<b>Appendix D.....</b>	<b>219</b>
<b>References.....</b>	<b>223</b>

# LIST OF TABLES

## Chapter 1

Table 1. Qualitative comparison of deposition rates of various growth techniques [31] ...	8
Table 2. Experimental values for the binding energy, $E_{des}$ , and the activation energy for diffusion, $E_s$ , for some typical systems.....	13
Table 3. Temperature of melting, Boiling, and a Vaporization Rate of 1 nm/pulse for Selected Solids. [31] .....	33
Table 4. Quantities needed for evaluating thermal stress by means of Equation 5 [31]...	34
Table 5. The different shape and size between the three phases.....	39

## Appendix

Table 6. Properties of quartz tube .....	213
Table 7. Specifications for Lambda Physik 210i KrF Excimer Laser .....	214
Table 8. Beam box specifications .....	214
Table 9. Specifications for the optical window .....	215
Table 10. Specification for the plano-convex lens.....	215
Table 11. Specification for the high power UV laser mirror .....	216
Table 12. Specifications for the aluminum optics stand .....	216
Table 13. Calculated Concentrations and Associated Etch Rates.....	220



# LIST OF FIGURES

## Chapter 1

Figure 1. Chemical vapor deposition process .....	7
Figure 2. Schematic of film surface with various edges, pits, and clusters identified.....	10
Figure 3. Free-energy change ( $\Delta G$ ) as a function of cluster ( $r^* > r$ ) or stable nucleus ( $r > r^*$ ) size. $r^*$ is critical nucleus size, and $\Delta G^*$ is critical free-energy barrier for nucleation. ....	15
Figure 4. Total free energy (surface plus volume free energies) of cluster formation vs. size ( $r$ ) for different supersaturations ( $S$ ). ....	17
Figure 5. Schematic representation of three film growth modes. $\theta$ is the overlayer coverage in monolayers (ML).....	18
Figure 6. Schematic of basic atomistic processes on substrate surface during vapor deposition. ....	19
Figure 7. Schematic representation of MBE deposition of a thin film. The film thickness and composition is defined by controlling the individual fluxes.....	21
Figure 8. A schematic representation of the sputtering process. ....	23
Figure 9. Formation of cone structures during laser ablation, indicating a collisional interaction of particles with the target surface. ....	31
Figure 10. Droplet formation in the gold target. Sputtering of polycrystalline Au in air after 4320 pulses from an ArF excimer laser (193nm) of 12 ns and $2.5\text{J}/\text{cm}^2$ . (From Kelly et al. 1985).....	35
Figure 11. Plasma gas-dynamic expansion [31]. ....	36
Figure 12. Laser produced plasma plume from a metal target [32]. ....	37
Figure 13. Variation of Gibbs free energy with the arrangement of atoms. Schematically, the configuration G2 has the lowest free energy which results in a system that is at stable equilibrium. The configuration G1 is a metastable equilibrium. .	45
Figure 14. Variation of $G_1$ (the free energy before mixing) with alloy composition. ....	47
Figure 15. Phase diagram for the gold-silicon system. ....	52

Figure 16. Gold droplets form an alloy with the silicon. The alloy has a eutectic point near 360°C, above which it is molten. ....	55
Figure 17. All directions of molecular velocities are consistently probable.....	63
Figure 18. A vector always represents the direction and the magnitude of its velocity. ..	63
 <b>Chapter 2</b>	
Figure 19. Nanowires grown from a piece of GaAs. The scale bar is 500 nm. ....	75
Figure 20. The nanowires grew from the GaAs chunk. The scale bar is 5µm.....	76
Figure 21. These nanowires were a few microns in length. The scale bar is 2 µm. ....	77
Figure 22. The nanowires grew from the edge. The scale bar is 2µm.....	78
Figure 23. Histogram showing the diameter of nanowires. Total sample size: 42. Average Diameter: 65 nm.....	79
Figure 24. Histogram showing the height distribution of nanowires. Total sample size : 42. Average length of the nanowire is 2.7 µm. ....	80
Figure 25. The EDS analysis of nanowire .....	81
Figure 26. Under these fabrication conditions, a very high density of nanowires formed. The scale bar is 20 µm. ....	83
Figure 27. The diameters of these nanowires were uniform. The scale bar is 5 µm. ....	84
Figure 28. This zoom-out image illustrates that nanowires connected with each other in order to form a wool-like structure. Nonetheless, there was no gallium arsenide chunk left inside this structure.....	84
Figure 29. The nanowires formed a thick layer on top of the GaAs chunk.....	85
Figure 30. The SEM image shows nanowires. In addition, the same image illustrates that the gallium arsenide surface was underneath the layer of nanowires and there were some nanowires left on the surface. The length of nanowires was tens of microns. The scale bar is 5 µm. ....	86
Figure 31. EDS analysis on the grown gallium oxide nanowires. ....	87
Figure 32. Histogram showing the diameter distribution of the nanowires. The average diameter is 81 nm.....	88

Figure 33. The SEM image shows the nanowires grew on the piece of gallium arsenide. These nanowires were a few microns in length. The scale bar is 10 $\mu\text{m}$ .....	89
Figure 34. The SEM image shows the nanowires grew on top of gallium arsenide chunk. ....	90
Figure 35. The SEM image show the nanowires grew on top of gallium arsenide chunk. The scale bar is 2 $\mu\text{m}$ . ....	91
Figure 36. Histogram showing the diameter of nanowires. Total sample size: 40. ....	92
Figure 37. EDS analysis on the grown gallium oxide nanowires .....	93
Figure 38. The SEM image of a piece of GaAs. No gold was deposited on this sample before growth. ....	94
Figure 39. TEM image shows nanowire grown from GaAs .....	95
Figure 40. TEM image shows nanowire grown from GaAs .....	96
Figure 41. TEM image shows nanowire grown from GaAs .....	97
Figure 42. EDS analysis of nanowires .....	98

### Chapter 3

Figure 43. The $\text{Sr}_8\text{Ga}_{16}\text{Ge}_{30}$ structure. In the framework, the black atoms occupy the 6c sites, the light gray atoms occupy the 16i sites, and the dark gray atoms occupy the 24k sites. In the cavities, the gray atoms are at the Sr(1) 2a sites and the black atoms are at the Sr(2) 24k sites [51]. ....	103
Figure 44. The SEM image shows that nanowires were scattered on the surface of $\text{Sr}_8\text{Ga}_{16}\text{Ge}_{30}$ powders. The scale bar is 5 $\mu\text{m}$ . ....	105
Figure 45. The SEM image shows that the dark region is a quartz plate. The scale bar is 2 $\mu\text{m}$ . ....	106
Figure 46. The SEM image shows that nanowires were mostly scattered on the top surface of the $\text{Sr}_8\text{Ga}_{16}\text{Ge}_{30}$ powder. The scale bar is 5 $\mu\text{m}$ . ....	106
Figure 47. Histogram showing the diameter of nanowires. Total sample size: 22. Average diameter is 52 nm. ....	107
Figure 48. EDS analysis on the nanowires grew on $\text{Sr}_8\text{Ga}_{16}\text{Ge}_{30}$ .....	108
Figure 49. The SEM image shows the nanowires around the $\text{Sr}_8\text{Ga}_{16}\text{Ge}_{30}$ powder. ....	110

Figure 50. The nanowires scattered around the $\text{Sr}_8\text{Ga}_{16}\text{Ge}_{30}$ powders. ....	110
Figure 51. The SEM image shows the distinctive structure of the nanowires.....	111
Figure 52. The average diameter was 40 nm and the average length was 1.5 $\mu\text{m}$ . ....	112
Figure 53. The average diameter of nanowires was about 100 nm.....	112
Figure 54. Histogram showing the diameter of nanowires. Total sample size: 36. The average diameter is 62.22 nm. ....	113
Figure 55. EDS analysis on the grown nanowires .....	114
Figure 56. The length of nanowire was over 4 $\mu\text{m}$ . Additionally, some nanowires were observed to form as a ball shape in the tip.....	116
Figure 57. The diameter of nanowires ranged from 40 nm to 200 nm. The scale bar is 500 nm. ....	116
Figure 58. Nanowires on top of the quartz plate. The scale bar is 2 $\mu\text{m}$ . ....	117
Figure 59. The dark region is the quartz plate. The scale bar is 2 $\mu\text{m}$ . ....	118
Figure 60. The scale bar is 10 $\mu\text{m}$ .....	118
Figure 61. Histogram showing the diameter of nanowires. Total sample size: 36. Average diameter 43 nm.....	119
Figure 62. The diameter was about 60 nm and the length was about 1.5 $\mu\text{m}$ .....	120
Figure 63. The diameter was about 40 nm.....	120
Figure 64. The density of these nanowires was uniformly distributed over the quartz substrate. ....	121
Figure 65. The length was about 2 $\mu\text{m}$ and the diameter was about 120 nm.....	122
Figure 66. The scale bar is 20 $\mu\text{m}$ . ....	122
Figure 67. Histogram showing the diameter of nanowires. Total sample size: 42. Average diameter is 55.24 nm.....	123

## Chapter 4

Figure 68. The experimental setup, for investigating the growth of $\text{GeO}_2$ nanowires. .	128
Figure 69. The SEM image shows the edge of the gold coin. The scale bar is 200 $\mu\text{m}$ .	129

Figure 70. The SEM image of nanowires on the surface of gold coin. The scale bar is 10 $\mu\text{m}$ . .....	130
Figure 71. The SEM image shows the whiskers at the edge. The scale bar is 2 $\mu\text{m}$ . ....	131
Figure 72. The whiskers with kinked shape. The scale bar is 2 $\mu\text{m}$ . .....	131
Figure 73. Away from the observed area, no nanowires were observed. ....	132
Figure 74. EDS analysis on the nanowires. ....	133
Figure 75. The silicon wafer was covered with dense germanium oxide nanowires.....	135
Figure 76. The growth of nanowires on the edge of a silicon wafer. The scale bar is 10 $\mu\text{m}$ . ....	136
Figure 77. The gold balls were appeared at the tip of nanowires. The scale bar is 5 $\mu\text{m}$ . ....	137
Figure 78. The image of a nanowire at a higher magnification (1 $\mu\text{m}$ scalebar).....	138
Figure 79. EDS analysis on the nanowires. ....	139
Figure 80. The silicon wafer only partially covered by nanowires (1mm scalebar).....	141
Figure 81. A closeup image of a scratched region showing that the growth of nanowires only occurred in the gold coated areas. The scalebar is 10 $\mu\text{m}$ .....	141
Figure 82. The dense of nanowires were observed on the surface of silicon wafer. The scale bar is 5 $\mu\text{m}$ . ....	142
Figure 83. Histogram showing the diameter of nanowires. Total sample size: 20. The average diameter is 285 nm. ....	143
Figure 84. EDS analysis on the grown nanowires. ....	144
Figure 85. The image of the sample set. ....	146
Figure 86. No growth happened in the “S” (1mm scale bar).....	147
Figure 87. Dark region is no gold zone. The scale bar is 20 $\mu\text{m}$ . ....	148
Figure 88. Nanowires extending into no gold zone. The scale bar is 5 $\mu\text{m}$ .....	148
Figure 89. The nanowires had a bright dot at tip (1 $\mu\text{m}$ scalebar). ....	149



Figure 90. Dense nanowires grown onto the surface (5 $\mu\text{m}$ scalebar).....	150
Figure 91. Higher magnification SEM image of nanowires (2 $\mu\text{m}$ scalebar).....	150
Figure 92. SEM EDS analysis on the nanowires. ....	151
Figure 93. TEM image shows the gold ball at the tip of the nanowires (0.2 $\mu\text{m}$ scalebar)..	152
Figure 94. TEM image shows the nanowires have diameter about 40 nm (0.2 $\mu\text{m}$ scalebar).....	153
Figure 95. TEM image shows the nanowires have diameter about 65 nm (20 nm scalebar).....	153
Figure 96. TEM image shows the gold ball at tip of nanowires (20 nm scalebar). ....	154
Figure 97. Selected area electron diffraction (SAED) pattern of nanowires. ....	154

## Chapter 5

Figure 99. The darker location is Si and the lighter locations are $\text{SiO}_2$ . The scale bar is 20 $\mu\text{m}$ . ....	161
Figure 100. The area identified in this image is near the edge of the half-circle pattern. The scale bar is 2 $\mu\text{m}$ . ....	161
Figure 101. The image is near the edge of the half-circle pattern. The darker location is Si and the lighter locations are $\text{SiO}_2$ . The scale bar is 2 $\mu\text{m}$ . ....	162
Figure 102. The image is inside the pattern. The background is Si. and the white dots are Au. The scale bar is 1 $\mu\text{m}$ . ....	162
Figure 103. The dark part is Si and the light ball is Au. This area is inside the pattern. The scale bar is 10 $\mu\text{m}$ . ....	162
Figure 104. This is a half-circle pattern. The white chunk is silicon. The scale bar is 20 $\mu\text{m}$ . ....	162
Figure 105. The average diameter of the Au balls was 100 nm. The scale bar is 1 $\mu\text{m}$ . ....	163
Figure 106. This is a half-circle pattern. The scale bar is 20 $\mu\text{m}$ .....	163
Figure 107. The darker location is Si and the lighter locations are $\text{SiO}_2$ .....	163
Figure 108. 10.5 nm of sputter deposited Au followed by an annealing at 700° C for 5 mins. The scale bar is 10 $\mu\text{m}$ . ....	163

Figure 109. The image is near the edge of the half-circle pattern. The scale bar is 2 $\mu\text{m}$ .....	164
Figure 110. The image is near the edge of the half-circle pattern. The scale bar is 2 $\mu\text{m}$ .....	164
Figure 111. The image is near the edge of the pattern. The dark location is Si and white dots are Au. The scale bar is 2 $\mu\text{m}$ .....	164
Figure 112. The dark location is Si. The scale bar is 5 $\mu\text{m}$ .....	164
Figure 113. The Au ball was observed to be in the gap as a bridge. The scale bar is 10 $\mu\text{m}$ . ....	165
Figure 114. The area in this image is in the edge of pattern. The scale bar is 10 $\mu\text{m}$ ....	165
Figure 115. The SEM image shows the square pattern. The scale bar is 50 $\mu\text{m}$ . ....	166
Figure 116. The SEM image shows the edge of pattern. The scale bar is 2 $\mu\text{m}$ .....	166
Figure 117. The Au ball was found outside. ....	166
Figure 118. The SEM image shows gold ball scattered outside the pattern. The scale bar is 50 $\mu\text{m}$ .....	166
Figure 119. This gap is not big enough to have a big Au ball produced in the gap. The scale bar is 2 $\mu\text{m}$ . ....	167
Figure 120. The Au balls are inside the pattern. The scale bar is 10 $\mu\text{m}$ .....	167
Figure 121. The image is near the edge of the pattern. The scale bar is 20 $\mu\text{m}$ . ....	167
Figure 122. The temperature was raised to 700° C and Au was deposited by pulsed laser deposition (PLD) for 1 minute. The substrate was then maintained at 700° C for 5 minutes before reducing power to the tube furnace. The shape of the Au ball looks like a bridge. The scale bar is 2 $\mu\text{m}$ .....	168
Figure 123. The image is taken near the edge of the pattern. The scale bar is 5 $\mu\text{m}$ .....	168
Figure 124. The image is taken near the edge of the pattern. The scale bar is 2 $\mu\text{m}$ .....	168
Figure 125. The temperature was raised to 700° C and Au was deposited by pulsed laser deposition (PLD) for 1 minute and reducing power immediately. The scale bar is 20 $\mu\text{m}$ . ....	169

Figure 126. The temperature was raised to 700° C and Au was deposited by pulsed laser deposition (PLD) for 1 minute and reducing power immediately. ....	169
Figure 127. The mask designed for patterning the SiO <sub>2</sub> layer using a positive photoresist (Shipley 1813). ....	170

## Chapter 6

Figure 128. Schematic diagrams of (a) metal catalyst and (b) lateral nanowire growth. ....	174
Figure 129. The nanowires grew across the trench. The scale bar is 50 $\mu\text{m}$ . ....	175
Figure 130. Nanowires grew across the 70 $\mu\text{m}$ wide trench. The scale bar is 50 $\mu\text{m}$ ..	176
Figure 131. Dense nanowires grew across the trench. The scale bar is 50 $\mu\text{m}$ . ....	177
Figure 132. The whiskers with large diameters grew on the side wall. The scale bar is 50 $\mu\text{m}$ . ....	178
Figure 133. The scale bar is 50 $\mu\text{m}$ . ....	178
Figure 134. The scale bar is 50 $\mu\text{m}$ . ....	178
Figure 135. The nanowires grew in the region with different widths. ....	179
Figure 136. Nanowires inside the trench. The scale bar is 50 $\mu\text{m}$ . ....	180
Figure 137. Nanowires inside the trench. The scale bar is 50 $\mu\text{m}$ . ....	180
Figure 138. Nanowires grew along the corner. ....	180
Figure 139. The growth of nanowires in the trench. ....	182
Figure 140. The SEM image shows nanowires grew across the trench. ....	183
Figure 141. The nanowires grew across the 80 wide trench. ....	184
Figure 142. The scale bar is 20 $\mu\text{m}$ . ....	184
Figure 143. The scale bar is 20 $\mu\text{m}$ . ....	184
Figure 144. The growth of nanowires in the trench. ....	185
Figure 145. The scale bar is 20 $\mu\text{m}$ . ....	185

Figure 146. In the SEM image of whiskers grew across the trench. The scale bar is 20 $\mu\text{m}$ . .....	186
Figure 147. The scale bar is 10 $\mu\text{m}$ . .....	187
Figure 148. The scale bar is 10 $\mu\text{m}$ . .....	187
Figure 149. The scale bar is 20 $\mu\text{m}$ . .....	187
Figure 150. The scale bar is 20 $\mu\text{m}$ . .....	187
Figure 151. The scale bar is 20 $\mu\text{m}$ . .....	187
Figure 152. The scale bar is 20 $\mu\text{m}$ . .....	188
 <b>Chapter 8</b>	
Figure 153. Schematic of an SEM .....	194
Figure 154. Interaction-volume variation with accelerating voltage. ....	200
Figure 155. Secondary electron escape, edge effects, and image production. ....	201
Figure 156. Schematic of an EDS detector attached to an SEM. ....	205
Figure 157. Quartz tube furnace system .....	208
Figure 158. Autosketch of optical-side drawing.....	209
Figure 159. Autosketch of endcap .....	210
Figure 160. Autosketch of endcap .....	211
Figure 161. Autosketch of endcaps assembled .....	212

## **Introduction**

Following Richard Feynman's best known comment "There is plenty of room at the bottom [1]," emerged a series of dominant interest in exploring subjects concerning reduced dimensional structures, such as microelectromechanical system (MEMS), quantum wells, nanowires, nanotubes, and nanodots [2-4]. Among these topics, semiconductor nanowires are deemed to be an innovation by means of the application of the Moore's law and the capabilities of manufacturing ever smaller metal oxide semiconductor field effect transistors (MOSFETs). With the ongoing evolution of reducing the length of the channel, it appears that corresponding technological advances should have been developed to support usable threshold voltages. In other words, the desired advances should be able to sustain the increased coverage of the channel surface by the gate through structures such as the Double Gate FET, or FinFET [5]. In particular, the fabrication of nanowires by self assembly deserves more attention with the improvement of semiconductor nanowires fabrication techniques [6, 4]. In general, applications of the nanowires structures of interest encompass field effect devices, mechanically resonant structures, and sensors.

## **Nanotechnology**

Nanotechnology deals with various structures of matter having dimensions of the order of a billionth of a meter. A recent definition of nanotechnology is "Nanotechnology is the understanding and control of matter at dimensions of roughly 1 to 100 nanometers [7]." This dimension range is especially drawing attention where



interdisciplinary fields of research are emerging [8,9,10]. The nanoscale is unique because it is the size scale where the commonplace properties of materials, including conductivity, hardness, or melting point, and the more exotic properties of the atomic and molecular world, such as wave-particle duality and quantum effects converge [11]. On the nanoscale, the most fundamental properties of materials and machines are closely related to their size, the condition that is not observed if on other scales. If the size reduces to or smaller than de broglie wavelength, the property changes. For example, after calculation we can get the de broglie wavelength of germanium is 17.98 nm. That means once the size of germanium smaller than 17.98 nm, the material properties will different from other scale.

### **One-dimensional nanostructure**

The reason why semiconductor nanowires and nanotubes, one-dimensional structures with diameters not exceeding a few hundred nanometers, can exhibit a breakthrough in terms of electronic and optical properties is related to their unique structural one-dimensionality and the effects of quantum confinement of carriers in two dimensions [12]. Sitting on the advantage of the selection of various compositions and band structures, the one-dimensional semiconductor nanostructures are deemed to be the essential components for constructing likely diverse applications of nanoscale devices. Considering this feature of one-dimensional nanostructures, current research has mainly paid attention to a logical synthetic control of one-dimensional nanoscale building blocks, the new characterization of properties, and the fabrication of devices would be taken into account by the use of nanowire building blocks, and by integrating nanowire elements

into architectures that are complicated in functions [13]. Corresponding with the topic of this dissertation, nanowires become the focus in the following discussion.

## Application

Having specific and distinguished characteristics, such as the small sizes and high surface-to-volume ratios, one-dimensional nanostructures have commanded great attention by their useful and newsworthy properties. The control of the surfaces and internal interfaces also equip one-dimensional nanostructures with unique stability effects. Certain fundamental limitations pose problems for the realization of this effort. Size-dependent thermal conductivity in nanostructures is one of them. Under the influence of increased boundary scattering and lessened phonon group velocities resulting from the phonon confinement, the phonon transport is expected to be blocked in thin 1D nanostructures. Nonetheless, if employing an alternative perspective, poor heat transport is useful for thermoelectric materials, which are characterized by a figure of merit :  $ZT = \alpha^2 T / [\rho(\kappa_p + \kappa_e)]$ , where  $\alpha$ ,  $T$ ,  $\rho$ ,  $\kappa_p$  and  $\kappa_e$  represent the Seebeck coefficient, absolute temperature, electronic resistivity, lattice thermal conductivity and electronic thermal conductivity, respectively. It is found that as the proceeding of the phonon transport worsens, the value of the figure would improve. In fact, the Dresselhaus research group has predicted that  $ZT$  can be increased above bulk values in thin nanowires as long as the diameters, compositions and carrier concentrations are carefully manipulated [14, 15]. This contention has been confirmed by different levels of experiments.

Various types of nanowires have been fabricated using different methods, including evaporation [16], laser ablation [17], chemical vapor deposition (CVD), and electron

beam lithography [18]. Moreover, nanowires that have been the target of studies range from silicon, germanium, III-V material, to II-VI material.

In the last decade, silicon nanowires have attracted plenty of research interests owing to the fact that silicon has certain attributes useful in applications of nanodevices. A couple of methods have been proved to be viable growth mechanisms. Metal catalyst-assisted and the oxide assisted (OA) methods are evaluated as the most accepted ones among the many methods discussed. Metal catalyst-assisted growth mechanism functions in connection with the widely known vapor-liquid-solid (VLS) mechanism [6]. Technically, the silicon vapor source in metal catalyst-assisted mechanism is obtained through silane which is created by using CVD method or by laser ablating the metal catalyst in physical vapor deposition (PVD). Without using the metal catalyst, the oxide-assisted method is making use of the metal oxide powder to grow nanowires.

Currently, there is more and more research focused on the silicon material as well as on III-V and II-VI material. III-V and II-VI semiconductor nanowires are grown by means of the laser-assisted catalytic growth (LCG) method [19]. In addition, the nanowire products are collected at the down-stream cold end of the furnace.

One challenge that needs to be addressed is how to grow nanowires in a way that is appropriate to the device fabrication from a manufacturing perspective. The exceptionally high surface-to-volume ratio of thin one-dimensional nanostructures has enabled them to function well with inherently high sensitivity and short response time. A common sensing device can be produced by configuring high performance, field-effect nanowire transistors, in which the specific function of sensing is achieved by coupling a recognition group and the surface of the nanowire. The device incorporates a Si

nanowire with distinct p- or n-type doping, source drain electrodes that are insulated from the environment, and a microfluid device for delivery of solutions. Since the Si nanowire is suspended in ethanol and flow aligned on substrates, and the contact leads are characteristic of emerging with electron –beam lithography, for manufacturing purposes, it would be beneficial to grow the device directly from substrates.

In this study, we investigated the growth of different nanowires and the control of the growth of nanowires. The procedures encompass exploring various materials, including GaAs, InSb,  $\text{Sr}_8\text{Ga}_{16}\text{Ge}_{30}$  and Ge, and different methods and approaches in order to achieve the above research goal. In particular, the deposition scheme was accomplished by the use of the pulsed laser deposition (PLD) technique, and KrF excimer laser and the nanowire growth were utilized based on the vapor-liquid-solid (VLS) mechanism using gold as the mediating metal catalyst. The role of oxygen in the metal-catalyzed nanowire growth process is also studied in order to gain a deeper understanding of the two nanowire growth methods.

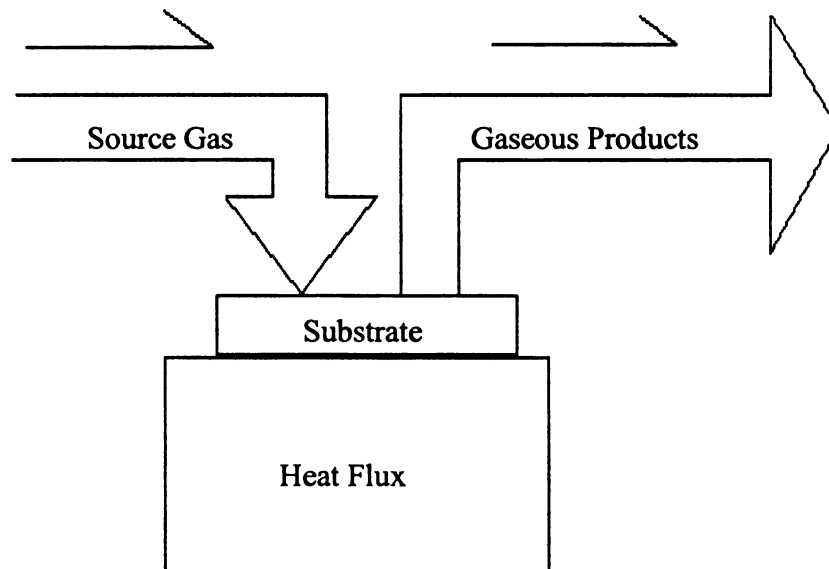
# **CHAPTER 1 THEORY**

## **1.1 Different grow methods**

The vapor-liquid-solid growth mechanism was reported by Wagner and Ellis in 1964 [20]. In their report, a chemical vapor deposition technique was used to fabricate high aspect ratio silicon wires of with diameters of 200  $\mu\text{m}$ . Many reports have followed this initial work [21,22,23], with more recent efforts focused on diameter in the submicron and nanoscale with reported diameters down to 3 nm [24,25]. Both chemical vapor deposition (CVD), and physical vapor deposition (PVD) techniques have been utilized in the fabrication of nanowires through the vapor-liquid-solid technique. More recently, an oxide assisted (OA) technique has been proposed as another mechanism for the growth of nanowires [26]. In this section, I review the various deposition techniques, and identify the similarities and difference between them.

### **1.1.1 Chemical Vapor Deposition (CVD)**

Chemical vapor deposition (CVD) is a process which is widely utilized for depositing thin films of various materials. In addition, there are a wide range of applications of CVD, such as the fabrication of microelectronic devices and the deposition of protective coatings.



**Figure 1.** Chemical vapor deposition process

Usually, in a CVD process, the substrate is exposed to one or more volatile precursors, whose reaction and decomposition on the substrate surface lead to the formation of the desired deposit.

As the deposited surface takes shape, the gas mixture is heated as it approaches the surface which is placed upon a heated substrate. Reactant gases, which are often diluted in a carrier gas, come into the reaction chamber at room temperature. Depending on the process and operating conditions, the reactant gases may go through consistent chemical reactions in the vapor phase before hitting the surface.

Method	Energy Range(eV)	Multi- Element Rate Control	Vacuum Requirement	Typical Deposition Rate (Å/s)	>10 mTorr Reactive Gas
CVD	0.1	Moderate	HV	20	Yes
MOCVD	0.1	Moderate	UHV	10	Yes
MBE	0.1	Moderate	UHV	3	No
PECVD	0.1-500	Moderate	HV	20	Yes
PLD	1-1000	Easy	HV	10	Yes
TE	0.1	Difficult	HV	20	No

**Table 1.** Qualitative comparison of deposition rates of various growth techniques [31]

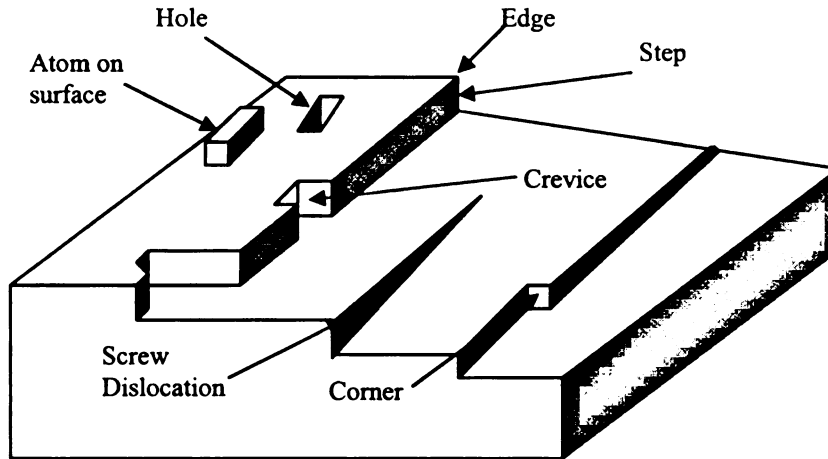
Close to the surface thermal, the momentum, and the layers of the chemical concentration boundary change with the status of the gas stream. They form as the gas streams heats, and then slow down due to the viscous drag, and the chemical composition alters accordingly. On the other hand, heterogeneous reactions of the source gases or reactive intermediate species take place at the deposition surface which produces the deposited material. By this way, byproducts resulting from the gaseous reaction are carried out of the reaction chamber.

**Plasma-enhanced CVD (PECVD)** is the CVD process that makes use of plasma to improve chemical reaction rates of the precursors. What's important is that PECVD process enables the deposition to occur at lower temperatures, which plays an important role in the semiconductors producing.

### **1.1.2 Physical Vapor Deposition (PVD)**

Physical vapor deposition involves atoms and/or molecules of a material that are deposited from the gas phase (or vapor) onto a substrate without a chemical reaction step taking place. Various mechanisms can be used to get the material into the gas phase including, thermal evaporation, sputtering, pulsed laser deposition, cathodic arc, and molecular beam epitaxy. During the PVD process, material from a liquid or solid source is transported through the gas phase to a substrate. In placing the atoms or molecules from the source into the vapor phase, the particles are raised in energy. As the particles arrive, their energy is taken away by a cooler substrate surface facing the source, which allows the particles to form a solid thin layer. The atoms or molecules in the vapor phase will condense on the substrate after some surface diffusion of the adatoms. Accommodation of the adatoms occurs as the Gibbs free energy,  $\Delta G$ , is sufficiently reduced during condensation. Since  $\Delta G$  is further reduced for adatoms that form clusters, or accommodate to step edges, there is a preferential growth of films along such defects, and/or in island formations. These mechanisms for film growth are summarized in blow.





**Figure 2.** Schematic of film surface with various edges, pits, and clusters identified.

Assuming the incident kinetic energy is not too high; an atom striking a surface will lose its velocity component normal to the surface in a short time. The incident vapor atom is then physically adsorbed and called an adatom. It may or may not be completely thermally equilibrated with the surface. If not equilibrated, it can move over the surface by jumping from one potential well to another as driven by thermal activation from the surface and/or by its own kinetic energy parallel to the surface. The adatom has a finite stay or residence time on the surface during which it may interact with other adatoms to form a stable cluster and be chemically adsorbed (incorporated into the surface) with the release of the heat of condensation. If not adsorbed, the adatom reevaporates (desorbs) into the vapor phase. Therefore, condensation is the net result of an equilibrium between the adsorption and desorption processes.

### Sticking Coefficient

Sticking coefficient is the probability that an impinging atom will be incorporated into the substrate (surface) is called the “condensation” or “sticking” coefficient. This probability is given as the ratio of the number of atoms incorporated into the film to the number of atoms impinging on the surface.

$$\alpha_s = \frac{N_{adh}}{N_{tot}} \quad \text{Equation 1}$$

where  $N_{adh}$  = number of atoms adhering to the surface and  $N_{tot}$  = total number of atoms arriving at the substrate.

### Accommodation Coefficient

The accommodation coefficient,  $a_T$ , is a measure of the degree of thermal equilibration with the surface and is given by:

$$a_T = \frac{T_i - T_r}{T_i - T_s} = \frac{E_i - E_r}{E_i - E_s} \quad \text{Equation 2}$$

where temperatures, T's, and kinetic energies, E's, correspond to the equivalent rms values for the incident (*i*), reevaporated (*r*) atoms, and the substrate (*s*) respectively.

Several theoretical investigations considered the problem of a head-on collision of an atom with a one-dimensional lattice consisting of spring-connected masses. For nearly equal masses of the impinging atom and the substrate lattice atom, a unity sticking coefficient should be obtained for incident kinetic energies up to 25 times the desorption energy,  $E_{des}$ . Since, for metals,  $E_{des} \approx 1\text{-}4$  eV, vapor atoms of equivalent beam temperatures of the order of a million degrees should be physically adsorbed. Of course, a 3D lattice of spring connected masses would be stiffer, decreasing the expected sticking

coefficient. For light impinging atoms relative to the substrate atoms, and/or for high incident kinetic energy, the sticking coefficient can be much less than unity.

As mentioned, the adatom has a finite stay or residence time,  $\tau_s$ , on the surface given by

$$\tau_s = \frac{1}{\nu} e^{\frac{E_{des}}{k_B T}} \quad \text{Equation 3}$$

where  $E_{des}$  = energy of desorption,  $\nu$  = surface vibrational frequency ( $\sim 10^{12}$  Hz),  $k_B$  is Boltzmann's constant ( $8.618 \times 10^{-5}$  eV/K). It has been theoretically predicted that almost all of the initial energy  $E_i$  is lost in the first three lattice vibrations and that the time to thermally equilibrate with the substrate,  $\tau_e$ , is about  $\tau_e \leq \frac{2}{\nu}$  or about a picosecond.

At high binding energies,  $\tau_s$  is large ( $\tau_e$  is small -  $\nu$  large) and thermal equilibrium occurs rapidly. Here an adatom can be considered as localized and it will diffuse by discrete jumps.

If  $E_{des} \sim k_B T$ , they do not equilibrate rapidly but remain "hot" (usually having  $\alpha_s < 1$ ), and the adatoms can be viewed as a 2D gas (where the kinetic theory of gasses can be applied).

During  $\tau_s$ , the adatoms will diffuse an average distance,  $\bar{X}$ , of

$$\bar{X} = \sqrt{2D_s \tau_s} = a_0 \sqrt{2\nu \tau_s} e^{-\frac{E_s}{2k_B T}} = \sqrt{2} a_0 e^{\frac{E_{des} - E_s}{2k_B T}} \quad \text{Equation 4}$$

where  $a_0$  is the jump distance between adsorption sites on the surface (on the order of atomic dimensions),  $E_s$  is the activation energy for a surface diffusion jump, and  $D_s$  is the surface diffusion coefficient:

$$D_s = a_0^2 v e^{-\frac{E_s}{k_B T}}$$

Equation 5

Several values of desorption and activation energies are given in the following table.

These values are very sensitive to the cleanliness of the films as shown for Cd on clean and contaminated Ag substrates.

**Table 2.** Experimental values for the binding energy,  $E_{des}$ , and the activation energy for diffusion,  $E_s$ , for some typical systems.

Condensate	Substrate	$E_{des}$ , eV	$E_s$ , eV
Ag	NaCl		0.2
Ag	NaCl		0.15 (evaporation) 0.10 (sputtering)
Al	NaCl	0.6	
	Mica	0.9	
Ba	W	3.8	0.65
Cd	Ag (fresh film)	1.6	
	Ag, glass	0.24	
Cu	Glass	0.14	
Cs	W	2.8	0.61
Hg	Ag	0.11	
Pt	NaCl		0.18
W	W	3.8	0.65

Experimentally the value of  $E_{des}$  has typically shown a value of about 4 times the diffusion activation energy  $E_s$ .

### Homogenous Nucleation

For the homogenous nucleation of a spherical solid phase of material, the change in free energy can be described as

$$\Delta G = \frac{4}{3}\pi r^3 \Delta G_v + 4\pi r^2 \gamma \quad \text{Equation 6}$$

where  $r$  is the radius of the sphere,  $\gamma$  is the surface free energy per unit area, and  $\Delta G_v$  is the change in free energy per unit volume as given by

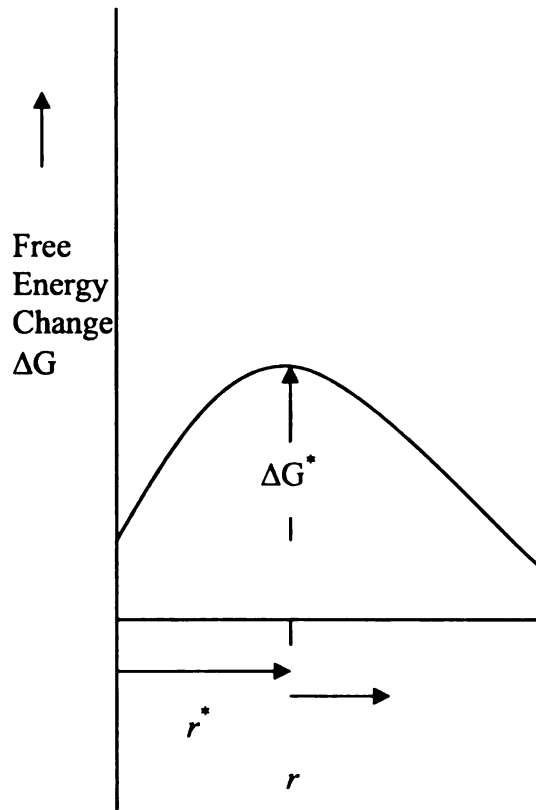
$$\Delta G_v = -\frac{k_B T}{\Omega} \ln \frac{P_v}{P_s} \quad \text{Equation 7}$$

Here  $\Omega$  equals the atomic volume of the solid,  $P_v$  is the pressure of the supersaturated vapor, and  $P_s$  is the vapor pressure at the surface of the solid. With the supersaturation,  $S$ , defined as  $(P_v - P_s)/P_s$  we could write

$$\Delta G_v = -\frac{k_B T}{\Omega} \ln(1 + S) \quad \text{Equation 8}$$

Nucleation will not occur unless there is supersaturation ( $S > 0$ ) and  $\Delta G_v$  is negative.

An energy barrier to the formation of stable nuclei is evident when the derivative of (Equation 6) with respect to  $r$  is set equal to zero as shown in Figure 3.



**Figure 3.** Free-energy change ( $\Delta G$ ) as a function of cluster ( $r^* > r$ ) or stable nucleus ( $r > r^*$ ) size.  $r^*$  is critical nucleus size, and  $\Delta G^*$  is critical free-energy barrier for nucleation.

The critical radius is found to be

$$r^* = -\frac{2\gamma}{\Delta G_v} \quad \text{Equation 9}$$

or using this in (Equation 6) gives the critical free energy barrier for homogenous nucleation

$$\Delta G^* = \frac{16\pi\gamma^3}{3(\Delta G_v)^2} \quad \text{Equation 10}$$

The nucleation rate for this sphere is

$$\dot{N} = N^* A^* \omega \quad \text{Equation 11}$$

where

$$N^* = n_s e^{-\frac{\Delta G^*}{k_B T}} \quad \text{Equation 12}$$

with  $n_s$  = density of all possible nucleation sites, and  $N^*$  = equilibrium concentration of stable nuclei,  $\omega$  is the rate at which atoms impinge on the the nuclei of critical area,

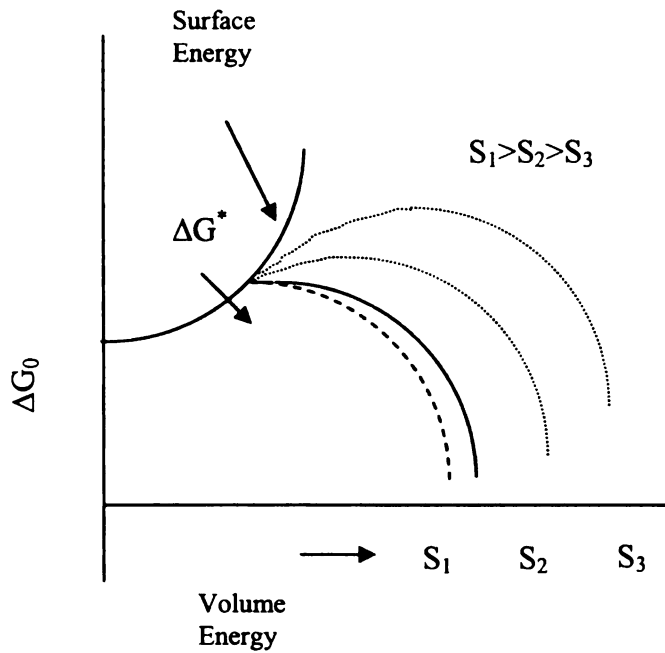
$$A^* = 4\pi r^{*2}.$$

$$\omega = \frac{\alpha_s (P_v - P_s) N_A}{\sqrt{2\pi MRT}} \quad \text{Equation 13}$$

or upon substitution

$$\dot{N} = n_s e^{-\frac{\Delta G^*}{k_B T}} 4\pi r^{*2} \frac{\alpha_s (P_v - P_s) N_A}{\sqrt{2\pi MRT}} \quad \text{Equation 14}$$

This shows  $\dot{N}$  is strongly dependent on  $\Delta G^*$  which is strongly dependent on the supersaturation,  $S$  as was shown in (Equation 8). The effect of supersaturation on  $\Delta G^*$  is shown in Figure 4.





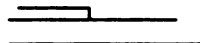
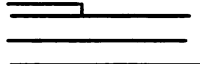

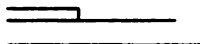
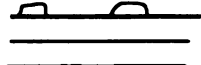


**Figure 4.** Total free energy (surface plus volume free energies) of cluster formation vs. size ( $r$ ) for different supersaturations ( $S$ ).

### Capillarity Theory

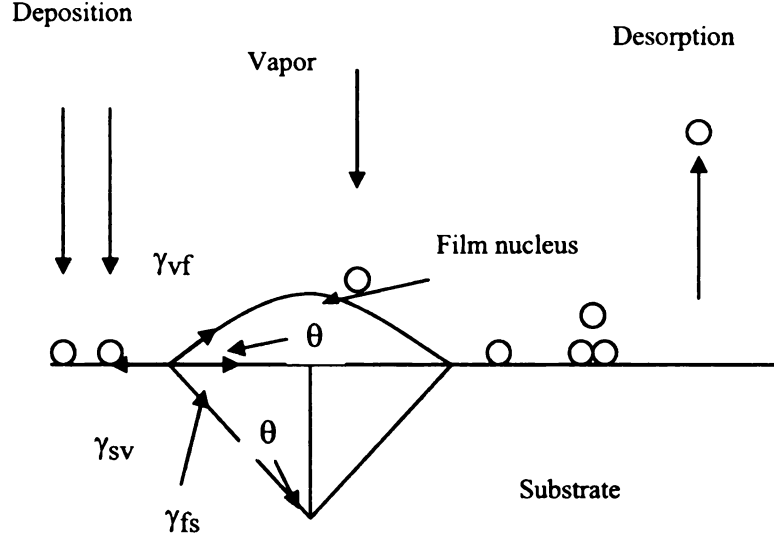
The capillarity theory extends the homogenous theory to the nucleation of a film on a planar substrate. The three different growth modes of a film on a substrate are Volmer-Weber (or island), Frank-van der Merwe (or layer), and Stranski-Krastanov (or layer plus island) are summarized in Figure 5.



Coverage		$\theta < 1\text{ML}$	$1 < \theta < 2$	$\theta > 2\text{ML}$
Mechanism				
3-D Island Growth				
2-D Layer-by-layer Growth				
Stranski-Krastanov Growth				

**Figure 5.** Schematic representation of three film growth modes.  $\theta$  is the overlayer coverage in monolayers (ML).

Here three interface tensions must be considered as shown in Figure 6, to replace the interface energy,  $\gamma$ , in (Equation 2).



**Figure 6.** Schematic of basic atomistic processes on substrate surface during vapor deposition.

The substrate-to-vapor,  $\gamma_{sv}$ , film-to-vapor,  $\gamma_{vf}$ , and film-to-substrate,  $\gamma_{fs}$  are related by

$$\gamma_{sv} = \gamma_{fs} + \gamma_{vf} \cos \theta \quad \text{Equation 15}$$

And (Equation 2) becomes

$$\Delta G = a_3 r^3 \Delta G_v + a_1 r^2 \gamma_{vf} + a_2 r^2 \gamma_{fs} - a_2 r^2 \gamma_{sv} \quad \text{Equation 16}$$

The critical cluster size,  $r^*$ , is found from  $\frac{d\Delta G}{dr} = 0$  which gives

$$r^* = -\frac{2[a_1 \gamma_{vf} + a_2 (\gamma_{fs} - \gamma_{sv})]}{3a_3 \Delta G_v^2} \quad \text{Equation 17}$$

and

$$\Delta G^* = \frac{4[a_1 \gamma_{vf} + a_2 (\gamma_{fs} - \gamma_{sv})]^3}{27a_3^2 \Delta G_v^2} \quad \text{Equation 18}$$

In general, PVD is used to deposit films with thickness ranging from a few nanometers to a few micrometers. In addition, PVD can be used to create multilayer structures by supplying different source materials during the process. The substrate size and material can be varied.

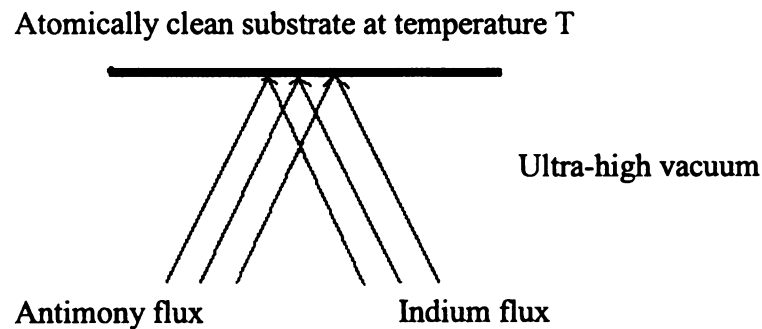
PVD processes can be used to deposit films of elements and alloys as well as compounds using reactive deposition processes. In reactive deposition processes, compounds are formed by the reaction of depositing material with the ambient gas environment. Quasi-reactive deposition is the deposition of films of a compound material from a compound source. During the transport and condensation process, having a partial pressure of reactive gas in the deposition environment can compensate the loss of more volatile species or less reactive species. A couple of examples representative of the physical deposition are given below:

### **Molecular beam epitaxy**

Molecular beam epitaxy (MBE) is a beam of molecules or atoms which emanate from an evaporation or effusion source. The beam of particles travels across an evacuated chamber with few if any collisions, and deposits onto a substrate. Throughout the process, atoms are deposited one layer at a time, under ultra-high vacuum (UHV  $10^{-10} - 10^{-11}$  Torr ), which leads to the formation of a perfect crystal. At this pressure, the mean-free path of gases is several orders of magnitude larger than the distance between the source and substrate. At very low pressures, the mean-free path can be approximated by [27]:

$$L = \frac{5 \times 10^{-3}}{P} \quad \text{Equation 19}$$

In solid-source MBE, pure elements such as indium and antimony are heated in separate effusion cells furnaces until they each slowly begin to evaporate. The evaporated elements then condense on a heated substrate, where they react with each other and create indium antimony.



**Figure 7.** Schematic representation of MBE deposition of a thin film. The film thickness and composition is defined by controlling the individual fluxes.

A computer controls shutters in front of each effusion cell, allowing precise control of the thickness of each layer, down to a single layer of atoms. Intricate structures of layers of different materials may be fabricated this way. Such control has allowed the development of structures where the electrons can be spacially confined, giving quantum wells or even quantum dots. Such layers are now a critical part of many modern semiconductor devices, including semiconductor lasers and light emitting diodes.

The ultra-high vacuum environment within the growth chamber is maintained by a system of cryopumps, and cryopanel, chilled using liquid nitrogen to a temperature of 77 kelvins (-196 degrees Celsius). The wafers on which the crystals are grown are mounted

on a rotating platter which can be heated to several hundred degrees Celsius during operation.

The main advantages of MBE are the low growth rate, which is not conditioned by wafer temperatures and facilitates a precise control of film thickness, and high purity where only elements that are components in the deposited film are in the vapor phase during deposition. In this way, chemical reaction byproducts can not be incorporated as impurities as can be the case with CVD methods.

**Thermal evaporation** is one of the oldest techniques of depositing thin films. Evaporation uses a heater to melt the material and raises its vapor pressure to a useful range. The vapor pressure is a pressure at which the vapor of the targeted substance is in equilibrium with its liquid or solid forms. Employing the thermodynamic principle, the number of molecules departing a unit area of evaporant per second, or flux  $F$ , is given by:

$$F = N_{\phi} \exp\left(-\frac{\phi_e}{kT}\right) \quad \text{Equation 20}$$

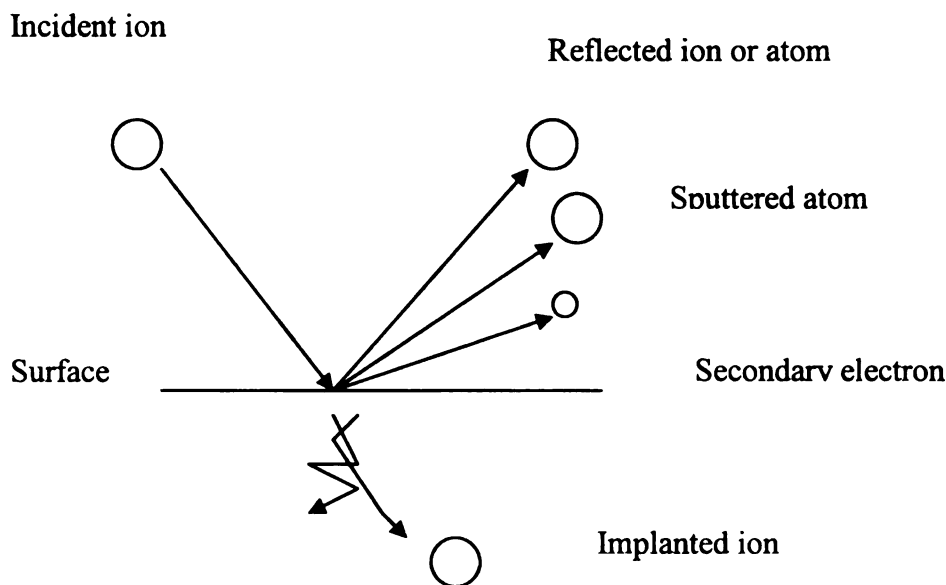
where  $N_{\phi}$  is a slowly variable function of the temperature ( $T$ ) and  $\phi_e$  is the activation energy (in eV) needed to evaporate one molecule of the material. The activation energy for evaporation is associated with the enthalpy of the formation of the evaporant,  $H$ , as

$$H = \phi_e \times e \times N. \quad \text{Equation 21}$$

This is executed in a high vacuum system, which could allow the vapor to approach the substrate without reacting with or spreading out against other gas-phase atoms in the chamber, and could reduce the consolidation of unwanted substances from the residual gas in the vacuum chamber [28]. To avoid contamination, only those materials with a

much higher vapor pressure than the heating element can be deposited. Thermal evaporation of compounds and alloys is not commonly done, since the individual elements typically have different evaporation rates.

**Sputtering** relies on ions to strike materials from a target, in which a small number of atoms are obtained at a time. The physical sputtering process entails the physical vaporization of atoms from a surface via momentum transfer realized by bombarding energetic atomic sized particles.



**Figure 8.** A schematic representation of the sputtering process.

Commonly, the energetic particles are ions of a gaseous material being accelerated in an electric field [29]. For example, during the process of sputtering, the target, such as a disc of the material to be deposited, at a high negative potential, is bombarded repeatedly

with positive argon ions. The target material is sputtered away principally in the form of neutral atoms through momentum transfer and then ejected surface atoms are deposited onto the substrate placed on the anode. The feature of allowing a great deal of materials available to use makes sputtering a preferred option over evaporation in many applications [28]. As shown in Equation 4, the amount of materials,  $W$ , sputtered from the cathode is inversely related to the gas pressure  $P$ , and the anode-cathode distance,  $d$ :

$$W = \frac{kVi}{Pd} \quad \text{Equation 22}$$

where  $V$  is the working voltage,  $i$  is the discharge current and  $k$  is a proportionality constant. The target can be maintained at a low temperature by water cooling, and compounds and alloys can be deposited with good transfer of stoichiometry from the target to the substrate.

**Pulsed laser deposition (PLD)** has emerged as one of the simplest and most versatile methods for the deposition of thin films of a wide variety of materials. The stoichiometric removal of constituent species from the target during the ablation process is one of the main advantages in PLD compared with other deposition techniques. Different thin film materials have been deposited by the use of PLD, including metals, semiconductors, nitrides, dielectrics, oxide, organic compounds/polymers, and ternary compounds. It has been described as an optical sputtering technique, and with the power source external to the deposition chamber, multiple chambers can use the same laser [30].

## **1.2 Pulsed Laser Deposition (PLD)**

### **1.2.1 History and Fundamental of pulsed laser deposition**

#### **Introduction**

Pulsed laser deposition (PLD) is a technique commonly used to deposit thin films [31]. This technique involves the evaporation of a solid target by short, high-energy laser pulses. The laser beam vaporizes the surface of the target, and the vapor condenses on a substrate placed near the target.

The PLD technique has the following advantageous characteristics: 1. Simple: a laser beam vaporizes a target surface, producing a film with the same composition as the target. 2. Versatile: many materials can be deposited in a wide variety of gases over a vast range of gas pressures. 3. Cost-effective: one laser can serve many vacuum systems. 4. Fast: high quality samples can be grown in 10 or 15 minutes. 5. Scalable: complex oxides move toward the volume production [31].

#### **Historical Development of Pulsed Laser Deposition**

**1916** – Albert Einstein proposed a hypothesis regarding the process of the stimulated emission.

**1960** – Theodore H. Maiman built the first optical maser by means of a rod of ruby as the lasing medium.

**1962** – Breech and Cross utilized the ruby laser to vaporize and excite atoms from a solid surface.

**1963** – Askar'yan made contributions to the development of the laser beam to liquid surface interactions.



**1963** – Meyerand and Haught investigated the laser beam to gaseous material interactions.

**1965** – Smith and Turner conducted studies on semiconductors, dielectrics, chalcogenides, and organometallic materials.

**1970s** –Q -switches were used to produce short optical pulses under the condition of peak power.

$$> 10^8 \text{ W/cm}^2 . \quad E = \sqrt{\frac{2\Phi}{c\epsilon_0 n}}$$

$E$  = electric field of electromagnetic wave (V/cm)

$\Phi$  = power density in ( $\text{W/cm}^2$ )

$\epsilon_0$  = dielectric constant in vacuum ( $8.85 \times 10^{-12} \text{ F/m}$ )

$n$  = refractive index

$c$  = velocity of light ( $3.00 \times 10^8 \text{ m/s}$ )

**1975** – A complex stoichiometry took form with the low temp. superconductor  $\text{Re B}_{22}$  (Desserre and Eloy)

**1979** – (Gapanov et al., 1979) semiconductor superlattices. Also demonstrated reactive deposition in 1979.

**1980s** – PLD as a technique for film growth earned recognition and drew a great deal of interest. Primarily, PLD was used to formulate crystalline thin films with epitaxy quality. In addition, PLD was present in the growth of the ceramic oxide, nitride films, metallic multilayers, and various superlattices.

**1990s** – The swift development of the laser technology rendered PLD more desirable. Newly developed lasers were characteristic of higher repetition rate than the

early ruby lasers, which made the growth of thin films possible. Then, reliable electronic Q-switches laser was adopted to generate optical pulses of extremely short length. It is this factor that created the opportunities for PLD to be used to attain the congruent evaporation of the target and to deposit stoichiometric thin films. In general, this significant breakthrough resulted in the development of the laser with a high efficient harmonic generator and excimer lasers delivering UV radiation. The non-thermal laser ablation of the target material was influenced and became exceedingly efficient thereafter. Additionally, using PLD to synthesis buckminsterfullerene and nanotubes was another example of its application.

**2000s** – Some production-related issues began to gain interests, such as reproducibility, the large-area scale-up, and the multiple-level. In other words, the attention awarded to the thin film fabrication reached its peak time.

### **1.2.2 Pulsed Laser Deposition: Mechanisms of Ablation**

#### **Introduction**

Although the Pulsed Laser Deposition (PLD) method is conceptually simple, the underlying ablation mechanisms are related to complex physical principles, such as collisional, thermal evaporation, electronic sputtering, exfoliation and hydrodynamics sputtering. In a typical PLD process, a target is placed in a vacuum chamber, and a pulsed laser beam converts the target material from solid into a vapor, often with a plasma or plume formed above the target, the evaporated species have high translational energy, and expand away from the target toward the substrate where condensation occurs. The

main components of the above physical process include a laser, optics, and a vacuum system. In general, the thin film growth process using PLD can be divided into the following four phases:

1. The connection of a high flux of laser radiation with the target and surface and the laser-plume interaction.
2. Dynamic ranges of ablation materials.
3. Deposition of the ablation materials with the substrate.
4. Nucleation and growth of a thin film on the substrate surface.

Each phase in PLD is important in fabricating crystalline thin films with epitaxial quality and those having stoichiometric, uniform and small surface roughness composition. In the first stage, the pulsed laser beam is focused onto the surface of the target. The high flux densities and short pulse duration are conducive to the rapid heating of all elements in the target to their evaporation temperature. Materials are then removed from the target surface and are ablated out with stoichiometry as in the target. The fluences of the laser shining on the target determine the immediate ablation rate.

After the laser-plume interaction, during the second stage of the thin film growth, the emitted materials are inclined to move towards the substrate under the influence of the gas-dynamic expansion of plasma created by irradiating a solid with laser pulses, and to demonstrate the forward peaking phenomenon. The spatial thickness is a parameter that is varied as a function of  $\cos^n \theta$ , and the spot size of the laser and the plasma temperature exert major effects on the uniformity of the deposited film. In addition, the

distance between the target and the substrate is a deciding factor that affects the angular spread of the ablated materials.

The third stage of deposition of the ablation materials with the substrate is critical in determining the quality of the produced thin film. The reason is that the ejected high-energy species have effect on the substrate surface and might incur a variety of damage to the substrate. To be more specific, these energetic species can sputter some of the surface atoms and a collision region will be shaped between the incident flow and the sputtered atoms. Then, the film could be produced after a thermalized region is formed. In fact, the collision region is utilized as a source for the condensation of particles. If the condensation rate is higher than the rate of particles resulted from the sputtering, the thermal equilibrium condition can be achieved fast and the film will grow on the substrate surface under the condition of the obstruction of the direct flow of the ablation particles and the thermal equilibrium reached.

In the final stage of the nucleation-and-growth of crystalline films depends the condensing material, temperature and the properties of substrate. The nucleation process depends on the interfacial energies between the three phases present, the vapor atom, condensing layer, and the substrate. It is described that the minimum-energy shape of a nucleus is like a cap. The deposition rate and the substrate temperature are such factors that might affect the critical size of the nucleus. In the case of the large nuclei, which are a characteristic of small supersaturation, they create insulated patches of the film on the substrate which are produced thereafter and coalesce together. While the supersaturation increases, the critical nucleus is reduced until its height extends to the atomic diameter and its shape is equal to that of a two-dimensional layer. If the scale of the

supersaturation is large, the layer-by-layer nucleation will occur for partially wetted foreign substrates.

In order to grow the crystalline film, the surface mobility of the adatom, or the vapor atoms, is required. Usually, the adatom will diffuse through different atomic distances before holding to a stable position within the newly formed film. The adatom's surface diffusion ability is determined by the surface temperature of the substrate. In general, the high temperature is conducive to the rapid and defect-free crystal growth, while at low temperature or large supersaturation, the energetic particle effect might deter the crystal growth and result in disordered or even amorphous structures.

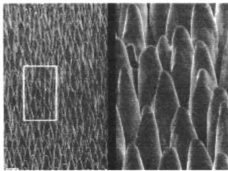
In the PLD process, during which the short laser pulsed duration ( $\sim 10$  ns) affecting the small temporal spread ( $\leq 10$  ms) of the ablated materials, the deposition rate can be quite high ( $\sim 10$   $\mu\text{m/s}$ ). As a result, a layer of thin film can be produced with the aid of the preferred layer-by-layer nucleation. In addition, since the deposited particles can be highly energetic (typically 1-10eV in energy), surface diffusion of the adatoms is enhanced, and surface temperatures can be higher than the bulk substrate. These mechanisms can help to lower the substrate temperature needed for crystalline film growth.

As mentioned before, mass removal takes place from the target surface where the laser ablates. The whole process includes various complex mechanisms. At sufficiently high flux densities and short pulse duration, elements in the target get more energy by rapidly heated up. When the target surface material has gained enough energy, particles are dissociated from the target surface. Five mechanisms for the emission of target

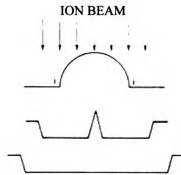
material have been identified as: Collisional, Thermal Evaporation, Electronic Sputtering, Exfoliation, and Hydrodynamic sputtering.

### 1.2.2.1 Collisional

Collisional mechanisms are present for ion and electron bombardment of a target, but not for photon bombardment. Nonetheless, indirect collisional effects do exist with photons. It has been shown that as plasma takes shape during the laser-surface interaction. The plasma formed above the target surface by photon bombardment will include creating electrons and ions, which collisionally interacts with the target.



Higher magnification views of cone structures.



Sketches relevant to the evolution of an asperity on an ion-bombarded surface.

**Figure 9.** Formation of cone structures during laser ablation, indicating a collisional interaction of particles with the target surface [31].

$$\hat{E} = \frac{2E_1^2}{m_2c^2} + \frac{4M_1M_2E_1}{(M_1 + M_2)^2} = \frac{E_1^2}{M_2} \times 2.147 \times 10^{-9} + \frac{4M_1M_2E_1}{(M_1 + M_2)^2} \text{ in eV} \quad \text{Equation 23}$$

$\hat{E}$  refers to the maximum energy transfer,  $E_1$  represents the binary collision between a particle with energy, and  $m_1$  is rest mass,  $m_2$ , a target atom of mass.  $M_1$  and  $M_2$  are the atomic weights of the two particles.

### 1.2.2.2 Thermal Evaporation

Thermal evaporation may require temperatures well above the melting or boiling points. Thermal evaporation commonly indicates a process during which the laser energy is converted to the lattice vibration energy proceeding to the bonds breaking. Some atomic-sized materials from the target surface will be released thereafter.

Kelly and Rothenberg (1985) used the following equation describing thermal sputtering which is based on the application of the vaporizing flux from a condensed phase:

Vaporizing flux = condensing flux

$$\begin{aligned}
 &= p(2\pi m k_B T)^{-1/2} \\
 &= p_0 \left\{ \exp \frac{-\Delta H_v}{k_B T} \right\} \times (2\pi m k_B T)^{-1/2} \text{ atoms} / \text{m}^2 \text{ s} \quad \text{Equation 24}
 \end{aligned}$$

where  $p$  is the pressure under the condition of the existence of the equilibrium vapor,  $p_0$  is a constant, and  $\Delta H_v$  is the heat of the vaporization while the condensation efficiency is assumed to be unity. The total loss from the target is demonstrated as

$$\text{Depth/pulse} = \frac{p_0}{n_c} (2\pi m k_B)^{-1/2} \times \int_0^\infty \exp\left(\frac{-\Delta H_v}{k_B T}\right) T^{-1/2} dt \quad \text{Equation 25}$$

where  $n_c$  is the number density of the condensed phase.

$$\text{Depth/pulse} \approx (\hat{p}_{atm} \hat{T}^{1/2} \tau / M^{1/2} \Delta H_v) \times 1.53 \times 10^6 \text{ m/pulse} \quad \text{Equation 26}$$

where  $\hat{T}$  is the maximum surface temperature,  $M$  is the molecular weight of the vaporizing species, and  $\Delta H_v$  is in electron volts.

**Table 3.** Temperature of metling, Boiling, and a Vaporization Rate of 1 nm/pulse for Selected Solids. [31]

Solid	Melting Point (K)	Boiling Point at 1atm (K)	Temperature for a Vaporization Rate of 1nm/pulse (K)
Au	1336	3133	4600
Si	1685	1685	4600
MgO	3098	3530	4200
SiO <sub>2</sub>	1995	3200	3800

In fact, the vaporizing flux equation is a standard thermal evaporation formula and the condensation efficiency is one, or unity.

### 1.2.2.3 Electronic Sputtering

Electronic sputtering involves the electronic excitation which leads directly to the bond breaking. The electronic excitation begins with the absorption of the laser energy, which results in the excitation of the outer shell electrons. The atoms and ions are liberated if the excitation energy is greater than the binding energy. For example, a laser of wavelength  $\lambda = 248\text{nm}$ ,  $h\nu = 5.01 \text{ eV}$ , so for materials with the bandgaps less than 5



eV, each photon can excite an electron across the bandgap. One characteristic of this mechanism is the existence of a threshold energy density for the particle emission.

#### 1.2.2.4 Exfoliation

Exfoliation of materials can occur when a target is repeatedly thermally shocked yielding flakes of materials that break from the surface. It typically occurs when the system has a high linear thermal expansion ( $\Delta L/L$ ), where  $L$  is the thickness that is heated and  $\Delta L$  is the change in thickness, a high Young's modulus ( $E$ ), a high melting point ( $T_M$ ), and the laser-induced temperature excursions approach but do not exceed  $T_M$ . The thermal shocks occur repeatedly and, since they are not relieved by melting under the above conditions, they eventually lead to cracking.

According to the argument of Kelly, the thermal shock can be measured in terms of thermal stress which can be expressed as

$$\text{stress} = \frac{E\Delta L}{L_0} \quad \text{Equation 27}$$

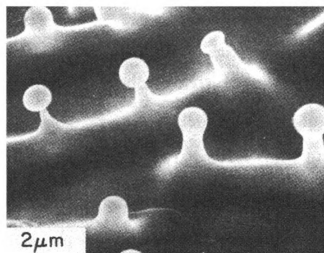
**Table 4.** Quantities needed for evaluating thermal stress by means of Equation 5 [31].

Solid	Linear Thermal Expansion of the Solid of solid	Young's Modulus, E ( $10^{10} \times \text{Pa}$ )	$E\Delta L/L_0$ ( $10^{10} \times \text{Pa}$ )
Au	0.018	8.0	0.12
Si	0.0054	11.3	0.06
MgO	0.045	26	1.2
SiO <sub>2</sub>	0.00077	7.2	0.006

Evidenced from the table, exfoliation sputtering will not occur with low melting metals. In addition, due to the influence of the low thermal stress, gold and silicon, in particular, are not expected to experience exfoliation sputtering.

#### 1.2.2.5 Hydrodynamic Sputtering

Hydrodynamic sputtering comprises the formation of droplets on the surface of the target material caused by surface melting, and the eventual expulsion of droplets as a consequence of the transient melting.



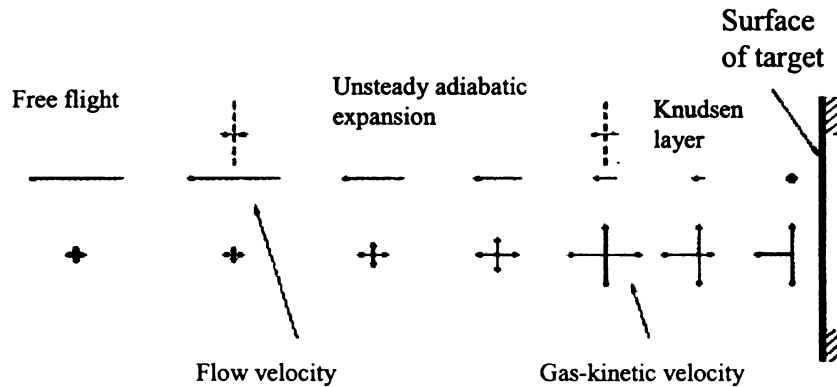
**Figure 10.** Droplet formation in the gold target. Sputtering of polycrystalline Au in air after 4320 pulses from an ArF excimer laser (193nm) of 12 ns and  $2.5\text{J}/\text{cm}^2$ . (From Kelly et al. 1985)

#### Plasma gas-dynamic expansion

Semiquantitative models have provided expressive power for the expansion dynamics of a laser-generated plasma plume. Gas dynamics are deemed to be a factor influencing spatial and velocity distributions and the hydrodynamic equations can be

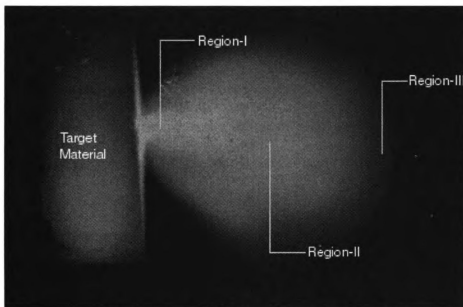
used to model the gas cloud moving away from the target. The model is focused on analyzing the density of the gas that is time-and space-dependent and the angular velocity distribution of the ejected particles. In the simulation process, the particle motion is developed in the direction  $x$ -axis perpendicular to the two lateral directions of the target plane,  $y$  and  $z$ . The process can be divided into following steps: interaction of the laser with the target resulting in the formation of the plasma, the isothermal expansion, and the adiabatic expansion of the gas cloud.

According to the above illustration, the first two regimes take place during the laser pulse, and the latter one is especially applied after the laser pulse is over. In the isothermal expansion, since the description of the relation between mass, momentum and plasma energy is required, the gas-dynamic equations of mass and momentum conservation are preferred. The velocities are determined by the pressure gradient, which influences the development of the expansion into an anisotropic form. When the laser pulse ends, the regime changes to the unsteady adiabatic expansion (UAE), in which no injection of particles is considered into factors controlling the expansion.



**Figure 11.** Plasma gas-dynamic expansion [31].

The dimensions of the gas cloud govern the expansion of the plasma in three directions once it is formed. For example, when the influence from the target is large, the highest velocities are in the direction of the smallest dimensions and vice versa, which helps produce an ellipsoidal plume that is stretched out from the surface. In addition, transverse expansions are created, which are determined by two lateral dimensions of the gas cloud when the plume is close to the target. In this situation, the forward expansion is the preferred direction. For example, an elliptical plume is produced by a symmetrical, or circular, spot. Nonetheless, in the situation of the non-symmetrical spot, the expansion velocity is larger for the direction where the spot is smaller initially. At that time, due to the influence of the laser spot anisotropy, the pseudorotation, or flip-over, of the plume shape will take place.



Laser produced plasma plume from a metal target

**Figure 12.** Laser produced plasma plume from a metal target [32].

In terms of physical composition, the laser induced plasma can be divided into three regions as shown in the above image.

Region-I is the essential part, in which the emission of the plasma occurs close to the sample surface. In the sample surface, the temperature is set at maximum and nearly all the species are in ionized state.

Region-II is the middle region, in which both neutral and a certain number of molecular species appear with the exception of ionized species.

Region-III is the extended region of the plasma. In this region, the plasma temperature is lower compared with other two regions, and the molecular species with larger density are present.

### **1.2.3 Particulates generated by pulsed laser deposition**

In general, the quality of the deposited film is mainly determined by the crystallinity of the lattice and the surface smoothness. The generation of particulates by pulsed ablation is the major factor influencing the smoothness of the resulting thin film. To be more specific, the nature of particulates covering the surface of thin films, including the generation rate, the chemistry, the energy, the size, and the microstructure, is determined by the process condition and the type of the material [33]. In particular, in the case of high-performance optical and electronic applications, due to the rigid constraints on surface smoothness, the demand for the particulate density and its size is extremely high.

In the following paragraphs, details about particulates are discussed in five sections. The first is related to their participation characterization.

**Table 5.** The different shape and size between the three phases.

	Solid	Liquid	Vapor
Shape	Irregular	Spherical	Spherical or polyhedral
Size	Sub-micron	Micron	nanometer

Based on the status of the original matter, there are three categories defining particulates produced by pulsed laser ablation, especially at the moment when they are expelled from the target. The original matter could be in solid, liquid, or vapor state. The origin of the particulate generation is multifaceted as shown in the Table 5.

The second section is pertinent to the chemistry of particulates. Since it was found that films produced by PLD process have chemistry quite similar to that of the target, a mechanism meant to create an environment inducing the exhaustion of lower melting temperature element in the particulates is viable. According to this mechanism, the composition of the ejected liquid droplet positioned above the surface is hypothesized to be fairly similar to that of the target. In addition, the depletion of the low melting temperature element takes place principally as it is moving close towards the substrate. For example, in the case of a particulate of radius  $r$ , a depletion layer of thickness is assumed to be  $l$ , hence, the normalized resultant content of the depleted element can be obtained as

$$\frac{RESULTANT\%}{INITIAL\%} = \left(\frac{r-l}{r}\right)^3 \quad \text{Equation 28}$$

In the third section of the characteristic of microstructures, the focus is on the cooling rate that is found to be an important factor deciding the microstructure of

particulates. The reason is that particulates become solid as a result of molten droplets ejected from the target. Currently, the cooling rate is measured by two different methods. When the ablation experiment is operated in vacuum, cooling is mainly noticed as radiant rather than convective. Put it in simples, the cooling rate can be expressed as

$$T = \left( \frac{6}{D \rho C_p} \right) \varepsilon \sigma (T^4 - T_0^4) \quad \text{Equation 29}$$

where  $D$  is the particulate diameter,  $\rho$  is the material density,  $C_p$  is the heat capacity of the material,  $\varepsilon$  is the radiant emissivity,  $\sigma$  is the Stefan-Boltzmann constant,  $T$  is the temperature of the particulate, and  $T_0$  is the surrounding temperature. From this formula, it is known that as the cooling rate is high, the solidified particulates tend to have finer microstructures. Moreover, this formula is also applicable to the conventional powder production process, such as atomization and splat quenching.

The fourth part of the discussion is focused on the effects of processing parameters, two of which are the laser fluence and the laser wavelength. In the situation of using a specific material and setting the laser wavelength within a certain range, the laser fluence on the target was found to be able to exert most significant effect on the particulate size and density. Fluence, which is to specify the energy delivered in a given time, provides a powerful foundation deciding how much the tissue will be heated by the laser pulse. Higher fluence means more heating is required, which has more effect on the tissue. Among the various factors related to the setting of treatment levels, the laser fluence is deemed as the most influential one. The laser fluence is measured in joules per square centimeter, rather than the power or pulse energy per unit area as in the case of usual definition. The fluence is derived from dividing the pulse energy by the area of the spot, whose size has determining power on the fluence. In other words, varying the laser

power or the laser spot size can result in changes in the laser fluence. Usually, if the laser power is set constant, the particulate number density is higher with tighter focus. Particularly, a threshold laser fluence exists, below which the particulates are negligible.

In addition, the impact of the laser wavelength  $\lambda$  on the effectiveness of the absorption of the laser power into the target has been observed. In certain cases of metals, the absorption coefficient  $\alpha$  decreases with the declining  $\lambda$ , which leads to a larger laser penetration depth in metals in the Ultraviolet (UV) range compared with that in the infrared (IR) range. Aside from these observations, for other materials, by taking different absorption mechanisms into account, such as lattice vibration, free carrier absorption, impurity centers, or bandgap transition, the definition of the relationship between the absorption coefficient and wavelength is far more complex. For example, in the case of oxide superconductors, unlike the above conclusion obtained from metals, the laser penetration depth appears to be larger in the near IR than in the UV range. On the whole, it is estimated that the principle impact that the laser wavelength has on the generation of particulates is ascribed to the difference in the absorption coefficient when various laser wavelengths are used.

In the final section, the target-to-substrate distance is discussed, whose effect is reflected in the angular spread of the ejected flux if the film is deposited in vacuum. At a larger target-to-substrate distance, or with the influence from the ambient pressure, particulates might occur; especially diverse types of particulates may emerge depending on the position of the substrate. This situation usually arises during the PLD process conducted in a poor vacuum. Normally, particulate trajectories are in various directions



if a defocused laser beam is used, compared with the condition in which an extremely focused beam is used to help generate a collimated jet of particulates.

In fact, the effects of the target-to-substrate distance and the ambient pressure could be interrelated. The improved collisions between the laser-produced plumes will affect the increase of the background gas pressure. This argument is supported by the study of Dyer et al (1990). According to their investigation,  $E/P_0$  is used as a scaling parameter for measuring the plume range, where  $E$  is the laser-pulse energy and  $P_0$  is the background gas pressure. Furthermore, the length of the plume can be explained by  $L \propto (E/p_0)^{1/3\gamma}$ , where  $\gamma$  represents the ratio of specific heats of the elements in the plume. If the target-to-substrate distance is greatly smaller than  $L$ , there are no discernible changes in the particulate size and the density. Nonetheless, when the target-to-substrate distance increases, the quantity of smaller particulates will decline compared with that of entire particulates. Then, a few larger particulates will emerge, which implies a merge takes place during flight. Moreover, as soon as this distance is large enough, or the substrate is located far beyond  $L$ , the adhesion to the substrate is reduced to a certain degree. The substrate is composed of the ejected matter, including the particulates and atomic species.

### 1.3 Thermodynamic and chemical potential

In terms of being predictive of whether an alloy is in equilibrium, thermodynamics is deemed to be a useful tool, especially during phase transformations in which changes toward equilibrium are usually the main concerns. In fact, this is also the main contribution that thermodynamics has made to physical metallurgy [34]. In normal situation under which the temperature and pressure is constant, the relative stability of a system during phase transformations is determined by its Gibbs free energy ( $G$ ). The Gibbs free energy of a system is defined by the equation

$$G = H - TS \quad \text{Equation 30}$$

where  $H$  is the enthalpy,  $T$  the absolute temperature, and  $S$  the entropy of the system. Enthalpy is a measure of the heat content of the system and is induced by the following equation

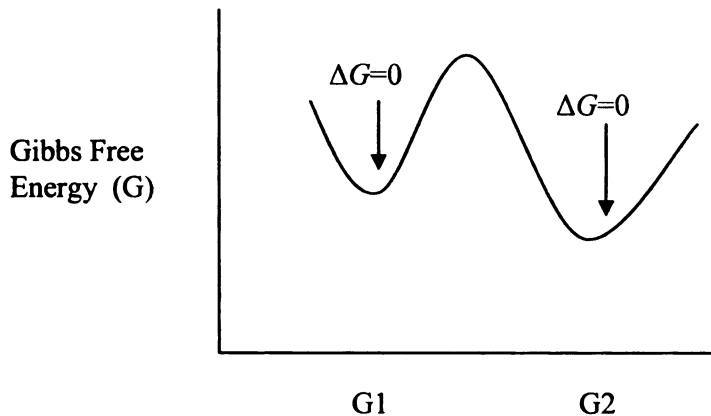
$$H = E + PV \quad \text{Equation 31}$$

where  $E$  is the internal energy of the system,  $P$  the pressure, and  $V$  the volume. The internal energy occurs from the total kinetic and potential energies of the atoms within the system. There are two sources of the kinetic energy, one of which is from the atomic vibration in solid or liquid status. The other one is from translational and rotational energies for the atoms and molecules within a liquid or gas. In the latter condition, the interactions between the atoms within the system give rise to the desired energy. Moreover, changes in the internal energy and the volume of the system will determine the status of the absorbed or evolved heat when a transformation or reaction takes place. Then, this situation can be applied to the two factors, pressure and volume, made of the term  $PV$ , and result in the condition that, at constant pressure, the heat absorbed or

evolved is produced corresponding with the change in  $H$ . Usually,  $PV$  is comparatively small with  $E$  when operating under condensed phases, including solids and liquids, which lead to the possible difference between  $H$  and  $E$ . The remaining factor that is related to the term  $G$  is  $S$ , the entropy of the system, which is to measure the randomness of the system.

A definition of a system to be in equilibrium means it is in the most stable state,. Applying the laws of classical thermodynamics, a closed system, such as through the fixed mass and composition, if set at constant temperature and pressure, will be in equilibrium with the aid of the lowest possible value of the Gibb free energy, or  $\Delta G = 0$ . According to the definition of  $G$ , if the state is described to be at the highest stability, at the minimum energy caused by a low enthalpy and high entropy. At low temperatures, since solid phases have the strongest atomic binding, which is contributive to the lowest internal energy, they are preferably stable. On the other hand, at high temperatures, phases are influenced by the negative product of the absolute temperature,  $T$ , and the entropy of the system,  $S$ , and therefore are demonstrated with most stable state characteristic of more freedom of atom movement, liquids and gases.

The following chart illustrates the lowest possible free energy defining the equilibrium condition.



**Figure 13.** Variation of Gibbs free energy with the arrangement of atoms. Schematically, the configuration G2 has the lowest free energy which results in a system that is at stable equilibrium. The configuration G1 is a metastable equilibrium.

If placing these configurations onto the Figure 13, in which different atomic configurations can be represented by points along the abscissa, the configuration G2 would be seen to be at the stable equilibrium state. At this point, minor changes in the arrangement of atoms to a first approximation create merely no changes in G, which could be representative of the example of  $\Delta G = 0$ . Nonetheless, if desiring to create the value  $\Delta G = 0$ , other arrangements, such as G1, could potentially make contributions by which placing at a local minimum in free energy and therefore also satisfying  $\Delta G = 0$ . This condition, however, does not have the lowest possible value of G. The condition at G1 is called a metastable equilibrium state. In reality, during the states for which  $\Delta G \neq 0$ , called intermediary states, the unstable status could be only realized lasting a short period of time. On the other hand, if the effect of thermal fluctuations on the arrangement of atoms is sufficiently high, atoms can rearrange into one of the free energy minima. A

system can transform into a new stable (or metastable) equilibrium state with a change of temperature or pressure.

Since any transformation leading to a decline in Gibbs free energy is possible, a definite criterion for any phase transformation is

$$\Delta G = G_2 - G_1 < 0 \quad \text{Equation 32}$$

where  $G_1$  and  $G_2$  represent free energies of the early and final states, respectively. Being able to skip a series of intermediate metastable states, the transformation could arrive at the stable equilibrium state directly.

By definition, the intensive properties of a system refer to those that are independent of the size of the system, such as  $T$  and  $P$ , while the extensive properties are those that are changing in proportion to the quantity of materials in the system, such as  $V$ ,  $E$ ,  $H$ ,  $S$  and  $G$ .

### 1.3.1 Binary solutions

Similar with single component systems, in which all phases have the same composition and the equilibrium simply encompasses pressure and temperature as variables, the composition is also variable in the case of alloys. Nonetheless, in order to understand phase changes in alloys, an appraisal of how the Gibbs free energy of a given phase is required, which is determined by the composition, the temperature, and the pressure.

### 1.3.1.1 The Gibbs Free Energy of Binary Solutions

In order to obtain the Gibbs free energy of binary solutions in alloys, a calculation of individual atoms in the system is necessary, which is derived from the free energies of pure atoms. For example, during the mixing of atom A and B, the two materials are mixed to create a solid material, or the system, in a flexible way, which is to set one mole mixed with X mole of A and Y mole of B. The following formula can demonstrate the relationship between X and Y

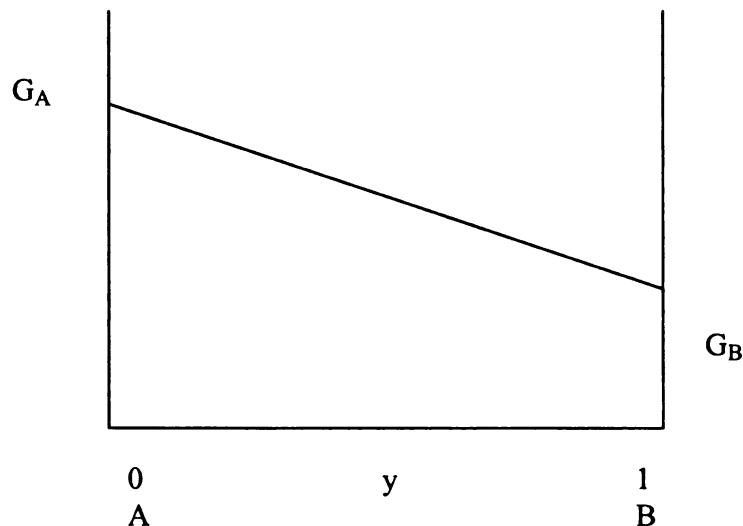
$$X + Y = 1 \quad \text{Equation 33}$$

where X represents the mole fraction of A in the alloy and Y is the mole fraction of B.

Thus, the total free energy of the system before the process of mixing is shown as

$$G_{total} = XG_A + YG_B \quad \text{Equation 34}$$

where  $G_A$  is the free energy of material A and  $G_B$  is the free energy of material B



**Figure 14.** Variation of  $G_1$  (the free energy before mixing) with alloy composition.

Due to the difference in Gibbs free energy, during the mixing process, the total free energy of the system will not remain stable, such that after the mixture is formed, the total free energy becomes  $G_{total}'$

$$G_{total}' = G_{total} + \Delta G \quad \text{Equation 35}$$

where  $\Delta G$  is the difference in Gibbs free energy before and after the mixing.

Combining the condition of  $G_{total} = H - TS$ ,  $G_{total}' = H' - TS'$ , and  $\Delta H = H' - H$  and  $\Delta S = S' - S$ , we could get the following conclusion

$$\Delta G = \Delta H - T\Delta S \quad \text{Equation 36}$$

$\Delta H$  represents the change in heat during the process of mixing as well as the change in internal energy (E) which is caused by the mixing. On the other hand,  $\Delta S$  refers to the difference in entropy before and after the mixing.

### 1.3.2 Chemical Potential

By definition, the chemical potential of a fixed entropy and a volume thermodynamic system refers to the possibility of energy changes in the system with the introduction of an additional particle. If a system has various species of particles, a variety of different chemical potentials would take place, which is associated with each species of particles respectively. In the situation, the change in energy is explained by the growing number of the particles of that specific species which is increased by one. In terms of the investigation of systems composed of reacting particles, the chemical potential is especially critical. For example, in the case of two species 1 and 2, particles belonged to species 1 can transform into those of species 2 and vice versa. A

supersaturated design mixed with water liquid (species 1) and water vapor (species 2) can exemplify this kind of situation.

According to the second law of thermodynamic, which states that heat plays an important role in energy conversions in that all forms of energy can be converted into heat, nonetheless, the reverse process cannot be realized by way of transforming the converted heat back to its original form. In other words, the conversion process involving heat cannot be initiated without loss. Based on this fact, any increase in one chemical potential would lead to a net release of energy of the system in the form of heat, during which the species of increased potential transform into the other species. Similarly, if the reverse transformation occurs, a net gain of energy would emerge in the form of heat. If the system is in equilibrium, the chemical potentials of the two species should have been equal. In the case of alloys, if atoms are added or removed, understanding how the free energy of a given phase will change is meaningful. For instance, if  $dn_A$  moles of species A, is added or removed to a large amount of a phase at constant temperature and pressure, the size of the system will increase by  $dn_A$ . Thus, the total free energy of the system will increase by  $\Delta G'$ .

More importantly, if  $dn_A$  is small enough,  $\Delta G'$  will be produced in proportion to the amount of A that is added. Following this rationale, we can get the equation shown as

$$\Delta G' = \mu_A dn_A \quad \text{Equation 37}$$

where  $\mu_A$  is called the partial molar free energy of A, or the chemical potential of A in the phase, with the proportionality set as constant. Since  $\mu_A$  is determined by the



composition of the phase,  $dn_A$  must be small enough not to influence the change in the composition.

$$\mu_A = \left( \frac{\partial G'}{\partial n_A} \right)_{T, P, n_B} \quad \text{Equation 38}$$

The symbol  $G'$  represents the Gibbs free energy, which could simply refer to the whole system. Usually, since the symbol  $G$  is used to signify the molar free energy, it refers to the fact that it is independent of the size of the system.

## 1.4 Growth Mechanism

### 1.4.1 Vapor-Liquid-Solid (VLS) Growth Mechanism

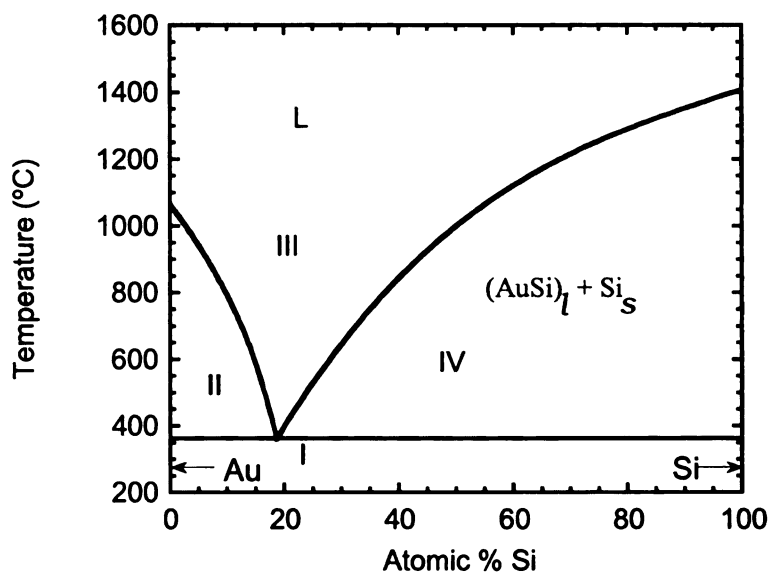
#### Introduction

Normally, the nanowire synthesis involves a vapor phase, such as their growth by means of chemical vapor deposition, physical vapor deposition or pulsed laser deposition. Among the various nanowire growth methods, the vapor-liquid-solid (VLS) mechanism, which was proposed by Wagner et al. as for the growth of single-crystal silicon whiskers, is particular popular [35]. Moreover, Givargizov has developed the growth model and delineated it within the framework of kinetics [36]. The VLS reaction was adopted by Westwater to grow silicon nanowires by using silane as the Si source gas and Au as the mediating catalyst [37].

In the VLS growth mechanism, a liquid metal region is formed by means of raising the temperature of the metal and semiconductor above the eutectic temperature. The liquid metal region also serves as an energetically preferred location supporting the

absorption of gas-phase reactants, which is related to the high sticking coefficient of the molten alloy. At least two basic mechanisms of the eutectic alloy formation can be emphasized currently [38]. The first is the formation of the eutectic alloy. Before the formation of the eutectic alloy, the intermediate layer of supersaturated solid solution is formed which is followed by the growing defects concentration into these layers and the increase of the free energy of the system. Actually, the increase of the free energy is the reason why the eutectic systems are easily melting. Different from the first mechanism, there is no formation of solid solution in the second mechanism. Based on the application of the adhesion theory and the mechanism of contact melting, the developing surface force between the atoms in the two surfaces takes place in micro-regions of physical contact between the conjugated crystal phases, and the transition epitaxial zone can be formed without the formation of solid solution. Actually, the formation of these transition epitaxial zones would result in the subsequent reduction of differences in lattices parameters between solid phases at the interface region under the condition of the stress present at the interface. In terms of the metal addition to the target, Wagner and Ellis have made great contributions. According to the study of Wagner and Ellis, since epitaxial structures are defined in location and diameter by the metal catalyst, the addition of such metals would catalyze their growth. The increasing gathering of the semiconductor encourages the achievement of the supersaturation condition in the metal-semiconductor alloy, which prompts the semiconductor phase to detach from the alloy and to form the next epitaxial layer at the base of the liquid. Then the cluster supersaturates and grows into one-dimensional wire of the material, under which the

alloy cluster is produced. Experimental parameters, such as temperature and pressure, and the nature of the metal catalyst determine the formation of the produced wire.



**Figure 15.** Phase diagram for the gold-silicon system.

This phase diagram plots the atomic percentage of Au and Silicon along the X-axis and temperature along the Y-axis. In the Region I, since the temperature in the Au-Si system is set below the eutectic temperature ( $\sim 360^\circ\text{C}$ ), which is the minimum melting temperature of any possible alloy, no molten alloy is formed. The reason is that eutectic implies that an alloy has a sharp melting point. Eutectic, or eutectic mixture, is a mixture of two or more elements which has a lower melting point than any of its components. Moreover, one characteristic of eutectic corresponds with the possibility that specific composition has the lowest melting point of an alloy. For example, if an AuSi alloy has 19.5 atomic % of Si and 80.5 % of Au, it will melt at  $T=360^\circ\text{C}$ . On the other hand, in solid phases composed of solid forms of pure Au and Si, solid up to  $1063^\circ\text{C}$  and  $1412^\circ\text{C}$ ,

respectively, Au and Si will coexist as solids in every atomic percentage of these two elements at the interface between them.

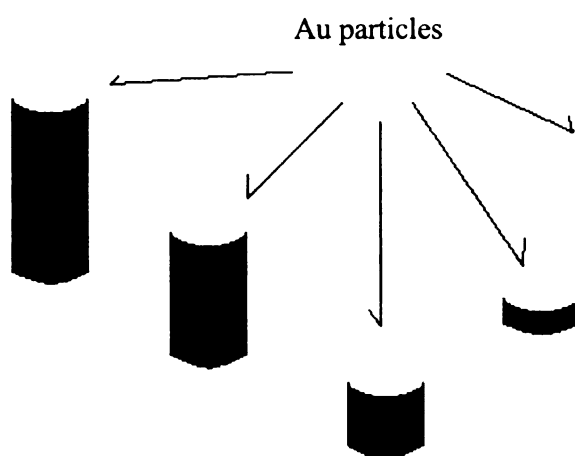
In the Region II, the solid form of gold and silicon starts to form liquid alloy if the following conditions are met: the temperature is higher than eutectic temperature ( $\sim 360^{\circ}\text{C}$ ) and the weight percent concentration of silicon is raised to a certain level, usually 82%. When these conditions are present, a molten alloy would be formed. Region II is a biphasic region; in which the solid gold and Au-Si molten alloy coexist. If more volume of the silicon is added into the system, the molten alloy will absorb more solid gold, which boosts the size of the Au-Si alloy droplet. Due to the characteristic of high sticking coefficient of the molten alloy, in which a large proportion of added atoms are adhering to its substrate, a liquid metal region is formed and provides a place attracting the absorbed gas-phase reactants.

In the Region III, due to the further absorption of atoms from the vapor phase, the silicon percentage will increase with time at certain temperature, which results in the increase of the gold and silicon droplet. The alloy remains liquid within this region while no solid phase exists. Nonetheless, if there are more and more silicon atoms added into the system, the whole system is pushed to fall into the Region IV, in which the solid silicon begins to emerge in the system with other variables, including temperature and pressure, remaining constant.

In the Region IV, the gold and silicon alloy remains in liquid state. With the atomic percentage of silicon increasing, the silicon crystal starts to grow. As the silicon concentration increases over 50 atomic percent at  $1000^{\circ}\text{C}$ , the silicon will begin drop out of the molten alloy as a solid, lowering the concentration of silicon in the melt, and

moving to the left on the phase diagram. Through this mechanism, the diameter of the resulting nanowire depends on the size of the Au-Si droplet. As more silicon added into the system the alloy again supersaturates and more silicon solidifies from the melt in a repetitive manner to continue the nanowire growth. The size of the Au-Si liquid alloy is also determined by the temperature of the substrate. The higher the substrate temperature, the larger the Au-Si liquid alloy becomes, which influences the formation of bigger diameter nanowires.

As the temperature of the system is raised above the eutectic point ( $\sim 360^{\circ}\text{C}$  in Figure 15), a molten alloy is formed. For proper growth of the nanowires it is desired to have the impinging silicon adatoms to preferentially stick at the molten alloy locations. Since the sticking coefficient of a liquid is very high, conditions for reducing the sticking coefficient at all other locations (silicon on silicon) are sought. As described previously, this condition can be met by raising the temperature of the substrate, and thus enhancing the surface diffusion of the adatoms. As the alloy supersaturates with silicon, the solid silicon drops out of the molten alloy to form the next layer of the nanowire, and the molten alloy is pushed to the top of the wire.



**Figure 16.** Gold droplets form an alloy with the silicon. The alloy has a eutectic point near 360°C, above which it is molten.

By using VLS technique, controlling the metal droplet location the location of nanowires can also be controlled. We initially investigated different patterned shapes to see if it was possible to control the location of the metal droplets to specific locations within the pattern.

## Kinetics

In kinetic studies the crystal growth rate is usually measured as a function of the driving force, such as supersaturation. For the growth of whisker, the discovery of the dependent relationship between the axial growth rate and the whisker diameter is especially enlightening. A method has been proposed to sort out the determining factors of the supersaturation and those of the kinetic coefficients of crystallization, under

the condition that the specific energy of the prismatic whisker surfaces is already specified. This method is based on the application of the Gibbs-Thomson equation and certain kinetic laws of growth.

Since the vapor pressure and solubility of Si increase with the diminishing diameter of the whisker, the growth rate decreases under the influence of the decreasing supersaturation. According to Gibbs-Thomson's contention, the decrease of the supersaturation as a function of the whisker diameter can be given as

$$\Delta\mu = \Delta\mu_0 - 4\Omega\alpha/d \quad \text{Equation 39}$$

where  $\Delta\mu$  is the valuable difference between the chemical potentials of Si in the vapor phase and those in the whisker,  $\Delta\mu_0$  is the similar difference at a plane boundary ( $d \rightarrow \infty$ ),  $\alpha$  is the particular free energy of the whisker surface, and  $\Omega$  is the atomic volume of Si.

Since the dependence of the growth rate  $V$  on the supersaturation  $\Delta\mu/kT$ , where  $k$  and  $T$  have the usual implications, is unidentified in advance, experimental data must provide related information effectively. For the singular faces, the dependence is not linear and, however, in many cases is of  $n$ th power

$$V \sim (\Delta\mu/kT)^n \quad \text{Equation 40}$$

This proportionality can be expressed as an accurate equation:

$$V = b(\Delta\mu/kT)^n \quad \text{Equation 41}$$

where  $b$  is the coefficient independent of the supersaturation. Based on this equation, it is concluded that this independence can be used as a criterion determining  $n$  from experiments. Furthermore, substituting  $\Delta\mu$ , we can obtain

$$V^{1/n} = \frac{\Delta\mu_0}{kT} b^{1/n} - \frac{4\Omega\alpha}{kT} b^{1/n} \frac{1}{d} \quad \text{Equation 42}$$

which is equivalent to a linear dependence of  $V^{1/n}$  opposed to  $1/d$ .

#### 1.4.2 Solid-liquid-solid growth mechanism

Solid-liquid-solid is corresponding to the mechanism making use of the sequence of vapor –liquid –solid. In the case of Ni thin film on Si (111), due to the relatively high solubility of Si in Si<sub>2</sub>Ni eutectic alloy, more Si atoms will diffuse through the solid (substrate)-liquid interface into the liquid phase, such as Ni-Si droplets. A second liquid-solid (nanowire) interface will take shape when the liquid phase becomes supersaturated owing to thermal or compositional fluctuations, which leads to the growth of SiNWs. Since this growth process involves the phase changes of solid-liquid-solid, it is named as the SLS growth, which is actually equivalent to the VLS mechanism.

From a kinetic perspective, due to the fluctuation in Si-Ni liquid droplets, the concentration gradient and the supersaturation are driving forces for this uninterrupted diffusion of Si atoms from the substrate through the substrate-liquid interface to the liquid droplets, and then through the liquid droplets-nanowires to load themselves onto nanowires. On the other hand, the carrier gas Ar<sub>2</sub>/H<sub>2</sub> will run into the surface of the semisphere-shaped Si-Ni liquid droplets, and will swap energy and momentum with atoms at the surface of the Si-Ni nanoparticles, stimulating the occurrence of overcooling at the surface of the droplets. This overcooling is vital to commence a favored unidirectional growth of a-SiNWs.



### 1.4.3 Oxide assisted growth

#### Introduction

Supported by the result of the experiment which showed that the metal catalyst was not observed in Si nanowires even when metals were mixed in the target, a different model has been proposed. Moreover, it was discovered that metal was not a necessary component of the Si nanowire synthesis through laser ablation. Instead, SiO<sub>2</sub> was the special and effective catalyst, which could fundamentally improve the growth of Si nanowires [39].

In this oxide-assisted growth (OAG) method, oxides, rather than metals, play an important role in inducing the nucleation and the growth of nanowires [40]. Because of the metal-free property, OAG not only supports large-quantity production of nanowires with controllability, but also yields nanowires characteristic of metal-free high purity.

The understanding of the OAG mechanism still has not developed into mature stage. Nonetheless, based on the success of the growth of nanowires from different materials, this growth mechanism deserved better attention.

#### Methods

S. T. Lee etc. [40] contended that the growth mechanism is assisted by silicon oxide. Specially, the vapor phase of  $Si_xO$  ( $x>1$ ) generated through thermal evaporation is the main determinant. It is assumed that the nucleation of nanoparticles generally takes place

at the substrate by means of different decompositions of silicon oxide at the relatively low temperature of 930°C as shown below.



and



These decompositions lead to the precipitation of silicon nanoparticles, such as the nuclei of Si nanowires, which are covered with shells of silicon oxide as observed.

Essentially, a large amount of Si nanowires have been synthesized through thermal evaporation by mixing silicon and SiO<sub>2</sub> powder. In order to form Si nanoparticles, or nuclei of nanowires, Si oxide vapor generated from the powder mixture first condensed on the substrate and then decomposed. A Si nanowire nucleus was composed of a polycrystalline Si core with a high density of defects and a silicon oxide shell. The growth mechanism was proposed to be properly associated with the imperfect structure of Si crystal cores and SiO.

During evaporation, since  $Si_xO$  vapor was recurrently generated, the nucleation could occur with different crystalline directions, either on the side surfaces or the tips of nanowires. If the nucleation takes place on the side surfaces, the forking of the nanowires is often observed. On the other hand, if it takes place on the tips of nanowires, a re-nucleation will occur. Especially, since the nuclei formed on the tips in an adverse growth direction could not grow fast, a re-nucleation shall inevitably occur again, which will lead to the formation of nanoparticle chains.

## **Nanowires**

Nanowires of different materials utilizing this method have been grown primarily either by thermal evaporation or laser ablation. For example, Si nanowires have been synthesized through thermal evaporation by mixing silicon and  $\text{SiO}_2$  powder [39,40]. In a similar fashion, the synthesis of MgO nanorods has been achieved by mixing Mg and CuO powder [41], and ZnO nanowires are the production by combining ZnO and  $\text{SnO}_2$  [42].

## **1.5 Vacuum Sciences**

### **The kinetic theory of Gasses**

The kinetic theory of gases was initially developed by Maxwell and was then investigated extensively by many following investigators. The main contribution of this theory lies in its useful explanations for both the bulk properties of a gas and the transport properties. The former includes elements such as the pressure, molecular impingement rate, and the distribution of molecular velocities, while the latter involves viscosity, thermal conductivity, and diffusion. This division is based on the employment of dynamics of the motion of individual molecules.

Essentially, the basis of the kinetic theory of gases is in close relation to two primary assumptions. The first premise hypothesizes that molecules of a gas are in constant motion, and this motion is significantly connected with macroscopic properties known as the temperature and pressure, distinguishing the state of the gas within a specific small region. The second hypothesis is that gas is composed of small particles.

In the gaseous state, these particles are monatomic or polyatomic molecules at moderate temperatures while at higher temperatures, they may be fully unconnected and transformed into atoms or even into positive ions and electrons in order to give shape to plasma.

It is assumed that the core of a mass of the molecule is moving toward the same direction with a constant velocity between collisions with other molecules. The forces between molecules are barely noticed only when the distance between the molecular centers and molecules is reduced to the range known as the mean molecular diameter. Velocity is viewed as a vector which must be measured in relation to some rigid reference frame. The magnitude of the velocity vector is defined as the speed of the molecule. Since kinetic energy is proportionally related to the square of the molecular velocity, it is a scalar quantity.

By definition, temperature is quantity proportional to the average kinetic energy of the translation of the particles in a reference frame, which is moving with any fluid flow within a specific small region. In the case of monatomic molecules, the effect of increased temperature is mainly discerned through amplified translational energy of the molecules. On the other hand, as for diatomic and polyatomic molecules, increased rotational energy of the molecule approximately one or more axes and increased vibrational energy of the component atoms regarding mean positions of equilibrium are both originated from increased temperatures by means of intermolecular collisions. The assumptions involved in this model are as follows:

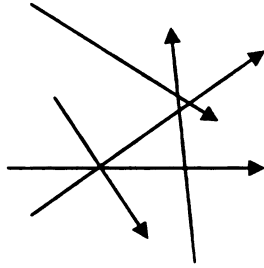
- 1 Any fixed volume of gas incorporates a great deal of molecules.

- 2 The influence of molecules only emerges when molecules collide. Between collisions with each other or with the container walls, they travel in the straight direction.
- 3 All directions of molecular velocities are of identical possibility.
- 4 Collisions of one molecule with another or with surfaces that are positioned open to the gas are entirely flexible. All surfaces are regarded to be smooth.
- 5 Although there are any possible magnitudes in relation to the speed of a given molecule, the number of molecules with speeds in a specific range is constant with time.

#### **1.5.1 Rate at Which Molecules Strike A Surface.**

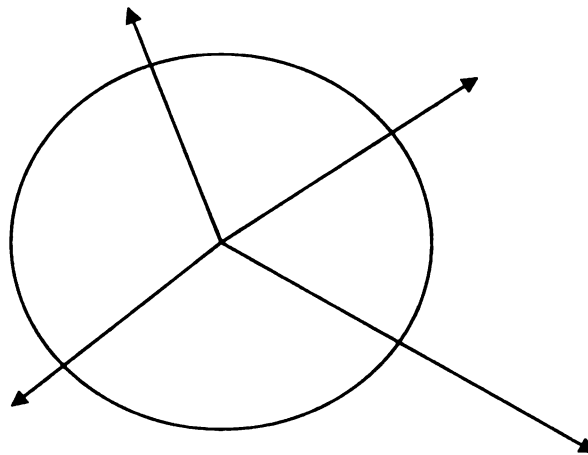
In order to study the role of pressure in the kinetic theory, the discussion about the molecular impingement rate is critical. The impingement rate refers to the number of gas molecules that hit a specified area in the system per unit time. The molecular impingement is adopted to formulate pressure in the kinetic theory. It is usually stated in units of *molecules / sec-cm<sup>2</sup>*.

As described in the Assumption 3, in Figure 17 all directions of molecular velocities are consistently probable, which considers the same probability of all directions of molecular velocities.



**Figure 17.** All directions of molecular velocities are consistently probable.

A vector always represents the direction and the magnitude of its velocity. We can relocate all vectors to a common origin and to a sphere of radius built close to this origin, shown as follows:



**Figure 18.** A vector always represents the direction and the magnitude of its velocity.

In this structural expression, the velocity vectors cross the surface of the sphere at many points, equivalent to the number of molecules intersected in the system. The average number of intersections per unit area is expressed as:

$$\frac{N}{S} = \frac{N}{4\pi r^2} \quad \text{Equation 45}$$

Hence, the number of intersections on any part of the surface of the sphere,  $dS$ , is

$$dN = \left( \frac{N}{4\pi r^2} \right) dS \quad \text{Equation 46}$$

which is independent of where  $dS$  is located on the sphere.

Expanding this formulation further and defining a specific surface element,  $dS$ , in terms of the polar coordinates  $\theta$ ,  $\phi$ , an equation can be developed as follows:

$$dS = r^2 \sin \theta d\theta d\phi \quad \text{Equation 47}$$

representing the number of molecules whose velocity vectors intersect this constituent of area. This indicates the number of molecules whose velocities are directed within a polar angle from  $\theta$  to  $\theta + d\theta$  and azimuthal angle from  $\phi$  to  $\phi + d\phi$ , which is called  $d^2N_{\theta,\phi}$  is where

$$d^2N_{\theta,\phi} = \left( \frac{N}{4\pi} \right) (\sin \theta d\theta d\phi) \quad \text{Equation 48}$$

The result mentioned above can be used to identify the molecular impingement rate, the rate at which molecules from the gas run into a unit area of the surface that are exposed to the gas, either the container surface or any area made within the bulk of the gas. Consequently, this could be realized by assuming a random element,  $dA$ , of any

surface exposed to the gas, and making a line normal to the plane of  $dA$ , and a reference plane posed at a 90 degree angle against the normal.

$$\begin{aligned} N_{\theta,\phi,v} &= d^3 n_{\theta,\phi,v} dv \\ &= dA dt \left( \frac{v dn_v}{4\pi} \right) \sin \theta \cos \theta d\theta d\phi \end{aligned} \quad \text{Equation 49}$$

$$I_{\theta,\phi,v} = \frac{N_{\theta,\phi,v}}{dA dt} = \left( \frac{1}{4\pi} \right) v dn_v \sin \theta \cos \theta d\theta d\phi \quad \text{Equation 50}$$

By integrating the equation above with respect to  $\theta$  from zero to  $\pi/2$  and respect to  $\phi$  from zero to  $2\pi$ , yielding

$$I_v = \left( \frac{1}{4\pi} \right) v dn_v (2\pi) \left( \frac{1}{2} \right) \quad \text{Equation 51}$$

So the total impingement rate for all molecules, irrespective of their speeds, is

$$I = 1/4 \int v dn_v \quad \text{Equation 52}$$

We can rewrite the equation in terms of  $\omega$  as

$$I_{\theta,\phi,v} = \left( \frac{1}{4\pi} \right) v dn_v \cos \theta d\omega \quad \text{Equation 53}$$

The total impingement rate for all velocities per unit solid angle is thus

$$I_\omega = \left( \frac{1}{4\pi} \right) \cos \theta \int v dn_v \quad \text{Equation 54}$$

$$I_\omega = \frac{1}{4} n \bar{v} \frac{\cos \theta}{\pi} \quad \text{Equation 55}$$

This is known as the Cosine Law or Cosine Rule.

### 1.5.2 Ideal Gas Law Pressure

Understanding of the impingement rate may be beneficial to developing an expression for the pressure influencing the container walls originated from the collisions of the gas molecules with the walls. The pressure refers to either the force exerted per



unit area by the gas molecules on the walls of the container or the rate at which the momentum is transmitted to the unit area of wall surface.

$$p=nKT \quad \text{Equation 56}$$

According to the kinetic theory, due to the impact of molecules on the confined walls, a gas yields a pressure on these walls. Since during the process of the gas exerting pressure on the inactive solid wall of the enclosure, no energy is lost from the gas, it appears that each molecule is projected back from the wall with the same speed as that with which it strikes, but in the reverse direction regarding the normal. In other words, these resulting impacts are absolutely elastic.

It is hypothesized that a molecule of a mass  $m$  moves toward a smooth wall surface belonging to the  $x, y$  plane with the velocity component,  $v_z$ , vertical against the wall. Since the rebounding rate of a molecule is consistent, the change of momentum per impact is  $2mv_z$ . Then there are  $\nu$  molecules striking the unit area, which results in  $2mv_z\nu$ . Nonetheless, the pressure,  $P$ , on a wall is known as the rate at which the momentum is lent to a unit area of surface. Therefore,

$$2m\sum v_z\nu = P \quad \text{Equation 57}$$

where the summation is total values of  $v_z\nu$  and all molecules are presumed to have the same mass  $m$ .

The final step is to calculate  $\nu$ . Among all of the molecules within a volume  $\Delta V$  stretching out from a small area,  $\Delta x\Delta y$ , of the wall by a distance  $|v_z dt|$ , where  $dt$  is a short interval of time. In equilibrium, only a half of the molecules will be moving with velocity components  $v_z$  toward the wall. Let  $n_z$  represent the number of molecules per

unit volume in the gas within  $\Delta V$  that have a velocity component of either  $v_z$  or  $-v_z$ .

Then the flux rate against the wall will be  $\nu = n_z v_z / 2$ , and  $2m \sum \nu_z V = P$  becomes

$$P = m \sum n_z v_z^2 \quad \text{Equation 58}$$

The sum of the speed of a molecule with velocity components is the square root of the quantity

$$v^2 = v_x^2 + v_y^2 + v_z^2 \quad \text{Equation 59}$$

Defining the averages

$$\langle v_x^2 \rangle = (\sum n_x v_x^2) / n, \quad \text{Equation 60}$$

$$\langle v_y^2 \rangle = (\sum n_y v_y^2) / n,$$

$$\langle v_z^2 \rangle = (\sum n_z v_z^2) / n,$$

where  $n$  is the total number of molecules per unit volume without considering velocity

components. The following symmetry could be derived accordingly  $\langle v_x^2 \rangle = \langle v_y^2 \rangle = \langle v_z^2 \rangle$

and

$$\langle v^2 \rangle = 3 \langle v_z^2 \rangle = 3 (\sum n_z v_z^2) / n \quad \text{Equation 61}$$

Then from  $P = m \sum n_z v_z^2$ , the basic equation for the pressure is obtained as

$$P = \frac{1}{3} nm \langle v^2 \rangle. \quad \text{Equation 62}$$

Since

$$mn = \rho \quad \text{Equation 63}$$

which indicates that, at constant temperature, their pressure is altered in correspondence with the density, or inversely with the volume. This is known as *Boyle's law*.

It is known that if two different gases, originally at the same temperature, are mixed, no change in temperature will occur. This result is proved to be true independent of the control of volumes. As a result, the average kinetic energy of molecules must be the same for all gases at any given temperature, and similarly, the rate of increase with temperature must be identical for all gases. The temperature could be defined in terms of the average kinetic energy per molecule, which is shown as the following relation

$$(m \sum n_x v_x^2 / 2n) = (m \sum n_y v_y^2 / 2n) = (m \sum n_z v_z^2 / 2n) = \frac{1}{6} m \langle v^2 \rangle = \frac{1}{2} kT \quad \text{Equation 64}$$

For each of the three degrees of freedom of translational motion, where  $T$  is the absolute temperature, and  $k$  is a universal constant, or the Boltzmann's constant. The total mean translational energy is then

$$\frac{1}{2} m \langle v^2 \rangle = \frac{1}{2} m v_r^2 = \frac{3}{2} kT \quad \text{Equation 65}$$

where  $v_r$  is identified as the root-mean-square velocity. The total kinetic energy of molecules in a volume  $V$  will be

$$\frac{1}{2} mn \langle v^2 \rangle V = \frac{3}{2} PV \quad \text{Equation 66}$$

Following Boyles's law, it could be expressed in the form

$$P = nkT \quad \text{Equation 67}$$

which is known as the Charles' law.

In order to evaluate the behavior of gas in phase reactions, gaseous beams, heat flows, and the surface bombardment, it is imperative to develop a model of gas

molecules. The kinetic theory of gases views gaseous molecules as hard spheres. The probability distribution of velocities is based on the application of the Maxwell speed distribution. For a simple monotonic gas, the probability of a molecule possessing a certain speed is given by

$$P(v) = 4\pi \left[ \frac{m}{2\pi kT} \right]^{3/2} v^2 e^{-mv^2/2kT} \quad \text{Equation 68}$$

where  $m$  is the mass of the molecule,  $k$  is Boltzmann's constant,  $v$  is the magnitude of the velocity, and  $T$  is the temperature in Kelvin. The speed, or the average magnitude of the velocity, is given by

$$|\bar{v}| \equiv \bar{c} = \int_0^\infty v P(v) dv = \sqrt{\frac{8kT}{\pi m}} \quad \text{Equation 69}$$

The standard component of the velocity in any direction is given by

$$\bar{v}_x = \bar{v}_y = \bar{v}_z = \sqrt{\frac{2kT}{\pi m}} \quad \text{Equation 70}$$

and the root mean square velocity is given by

$$v_{rms} = \sqrt{\frac{3kT}{m}} \quad \text{Equation 71}$$

Since the direction of the thermal velocity is random, if there are no applied forces on the outside, the average velocity is zero. If a small pressure gradient is forced upon the gas, a net macroscopic flow will emerge, from high to low pressure. On the microscopic level, this excited flow velocity vector is imparted upon the much larger thermal velocity. Although individual atoms may be moving against the pressure gradient at any second, normally the flow will travel from high to low pressure.

Gas phase collision is one of the crucial mechanisms specified for gases changing velocity at atmospheric pressure. It is hypothesized that a molecule of diameter  $d$  is

moving arbitrarily in the gas. If another molecule of the same type is within a distance  $d$  of the estimated path of the first atom, a collision takes place. Then, the molecule has a collision cross section of  $\pi d^2$ , which, by the simple hard sphere approximation, is four times the definite cross section of a single molecule. The probability that a collision will be initiated over a distance  $L$  is given by

$$P = L\pi d^2 n \quad \text{Equation 72}$$

where  $n$  is the number of gas molecules per unit volume. Setting  $P \approx 1$ , the average distance between collisions can be estimated as

$$\lambda \approx \frac{1}{\pi d^2 n} \quad \text{Equation 73}$$

These collisions are usually called the mean free path  $\lambda$ .

A more accurate rigor statistical treatment gives [43]:

$$\lambda \approx \frac{1}{\sqrt{2}\pi d^2 n} \quad \text{Equation 74}$$

Since  $n$  is not uniformly defined, it must be calculated from a macroscopic equation of state. Thus, the optimal gas law is frequently used

$$n = \frac{N}{V} = \frac{P}{kT} \quad \text{Equation 75}$$

where  $P$  is the pressure of the chamber. Combining equations,

$$\lambda = \frac{kT}{\sqrt{2}\pi d^2 P} \quad \text{Equation 76}$$

## 1.6 Gas Flow and Conductance

The equations are used to calculate pumping speeds and gas flows. In measuring the flow of a simple liquid, such as water, a common unit might be the volumetric flow rate, or gallons per hour. Although volumetric flow rate is usually used in recounting gas flows, especially in delineating pumping speeds, due to the fact that gases are much more compressible than liquids, the use of the gas flow in this approach incurs problems. In order to avoid this problem, the throughput is used to express the amount of gas flowing through a system. The mass of a gas in some volume  $V$  is

$$G = \rho V \quad \text{Equation 77}$$

where  $\rho$  is the mass density ( $m \times n$ ). Then the mass flow rate is

$$q_m = \frac{dG}{dt} \quad \text{Equation 78}$$

The throughput of a gas  $Q$ , which has units of pressure-volume/time, is given by

$$Q = q_m \frac{P}{\rho} \quad \text{Equation 79}$$

Generally, gas flows are measured in terms of a standard volume, which refers to the condition that the volume of an equivalent amount of gas would occupy at 0°C and 1 atm of pressure. While one mole of gas occupies 22.4 L at standard conditions, one standard liter is 1/22.4 moles. Pumps are usually defined in terms of pumping speed,  $S_p$ ,

$$S_p = \frac{Q}{P_p} = \frac{dV_p}{dt} \quad \text{Equation 80}$$

where  $P_p$  is the inlet pump pressure. For instance, a pump rated for 1000 l/ min (slm), will pump 1000 slm at 1 atm inlet pressure. If the inlet pressure is 0.1 atm and the

pumping speed at this pressure stays at 1000 l/min, it can be concluded the maximum gas flow that this same pump could allow is 100 slm. Furthermore, the pumping speed normally is not a constant. Instead, it is closely related to the gas being pumped and the inlet pressure.

## **Chapter 2 Growth of III-V Semiconductor Nanowires (GaAs)**

Studies of one-dimensional (1D) nanoscale materials have attracted substantial research interest during the past decade concerning their specific physical properties and potential applications. III-V group semiconductors are of particular interest for their electronic and optoelectronic properties. Generally, efforts have focused on the synthesis and the characterization of III-V semiconductor colloids and nanocrystals [44], while fabrication techniques have encompassed the evaporation, the laser-assisted catalytic growth (VLS, at above 680° C) [45,46], and the oxide-assisted fabrication (~750° C) [47].

### **2.1 Introduction**

A series of experiments were designed to investigate the growth of gallium arsenide nanowires. In the course of the experiment, however, it was found that the nanowires formed were deficient in arsenic. Furthermore, oxygen was readily incorporated into the nanowires. A set of experiments was then investigated for the growth of gallium oxide nanowires from the GaAs source material. It is well known that the deposition of gold onto III-V substrates can catalyze a series of chemical reaction at higher temperatures. Since the Pauling electronegativity of Au is higher than that of the elements of Group V, Au can act as an oxidizing agent to displace the less electronegative elements of Group V by combining the highly electropositive Group III metals. In these experiments, GaAs pieces were first rinsed with acetone and methanol. Then gold was deposited either on the substrate at room temperature via sputter deposition, followed by an annealing step, or onto the substrate at a high temperature of



deposition via laser ablation. Various temperatures were investigated with results shown as follows.

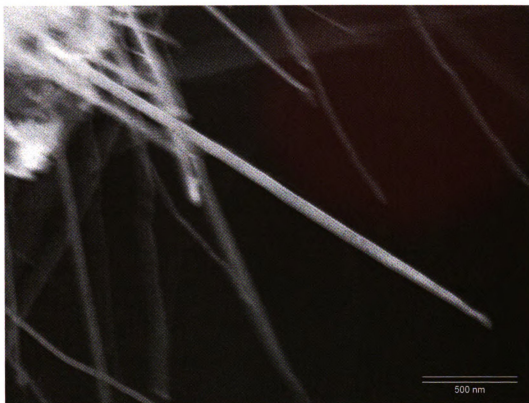
## **2.2 Experiments**

### **Experiment #1:**

A gold layer was sputter deposited at room temperature to a thickness of 20 nm, and the sample was subsequently annealed to 970° C. The GaAs target was placed approximately 4 cm from the substrate and ablated by pulsed laser deposition (PLD) for 1 minute and 30 seconds. The pulse was 10 Hz at 500 mJ.

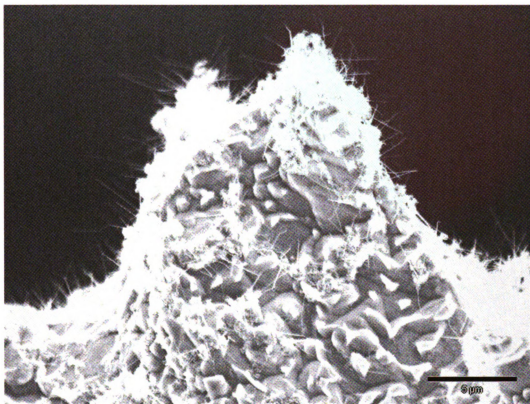
The experiment was conducted within a quartz tube (outer diameter, 90 mm; length, 80 cm) heated by a horizontal tube furnace. The sample was positioned at the center of the quartz boat, which was placed at the center of a quartz tube which was evacuated to about 30 mTorr. A background gas of argon was introduced into the chamber at a flow rate of 200 standard cubic centimeters per minute (sccm), which was maintained throughout the whole reaction period.

All the samples were examined and photographed using the JEOL Scanning Electron Microscope (SEM) and EDS (Energy Dispersive X-Ray Spectroscopy) was concurrently carried out to determine the elements present in the sample.

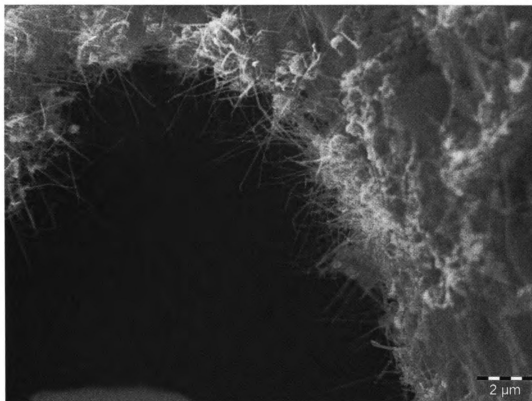


**Figure 19.** Nanowires grown from a piece of GaAs. The scale bar is 500 nm.

In the SEM image of Figure 19, the upper left white area is the GaAs chunk. This GaAs sample was placed in front of a separate gallium arsenide target which was ablated by a KrF excimer laser for 1 minute and 30 seconds, at 10 Hz and 500 mJ. The nanowires shown in the SEM image have diameters ranging from 30-90 nm and their lengths are a few microns. Most of the nanowires appear to be straight forming to a sharp tip. A characteristic of the vapor-liquid-solid growth mechanism is the formation of an alloy ball at the tip of the nanowires. The absence of this characteristic ball suggests that either a different growth mechanism is taking place such as the oxide assisted growth, or the gold ball is being incorporated into the nanowire during system cool down.

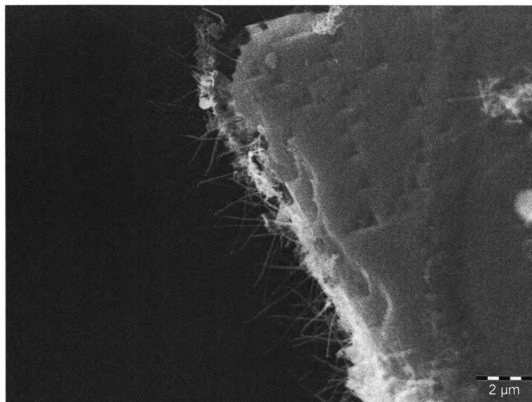


**Figure 20.** The nanowires grew from the GaAs chunk. The scale bar is 5 $\mu$ m.



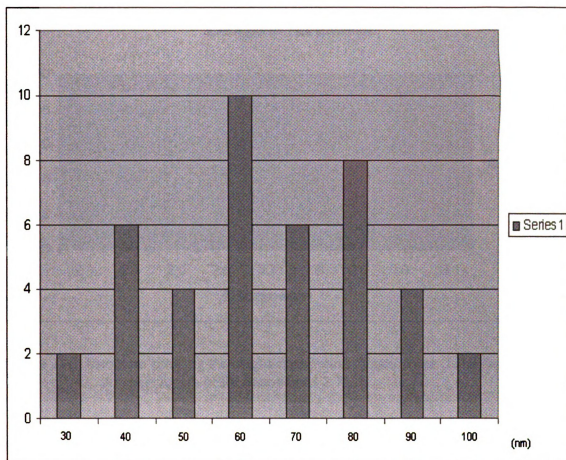
**Figure 21.** These nanowires were a few microns in length. The scale bar is 2  $\mu\text{m}$ .

Figure 21 is the SEM image of gallium oxide nanowires grew from the gallium arsenide chunk. These nanowires were a few microns in length and were primarily found on the edge of the sample. The upper and right white areas are the gallium arsenide chunk. These nanowires were 2-3 microns in length.

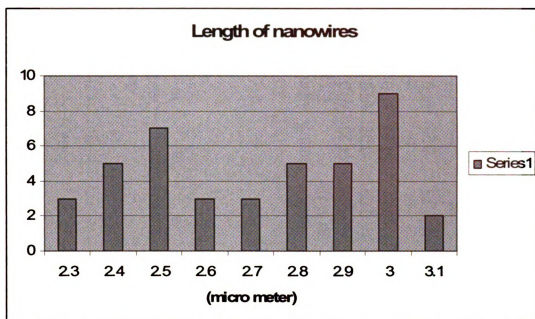


**Figure 22.** The nanowires grew from the edge. The scale bar is 2μm.

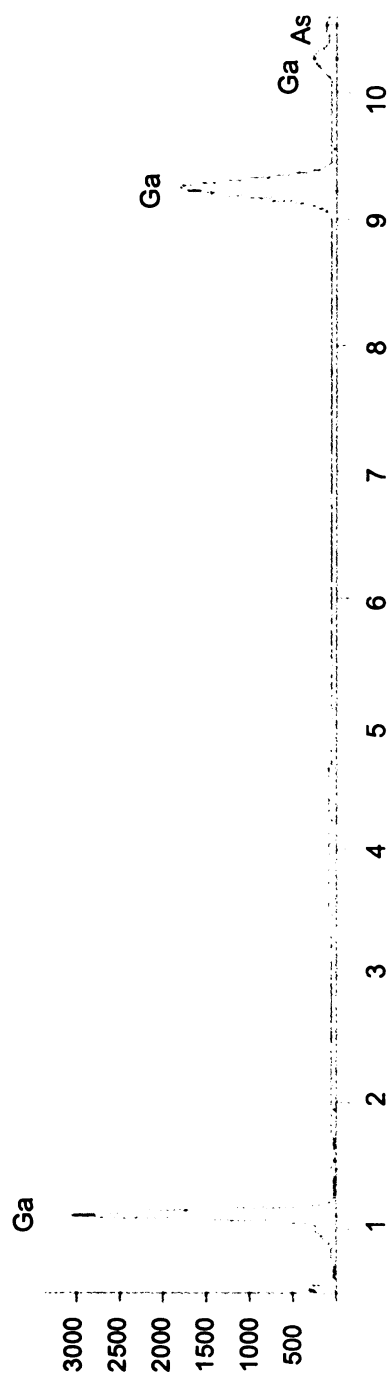
In Figure 22, the SEM image shows gallium oxide nanowires grew from the GaAs chunk. These nanowires were a few microns in length and their growth mainly took place along the edges. The SEM image also shows the presence of some triangular shape structures scattered throughout the image.



**Figure 23.** Histogram showing the diameter of nanowires. Total sample size: 42.  
Average Diameter: 65 nm



**Figure 24.** Histogram showing the height distribution of nanowires. Total sample size : 42. Average length of the nanowire is 2.7  $\mu\text{m}$ .



Quantitative Results ga(1)

Element Line	K-Ratio	Z	A	F	ZAF	Weight % Error	Weight % Error	Norm. Wt.% Err	Atom %	Atom % Error
OK	0.046	0.795	5.018	0.998	3.985	15.36	+/- 0.28	+/- 0.28	44.23	+/- 0.82
Al K	0.000	0.887	6.408	1.000	5.684	0.23	+/- 0.06	+/- 0.06	0.39	+/- 0.11
Ga K	0.868	1.053	0.998	0.984	1.034	75.88	+/- 0.87	+/- 0.87	50.14	+/- 0.58
Ga L	0.000	0.000	0.000	0.000	0.000	--	--	--	--	--
As K	0.086	1.074	1.093	1.000	1.174	8.53	+/- 0.75	+/- 0.75	5.25	+/- 0.46
As L	0.000	0.000	0.000	0.000	0.000	--	--	--	--	--
Total						100.00			100.00	

**Figure 25.** The EDS analysis of nanowire

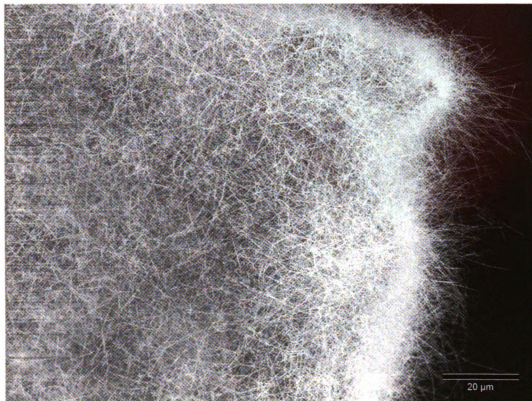


Figure 25 shows the EDS analysis taken on the nanowires shown in Figure 21. The EDS analysis shows the components of nanowires were gallium and oxygen. The histograms in Figure 23 and Figure 24 show the diameter and length distributions of the nanowires. The average dimensions of the grown nanowires were about 65 nm in diameter and 2.7  $\mu\text{m}$  in length. These nanowires were not distributed evenly and consistently on the surface, but tended to grow in clustered areas.

A similar experiment was conducted with the same temperature and pressure conditions. The only difference was the substrate was placed behind the GaAs target. The results were similar to those reported above showing that the location of the GaAs target did not affect the nanowires growth.

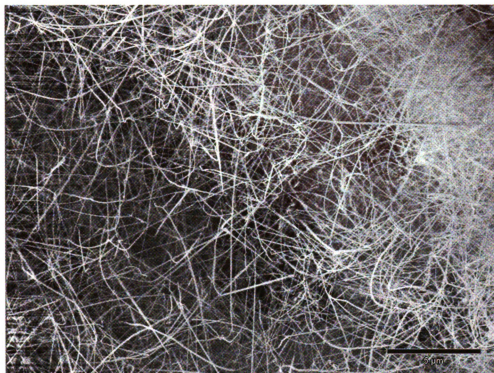
#### Experiment #2:

Experiment #1 described the first evidence of gallium oxide nanowires growth on the GaAs substrate. In Experiment #2, nanowires dependence on annealing time is reported. A gold layer was sputter deposited at room temperature to a thickness of 20 nm, and the sample was subsequently annealed at 970° C for 40 minutes. Two samples of different sizes were placed inside the chamber.

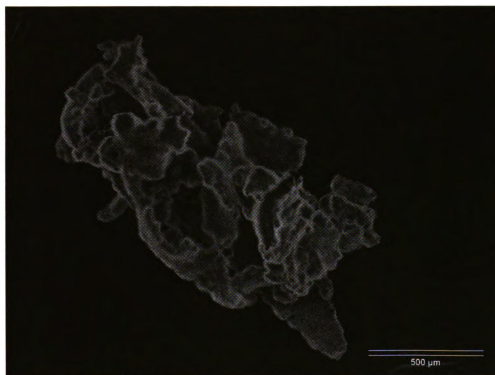


**Figure 26.** Under these fabrication conditions, a very high density of nanowires formed. The scale bar is 20  $\mu\text{m}$ .

The SEM images in Figure 26 and Figure 27 show nanowires of several microns in length with an average diameter of approximately 80 nm. The size of this GaAs substrate was approximately 0.2 mm by 0.2 mm. The diameters of these nanowires were more uniform than for the shorter growth times of the previous section.

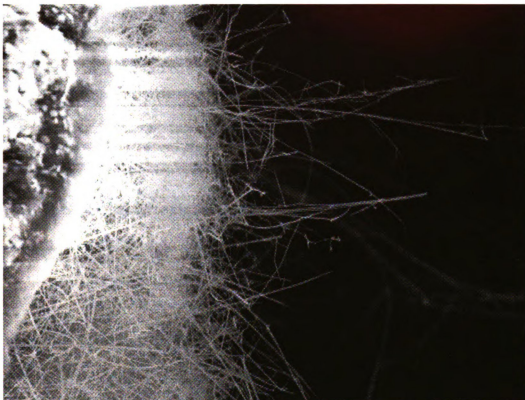


**Figure 27.** The diameters of these nanowires were uniform. The scale bar is 5  $\mu\text{m}$ .

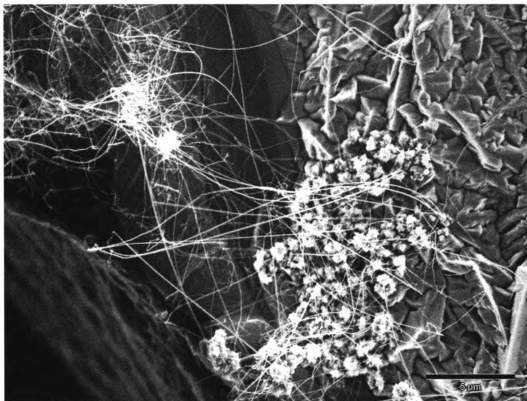


**Figure 28.** This zoom-out image illustrates that nanowires connected with each other in order to form a wool-like structure. Nonetheless, there was no gallium arsenide chunk left inside this structure.

The SEM images in Figure 29 and 30 were taken from a larger substrate of gallium arsenide (approximately 0.8 mm by 0.8 mm). The nanowires formed a thick layer on top of the piece of GaAs. From the SEM image in Figure 29, the GaAs chunk could be observed to be placed on the left side while a thick layer of nanowires were on the top. These nanowires were a few microns in length.



**Figure 29.** The nanowires formed a thick layer on top of the GaAs chunk.

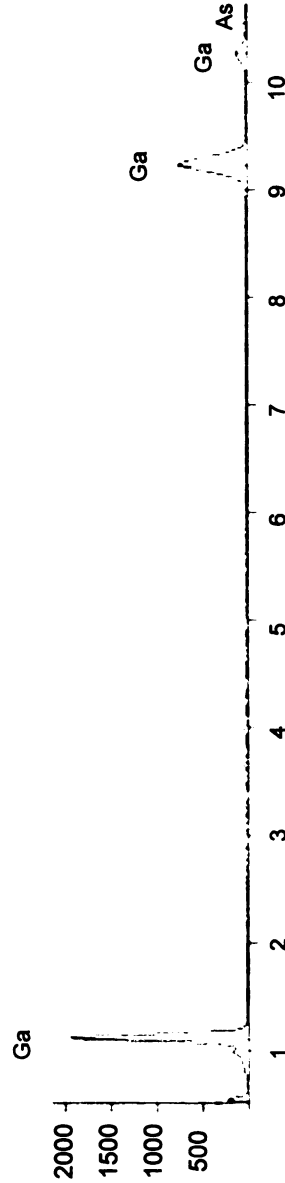


**Figure 30.** The SEM image shows nanowires. In addition, the same image illustrates that the gallium arsenide surface was underneath the layer of nanowires and there were some nanowires left on the surface. The length of nanowires was tens of microns. The scale bar is 5  $\mu\text{m}$ .

The EDS analysis in Figure 31 shows the nanowires consisted primarily of gallium and oxygen.

The histogram in Figure 32 shows the diameter distribution of the grown gallium oxide wires. The average dimension of the grown nanowires was about 81 nm in diameter.

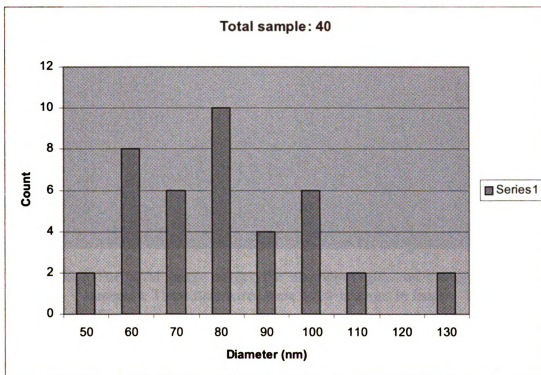
Element Line	K-Ratio	Z	A	F	ZAF	Weight % Error	Weight % Error	Norm. Wt % Err	Atom % Error	Atom % Error
C K	0.002	0.777	9.110	1.000	7.074	1.24	+/- 0.95	+/- 0.95	3.86	+/- 2.97
O K	0.082	0.819	4.740	0.999	3.878	24.04	+/- 0.50	+/- 0.50	56.21	+/- 1.18
Ga K	0.865	1.089	0.995	0.991	1.073	70.12	+/- 1.26	+/- 1.26	37.63	+/- 0.68
Ga L	0.000	0.000	0.000	0.000	0.000	--	--	--	--	--
As K	0.050	1.111	1.089	1.000	1.210	4.60	+/- 0.54	+/- 0.54	2.30	+/- 0.27
As L	0.000	0.000	0.000	0.000	0.000	--	--	--	--	--
Total						100.00			100.00	



**Figure 31.** EDS analysis on the grown gallium oxide nanowires.

The density of nanowires was found to be significantly higher in Experiment #2 compared to the results of Experiment #1. These nanowires were distributed evenly and consistently on the surface of the piece of GaAs.

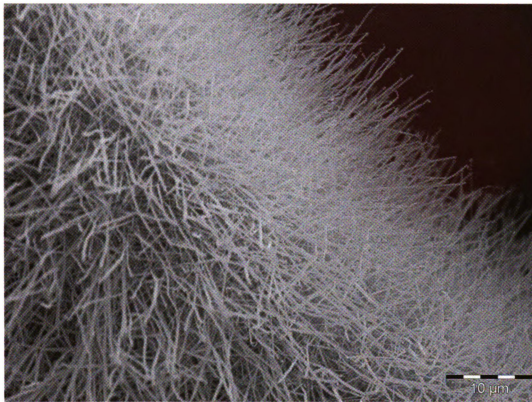
In Experiment #1, the sample stayed in 970° C for 90 seconds while the laser ablated the GaAs target. The results showed these nanowires were not distributed evenly on the surface. In Experiment #2, the GaAs was annealed at 970° C for 40 minutes, and showed a significant increase in the density and distribution of nanowires.



**Figure 32.** Histogram showing the diameter distribution of the nanowires. The average diameter is 81 nm.

### Experiment #3:

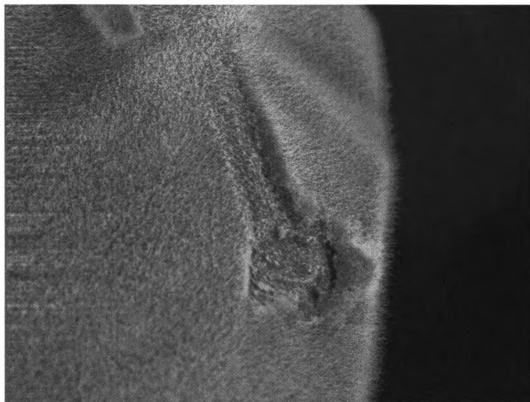
To study the affect of the annealing temperature, the same experimental conditions were used except the annealing temperature. A gold layer was sputter deposited at room temperature to a thickness of 20 nm, and the sample was subsequently annealed at 800° C for 40 minutes.



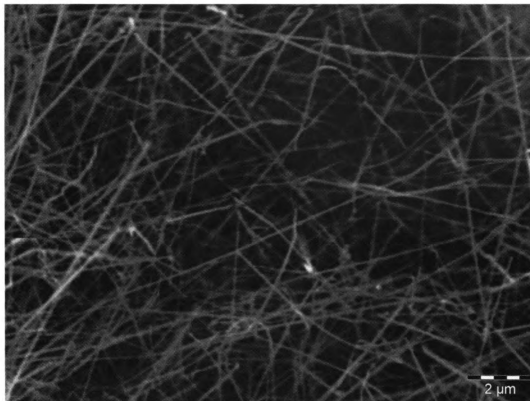
**Figure 33.** The SEM image shows the nanowires grew on the piece of gallium arsenide. These nanowires were a few microns in length. The scale bar is 10  $\mu\text{m}$ .

Figure 34 shows a broader view indicating the uniform coverage of the substrate by nanowires. The shape in the middle of the image was formed after picking up the sample with tweezers. It clearly indicates that the piece of gallium arsenide was covered with a thick layer of nanowires with uniform length. Nonetheless, not all of the germanium arsenic turned into nanowires.



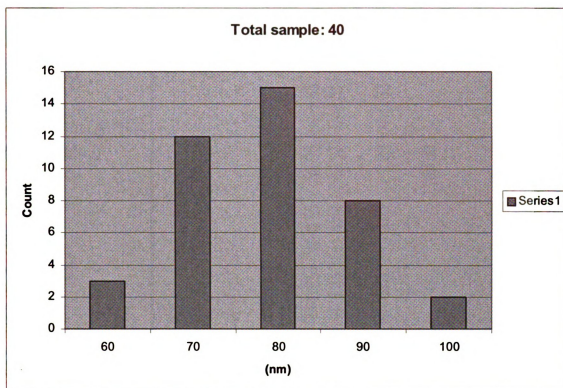


**Figure 34.** The SEM image shows the nanowires grew on top of gallium arsenide chunk.



**Figure 35.** The SEM image show the nanowires grew on top of gallium arsenide chunk. The scale bar is 2  $\mu\text{m}$ .

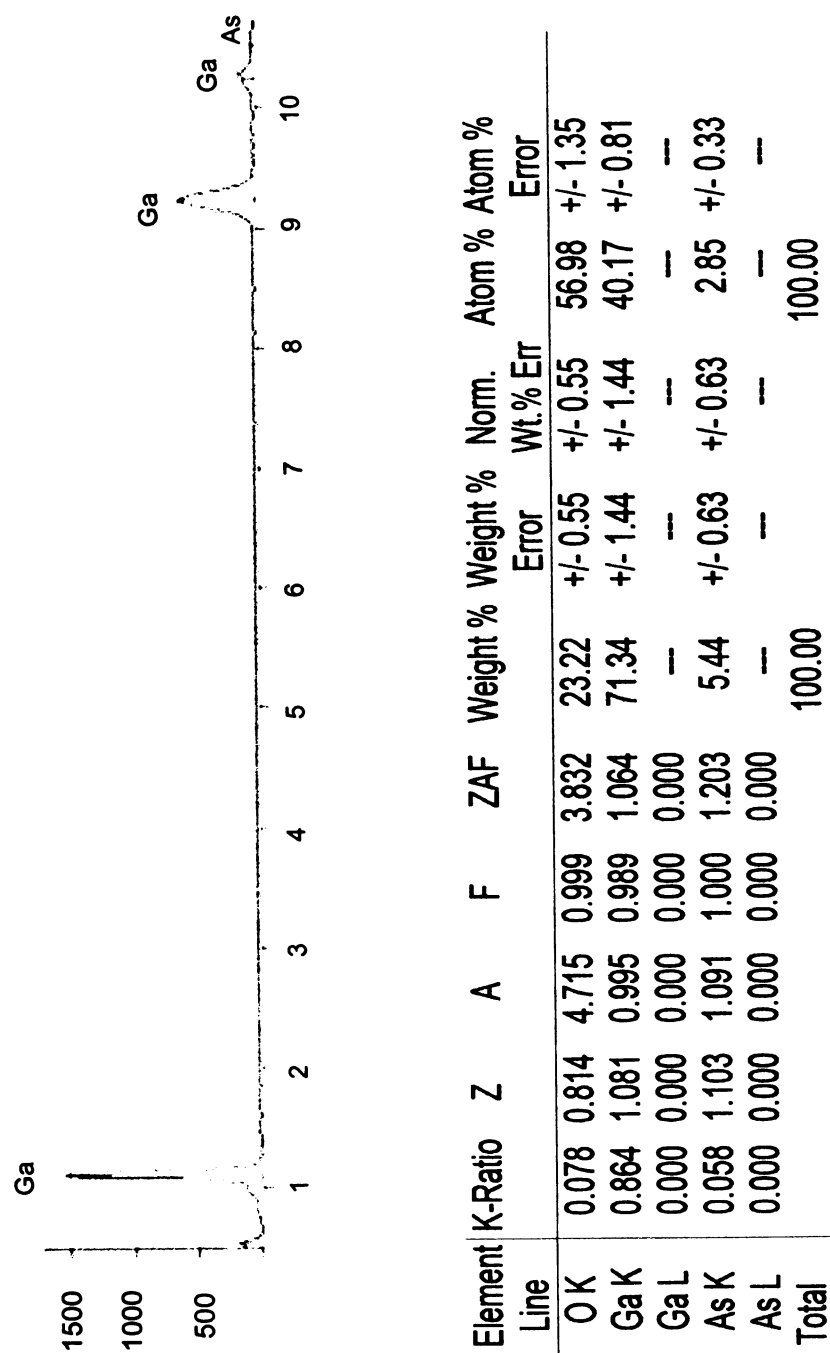
The diameter of nanowires was quite uniform as indicated in the histogram shown in Figure 18. The average dimension of the grown nanowires was about 78.5 nm in diameter.



**Figure 36.** Histogram showing the diameter of nanowires. Total sample size: 40.

Comparing Experiment #3 with Experiment #2, we do not find significant differences in the results; however below 700° C annealing, no growth was observed.

The EDS analysis in Figure 37 shows gallium and oxygen as the predominant components of the nanowires. Arsenic also appeared in the analysis; however, its amount was extremely small compared with that of gallium and oxygen.



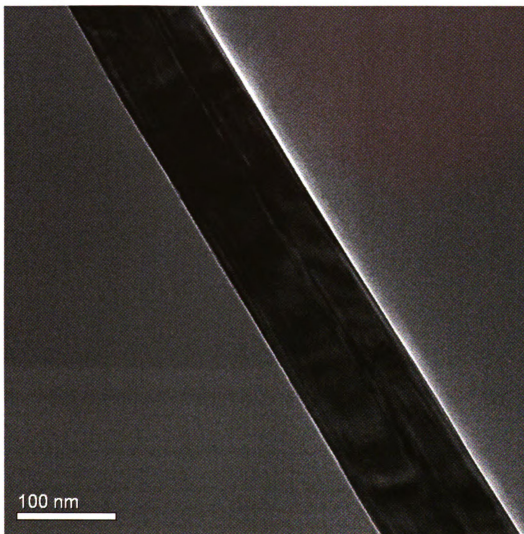
**Figure 37.** EDS analysis on the grown gallium oxide nanowires



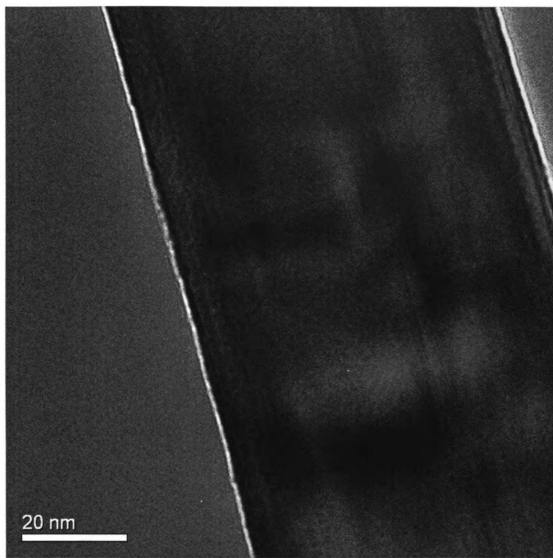
**Figure 38.** The SEM image of a piece of GaAs. No gold was deposited on this sample before growth.

Figure 38 is a SEM image of GaAs which did not have a layer of gold deposited on it. This piece of GaAs was placed next to a separate sample that did have a layer of deposited gold. There were still some nanowires on the surface; however, the density of nanowires is significantly smaller, and the nanowire clusters are loosely bound to the surface of the substrate.

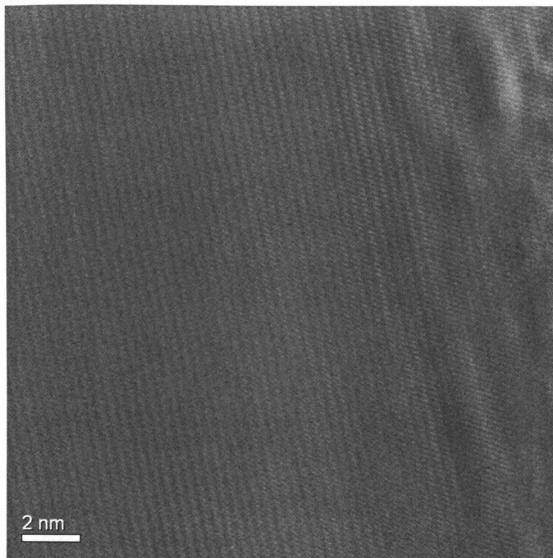
### TEM image analysis



**Figure 39.** TEM image shows nanowire grown from GaAs

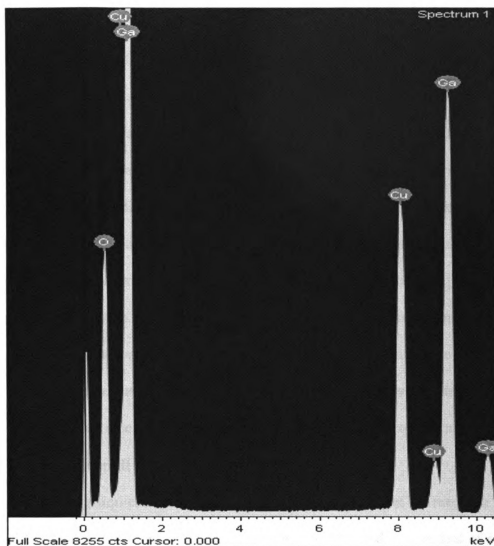


**Figure 40.** TEM image shows nanowire grown from GaAs



**Figure 41.** TEM image shows nanowire grown from GaAs





Element	Weight%	Atomic%
O K	31.07	65.46
Cu K	26.00	13.79
Ga K	42.93	20.75
Totals	100.00	

**Figure 42.** EDS analysis of nanowires

The TEM images show a nanowire diameter of approximately 70 nm. The atomic planes shown in Figure 41 have a spacing of approximately 3.46 Å. In Figure 42, the EDS analysis shows gallium and oxygen in a ratio of approximately 1:3 respectively.

## 2.3 Discussion

Current studies of Au/III-V interfaces have pointed out that the “interdiffusion” between the metal and semiconductor occurred after samples were heated to relatively low temperatures, such as 573 K and other degrees of same effect. Meanwhile, the fact that this diffusion is essentially the result of a chemical reaction has been identified. The general pattern derived from these studies is that heating a Au film/III-V substrate system will lead to the decomposition of the semiconductor near the interface and the release of the volatile elemental Group V via the grain boundaries of the metal film [48]. The study of the Au-Ga-As system indicated that the bulk Au and GaAs are not thermodynamically stable with respect to one another [49] since Pauling electronegativity of Au is higher than that of the element of Group V. Thus, Au could act as an oxidizing agent and displace the less electronegative Group V elements by combining the highly electropositive Group III metals.

The investigation concerning chemical reactions occurring at the interface between a metal film and a III-V compound semiconductor has attracted a great deal of attention. Nonetheless, the measure of the reaction spontaneity is the change in the Gibbs free energy of the system, ( $\Delta G_R$ ), which takes into account the entropy change of the reaction ( $\Delta S_R$ ) of a system as well as  $\Delta H_R$ . In our discussion, since the assumption was that metal/semiconductor reactions only involve solid-phase products, the contribution of the entropy was considered insignificant. The phenomenon of group V elements escaping from III-V compound semiconductors in gas-phase has been observed during reactions of thin metal films with substrates [50]. Hence, the entropy change is required for the gas-phase elements formation. This change is positive, especially for a vaporization process.

The system with a positive entropy reaction will ultimately become thermodynamically spontaneous at particularly high temperatures; therefore, either the entropy or the reaction is considered to be an important factor. The determination of  $\Delta G_R$  as a function of temperature refers to the temperatures at which a reaction may occur spontaneously.

Expanding on the thermodynamic principles proposed by Gibbs in 1875, Gibbs' phase rule identifies the possible number of degrees of freedom in a system at equilibrium, in terms of the number of separate phases and the number of chemical constituents in a system.

$$F=C-P+2 \quad \text{Equation 81}$$

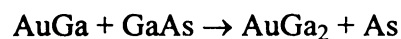
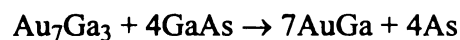
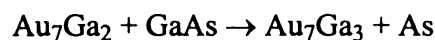
where  $F$  is the number of degrees of freedom,  $C$  the number of chemical constituents, and  $P$  is the number of phases. In the case of the system of Au-III-V with three components, the maximum number of phases that may coexist is  $P=3$ . With the Au film deposited onto the III-V substrate, the quantity of the II-V material is larger than that of the Au thin film in this system. The reaction:



The Au thin film reacts with the III-V substrate in order to form the intermetallic compound Au-III and elemental (element) V. In particular, the system will not reach the equilibrium until all of the Au is consumed. This system is an open system, which indicates that, during a heating cycle, the vapor pressure of the Group V elements becomes appreciable. There are four phases present at equilibrium (III-V), Au-III, and the elements of Group V in solid and gas-phases. As the gaseous species are

continuously being pumped out, the vaporization process will continue until all the solid elemental group has escaped into the gas phase.

The reactions that have been observed between deposited Au films and GaAs substrates were mainly driven by the loss of the gas-phase As in an open system during the experiment. After losing a certain amount of As, the composition of solid phases that were initially on the Au-GaAs pseudobinary shifted to the Ga-rich side, where the equilibrium phases are Au and GaAs phases. With the loss of As in an open system, all the Au may be consumed. Thus, a series of reactions liberating gas-phase As species become feasible accordingly, in which the succeeding reaction occurs once the gold containing reactants had been consumed:



Based on the thermodynamic equations mentioned in the previous section, an equation can be deduced as follows:

$$\Delta G_R = \Delta H_R - T\Delta S_R \quad \text{Equation 83}$$

A reaction will occur spontaneously when  $\Delta G_R < 0$ . If both  $\Delta H_R$  and  $\Delta S_R$  are positive,  $\Delta G_R$  will be positive when T is small.

$$T\Delta S_R = \Delta H_R - \Delta G_R$$

$$T = (\Delta H_R - \Delta G_R) / \Delta S_R \quad \text{Equation 84}$$

We can find the point  $\Delta G_R = 0$  when the temperature is  $\Delta H_R / \Delta S_R$ . This is the point when the reaction will first become thermodynamically feasible.

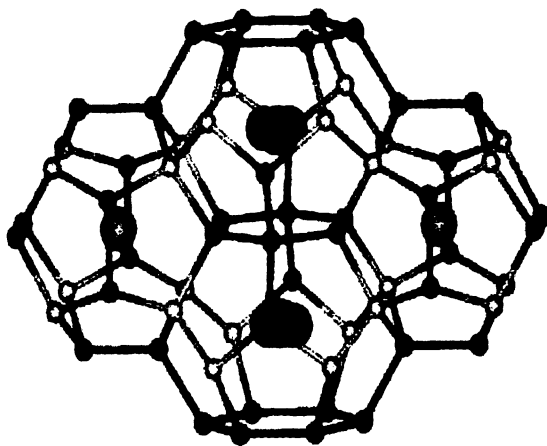
## 2.4 Conclusion

In this chapter, various growth conditions have been employed to grow nanowires from GaAs in the furnace system. Nanowires with different densities were found in different growing conditions. From the SEM image in Figure 38, the significant growth of nanowires only occurred when an additional gold was deposited on the gallium arsenide chunk. The EDS analysis shows that nanowires were gallium oxide nanowires with the gallium to oxygen ratio ranging from 1:1 to 1:3. To our knowledge, this is the first observation of gallium oxide nanowires being synthesized through the simple physical evaporation of the gold deposited on a GaAs chunk. In all cases, a gold ball was found absent at the tips of the nanowires, however, when no gold was deposited on the GaAs, no nanowires grew.

## Chapter 3 Growing Nanowires from $\text{Sr}_8\text{Ga}_{16}\text{Ge}_{30}$

### 3.1 Introduction

Through independent research in the laboratory, an opportunity to investigate a new material consisting of  $\text{Sr}_8\text{Ga}_{16}\text{Ge}_{30}$  was capitalized on. This material is a type-I clathrate and displays glass-like thermal conductivities along with good charge carrier mobility, which makes it an interesting material for thermoelectrics research. We produced nanowires from  $\text{Sr}_8\text{Ga}_{16}\text{Ge}_{30}$  simply by mixing it with Au nanoparticles and annealing. To our knowledge, this material has not previously been grown in the form of nanowires. Hence, the successful growth of clathrate nanowires would establish the foundation for further studies of this thermoelectric material. Unfortunately, EDS analysis during the TEM imaging shows the nanowires primarily consist of gallium, with no trace of Sr and Ge detected.



**Figure 43.** The  $\text{Sr}_8\text{Ga}_{16}\text{Ge}_{30}$  structure. In the framework, the black atoms occupy the  $6c$  sites, the light gray atoms occupy the  $16i$  sites, and the dark gray atoms occupy the  $24k$  sites. In the cavities, the gray atoms are at the Sr(1)  $2a$  sites and the black atoms are at the Sr(2)  $24k$  sites [51].

## 3.2 Experiments

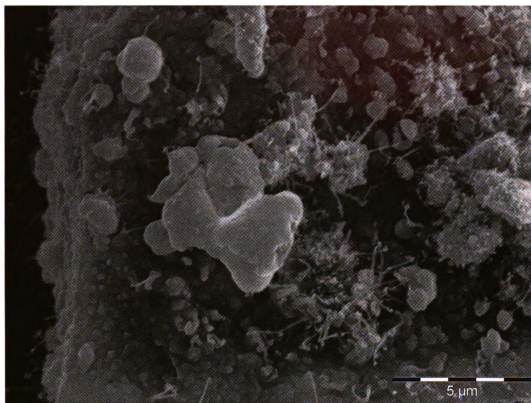
### Experiment #1:

$\text{Sr}_8\text{Ga}_{16}\text{Ge}_{30}$  powder was mixed with gold nanoparticles and annealed at  $810^\circ\text{C}$  for 120 minutes. The  $\text{Sr}_8\text{Ga}_{16}\text{Ge}_{30}$  pile was mixed with colloidal Au of 20nm nominal size and with polylysine-L to avoid colloidal clustering. The sample was placed on top of a quartz plate, and subsequently annealed to  $810^\circ\text{C}$  for 120 minutes. The experiment was conducted within a quartz tube (outer diameter, 90 mm; length, 80 cm) heated by a horizontal tube furnace. The sample was put on a quartz boat and placed at the center of the quartz tube that was evacuated to about 30 mTorr. A background gas of argon was used at a flow rate of 200 sccm and this flow was maintained throughout the whole reaction. The pressure inside the tube increased from 30 mTorr to 150 mTorr after the argon gas entered into the tube.

The SEM image in Figure 44 shows that the nanowires were scattered on the surface of the  $\text{Sr}_8\text{Ga}_{16}\text{Ge}_{30}$  powder. The dark area on the left side is the quartz plate. Nanowires with a diameter of 50 nm grew on the  $\text{Sr}_8\text{Ga}_{16}\text{Ge}_{30}$  powder surface and mixed with some whiskers of bigger size. The nanowires were found to grow in select regions and were not notably straight. Some nanowires were observed on the quartz plate close to the  $\text{Sr}_8\text{Ga}_{16}\text{Ge}_{30}$  powder.

In the SEM image in Figure 45, the dark region is the quartz plate. The bright area in the bottom left of the image is the  $\text{Sr}_8\text{Ga}_{16}\text{Ge}_{30}$  powder. We found that most of nanowires distributed on the bottom half of the image were close to the  $\text{Sr}_8\text{Ga}_{16}\text{Ge}_{30}$  powder region. Nanowires close to the  $\text{Sr}_8\text{Ga}_{16}\text{Ge}_{30}$  powder particles were found in higher densities with lengths of approximately 5  $\mu\text{m}$  and average diameters of 30 nm,

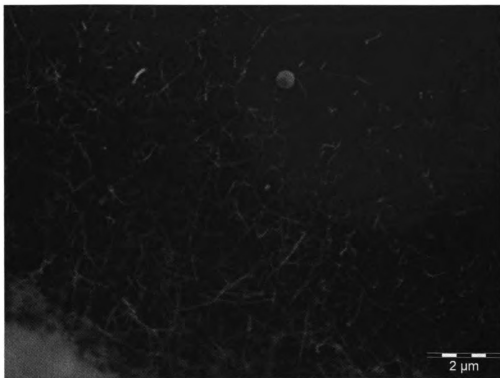
farther away from the powder particles, the density and length of the nanowires gradually decrease to negligible quantities at distances of 11  $\mu\text{m}$  from the powder particles.



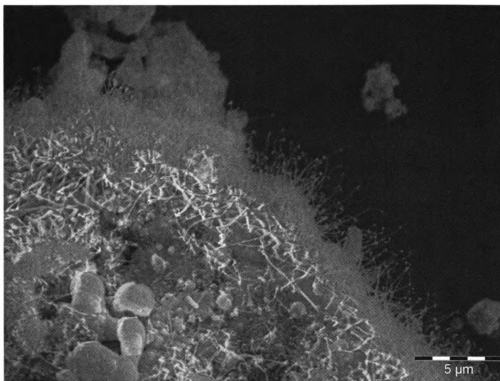
**Figure 44.** The SEM image shows that nanowires were scattered on the surface of  $\text{Sr}_8\text{Ga}_{16}\text{Ge}_{30}$  powders. The scale bar is 5  $\mu\text{m}$ .

The SEM image in Figure 46 shows that nanowires were mostly scattered on the top surface of the  $\text{Sr}_8\text{Ga}_{16}\text{Ge}_{30}$  powder. A mixture of larger diameter and smaller diameter nanowires can be seen by comparing the center of the image, to the nanowires at the perimeter of the powder particle. The dark area on the right side is the quartz plate. The average length of nanowires was 4  $\mu\text{m}$  and the average diameter was 70 nm. The scale bar is 5  $\mu\text{m}$ .

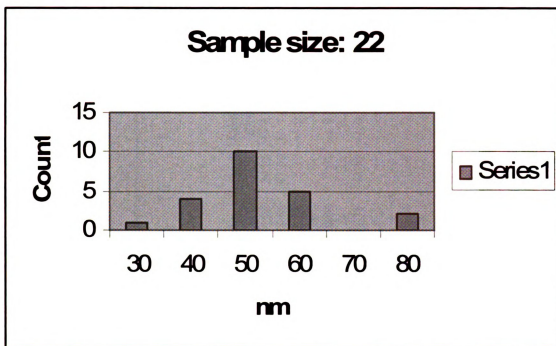




**Figure 45.** The SEM image shows that the dark region is a quartz plate. The scale bar is 2 μm.

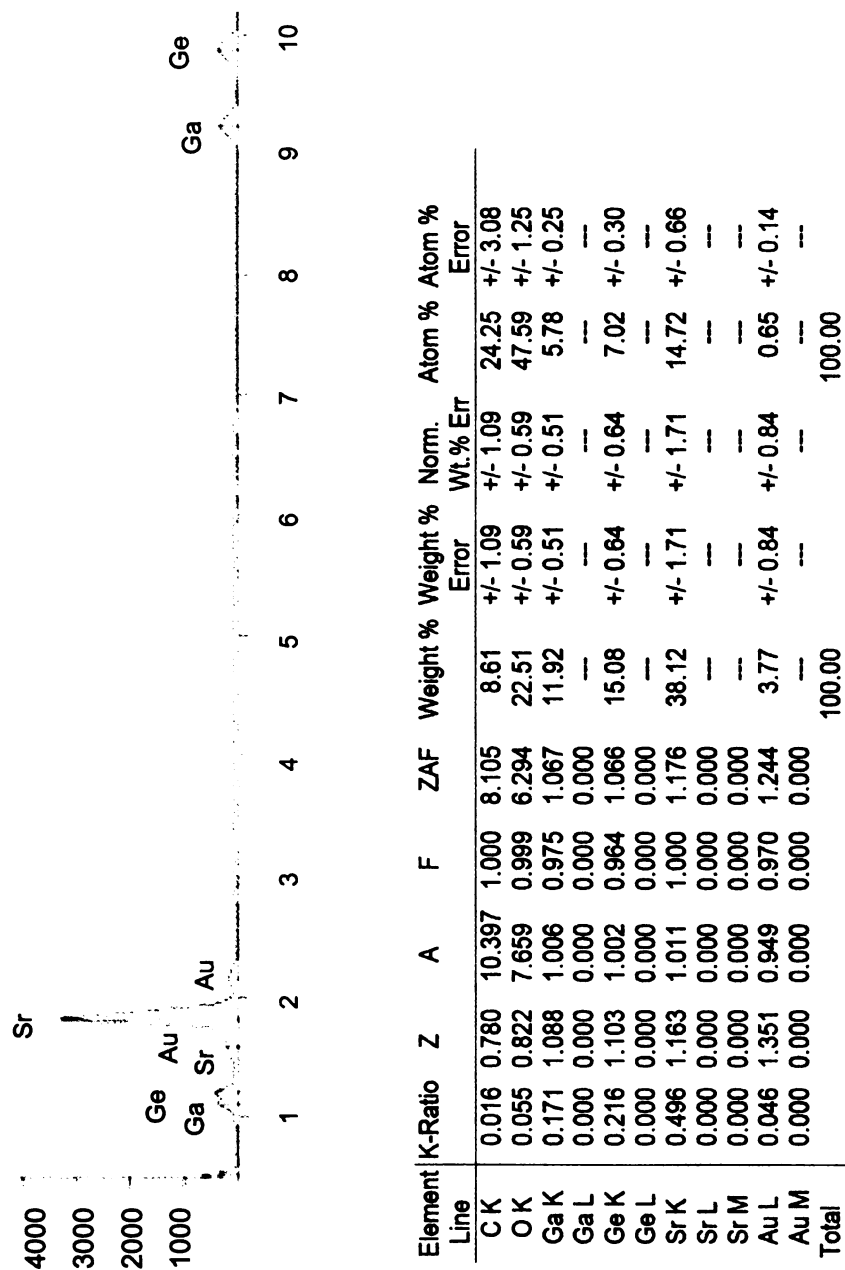


**Figure 46.** The SEM image shows that nanowires were mostly scattered on the top surface of the  $\text{Sr}_8\text{Ga}_{16}\text{Ge}_{30}$  powder. The scale bar is 5 μm.



**Figure 47.** Histogram showing the diameter of nanowires. Total sample size: 22.  
Average diameter is 52 nm.

The histogram in Figure 47 shows the diameter distributions of the nanowires. The average dimension was about 52 nm in diameter.



**Figure 48.** EDS analysis on the nanowires grew on  $\text{Sr}_8\text{Ga}_{16}\text{Ge}_{30}$

Because the nanowires grew on the surface of the  $\text{Sr}_8\text{Ga}_{16}\text{Ge}_{30}$  powder, the EDS still shows the composition of  $\text{Sr}_8\text{Ga}_{16}\text{Ge}_{30}$ .

#### Experiment #2:

A similar experiment was conducted in the same condition. The only difference was the sample was not mixed with gold nanoparticles. No nanowires were observed in the experiment.

#### Experiment #3:

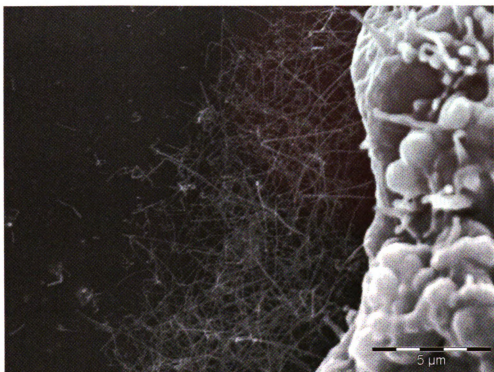
A similar experiment was conducted in the same condition. The only difference was the sample was annealed for shorter period of time. The results were similar to Experiment #1. The nanowires were scattered on the surface of the  $\text{Sr}_8\text{Ga}_{16}\text{Ge}_{30}$  powder.

#### Experiment #4:

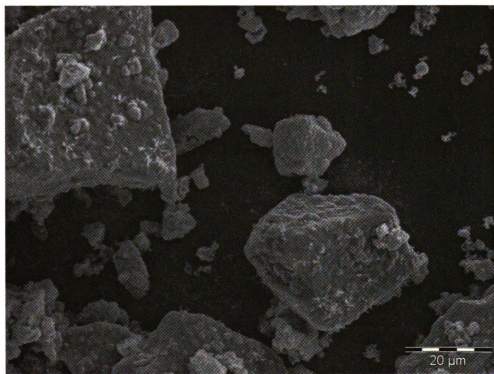
$\text{Sr}_8\text{Ga}_{16}\text{Ge}_{30}$  powder was mixed with gold nanoparticles were annealed at  $825^\circ\text{C}$  for 120 minutes. We slightly increased the annealing temperature to  $825^\circ\text{C}$  and used the same annealing time, 120 minutes. We used silicon wafer instead of quartz plate.

In Figure 49 and 50, the dark area is the silicon wafer. We found that the density of nanowires was higher close to the powder. Most nanowires were found within a  $5\text{ }\mu\text{m}$  region around isolated powder particles, and higher densities of nanowires were found between clusters of powder particles as shown in Figure 8.

In the SEM image in Figure 49 shows the nanowires on the quartz plate were scattered around the  $\text{Sr}_8\text{Ga}_{16}\text{Ge}_{30}$  powders. In addition, there were some nanowires growing on the surface of the powder.



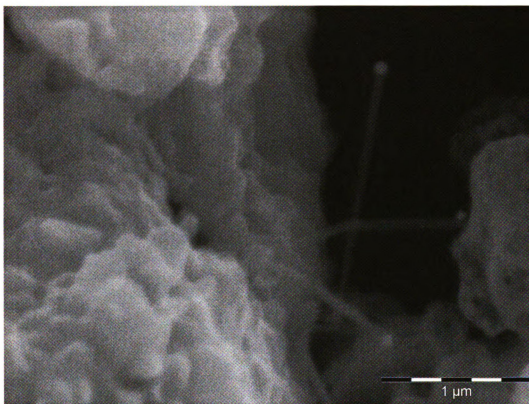
**Figure 49.** The SEM image shows the nanowires around the Sr<sub>8</sub>Ga<sub>16</sub>Ge<sub>30</sub> powder.



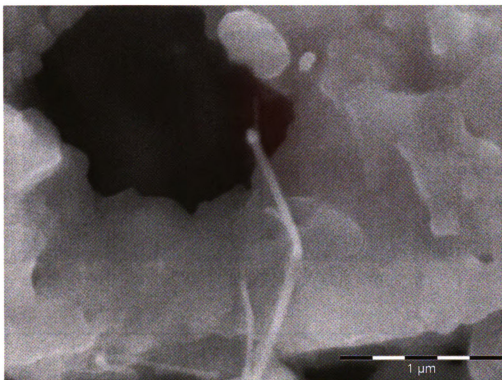
**Figure 50.** The nanowires scattered around the Sr<sub>8</sub>Ga<sub>16</sub>Ge<sub>30</sub> powders.

The SEM image in Figure 50 shows the nanowires on the quartz plate were scattered around the  $\text{Sr}_8\text{Ga}_{16}\text{Ge}_{30}$  powder and growing on the surface of the powder. This suggests that a vapor transport of one or more component from the material is occurring during growth of the nanowires.

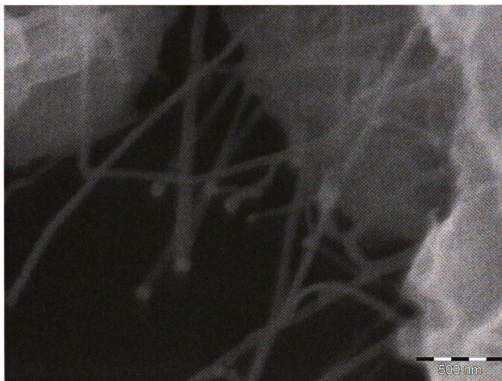
In Figure 51, the nanowires show a uniform diameter along the length of the nanowires ranging from 40 nm to 100 nm and the average length was 1.5  $\mu\text{m}$ . These ball-shape tips were observed in the majority of wires characteristic of the vapor-liquid-solid growth mechanism. Most of the wires were remarkably straight without being kinked.



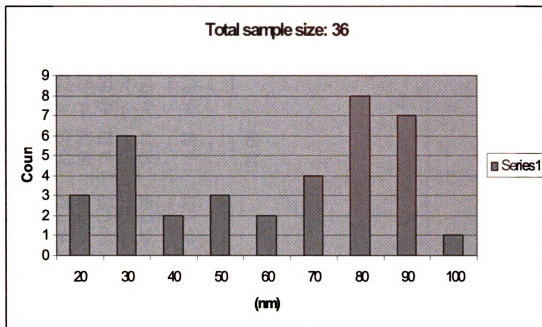
**Figure 51.** The SEM image shows the distinctive structure of the nanowires.



**Figure 52.** The average diameter was 40 nm and the average length was 1.5 μm.



**Figure 53.** The average diameter of nanowires was about 100 nm.

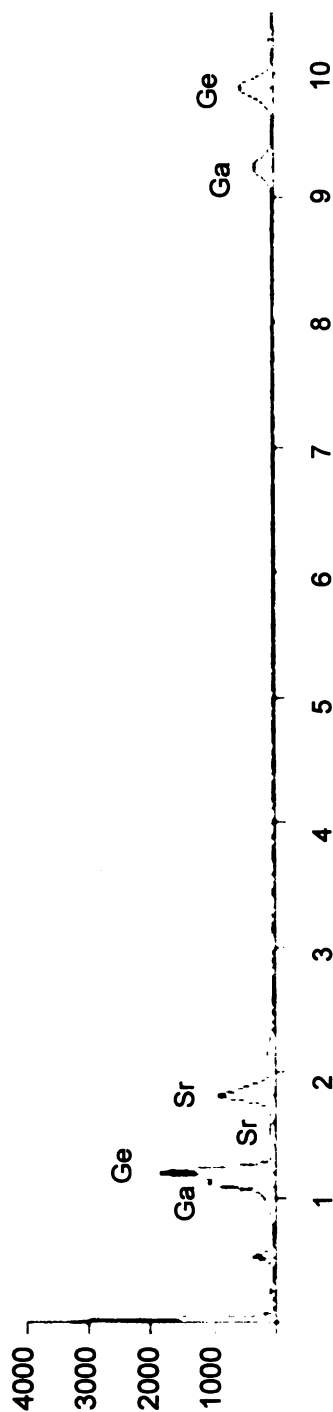


**Figure 54.** Histogram showing the diameter of nanowires. Total sample size: 36. The average diameter is 62.22 nm.

The SEM image in Figure 53 shows nanowires that grew on the surface of the  $\text{Sr}_3\text{Ga}_{16}\text{Ge}_{30}$  powder. These nanowires had gold balls formed at the tips and the average diameter of the nanowires was about 100 nm. The histogram in Figure 54 shows the diameter distributions of the grown nanowires. The average dimension was about 62.2 nm in diameter.



Element Line	K-Ratio	Z	A	F	ZAF	Weight % Error	Weight % Error	Norm. Wt.% Err	Atom % Error	Atom % Error
C K	0.016	0.792	9.387	1.000	7.430	7.97	+/- 0.88	+/- 0.88	21.13	+/- 2.32
O K	0.076	0.835	6.074	0.999	5.066	25.16	+/- 0.68	+/- 0.68	50.09	+/- 1.35
Ga K	0.250	1.111	0.996	0.993	1.100	17.99	+/- 0.67	+/- 0.67	8.22	+/- 0.31
Ga L	0.000	0.000	0.000	0.000	0.000	--	--	--	--	--
Ge K	0.508	1.127	0.995	0.990	1.110	36.95	+/- 0.98	+/- 0.98	16.21	+/- 0.43
Ge L	0.000	0.000	0.000	0.000	0.000	--	--	--	--	--
Sr K	0.149	1.194	1.022	1.000	1.220	11.94	+/- 1.01	+/- 1.01	4.34	+/- 0.37
Sr L	0.000	0.000	0.000	0.000	0.000	--	--	--	--	--
Sr M	0.000	0.000	0.000	0.000	0.000	--	--	--	--	--
Total						100.00			100.00	



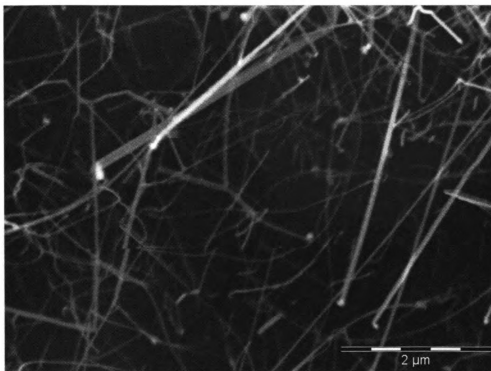
**Figure 55.** EDS analysis on the grown nanowires

Because the nanowires grew on the surface of the  $\text{Sr}_8\text{Ga}_{16}\text{Ge}_{30}$  powder, the EDS was taken on a region of nanowires with a powder particle as a substrate, thus the analysis still shows the composition of  $\text{Sr}_8\text{Ga}_{16}\text{Ge}_{30}$ .

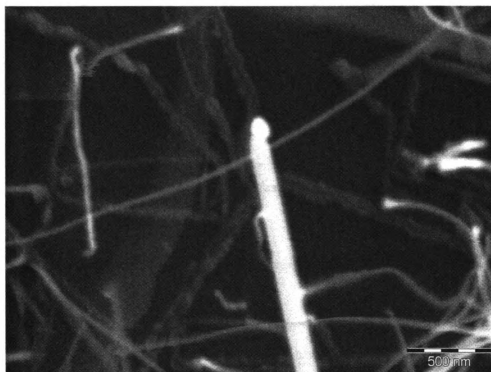
#### Experiment #5:

$\text{Sr}_8\text{Ga}_{16}\text{Ge}_{30}$  powder was mixed with gold nanoparticles and annealed at temperature at  $740^\circ\text{C}$  for 40 minutes with quartz plate on top of it. From the previous experiments, we found out the density of nanowires was higher in the region closer to the  $\text{Sr}_8\text{Ga}_{16}\text{Ge}_{30}$  powder. In the following experiment, we used this phenomenon to increase the amount of nanowires.

The  $\text{Sr}_8\text{Ga}_{16}\text{Ge}_{30}$  pile was mixed with colloidal Au of 20 nm nominal size and with polyisene-L to avoid colloidal clustering, and the sample was subsequently annealed at  $740^\circ\text{C}$  for 40 minutes. We put a piece of quartz plate on top of the pile as a local vapor confinement technology.



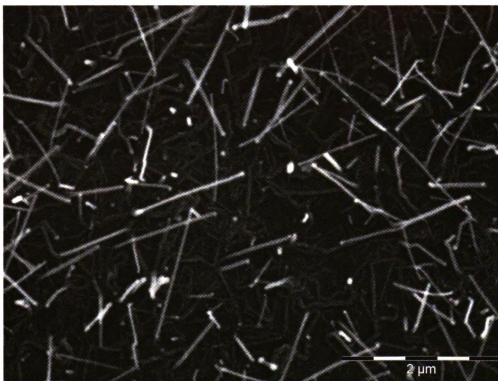
**Figure 56.** The length of nanowire was over 4  $\mu\text{m}$ . Additionally, some nanowires were observed to form as a ball shape in the tip. (2 $\mu\text{m}$  scalebar).



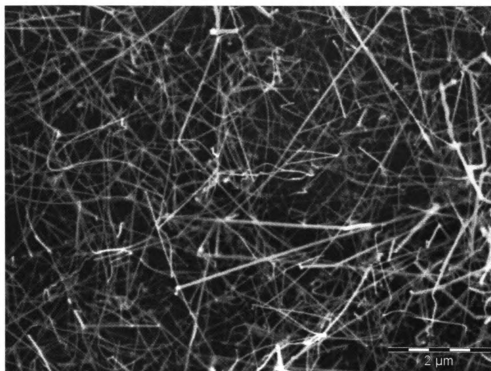
**Figure 57.** The diameter of nanowires ranged from 40 to 200nm. (500nm scalebar).

The SEM images show the growth of nanowires from the  $\text{Sr}_8\text{Ga}_{16}\text{Ge}_{30}$  powder (Figure 57 and 58). The nanowires had gold balls formed at the tips, which suggests the dominance of the VLS growth mechanism.

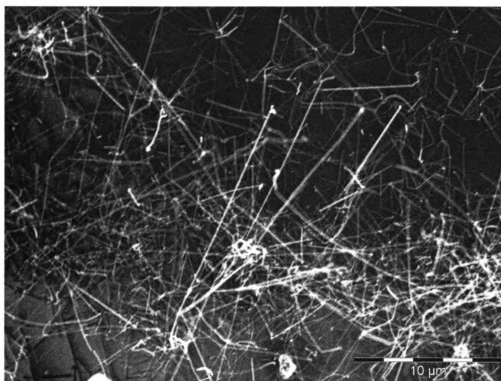
In the SEM image in Figure 58 and 59 the nanowires were observed on top of the quartz plate. Most wires appear straight and the diameters were relatively uniform. Again gold balls can be seen at the tips.



**Figure 58.** Nanowires on top of the quartz plate. The scale bar is 2 μm.

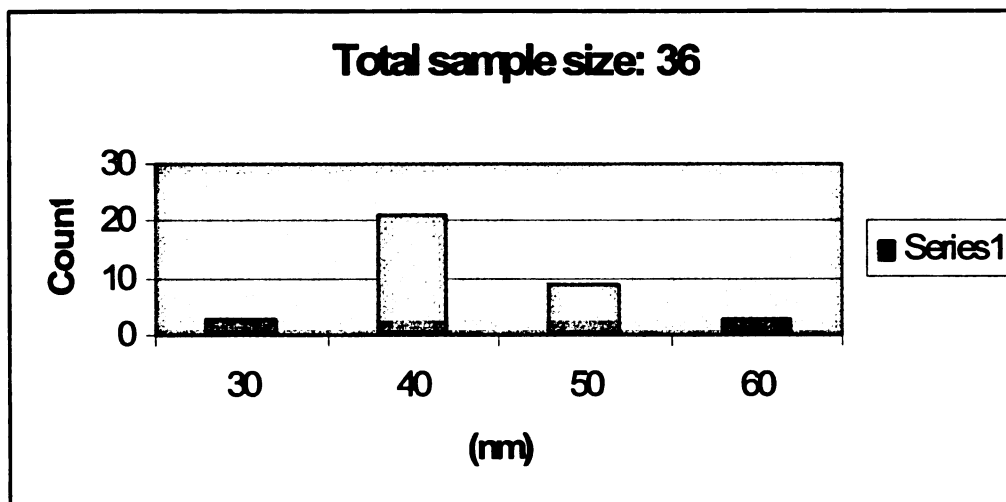


**Figure 59.** The dark region is the quartz plate. The scale bar is 2 μm.



**Figure 60.** The scale bar is 10 μm.

The SEM images show nanowires grown from the  $\text{Sr}_8\text{Ga}_{16}\text{Ge}_{30}$  powder (Figure 58 through Figure 60). The nanowires were very straight with gold balls formed at the tips.

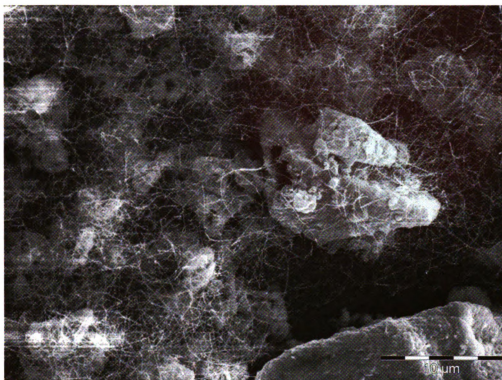


**Figure 61.** Histogram showing the diameter of nanowires. Total sample size: 36. Average diameter 43 nm.

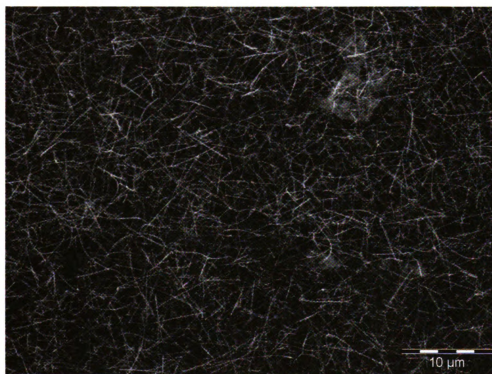
The histogram in Figure 61 shows the diameter distributions of the grown nanowires. The average dimension was about 43nm in diameter.

#### Experiment #6:

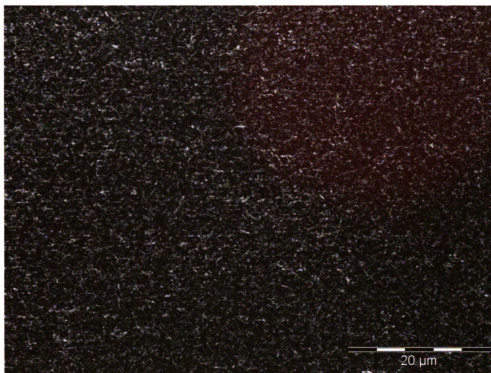
We increased the annealing temperature to 950°C and used the same annealing time, 40 minutes. A higher density of nanowires was found for this sample compared to previous experiments as shown in Figure 62. The average diameter was about 60 nm and the length was about 1.5  $\mu\text{m}$ . In the SEM image in Figure 63, was taken in the quartz area far removed from the  $\text{Sr}_8\text{Ga}_{16}\text{Ge}_{30}$  powder. The diameter was about 40 nm and the length was about 1.5  $\mu\text{m}$ . The scale bar is 10  $\mu\text{m}$ . The density of these nanowires was uniformly distributed over the quartz substrate as shown in Figure 64.



**Figure 62.** The diameter was about 60 nm and the length was about 1.5 μm.



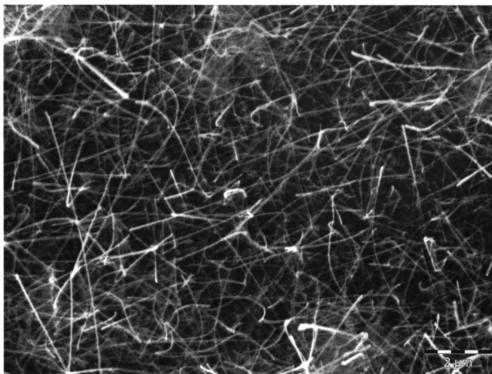
**Figure 63.** The diameter was about 40 nm.



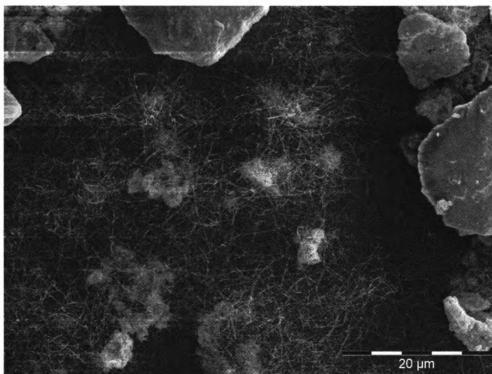
**Figure 64.** The density of these nanowires was uniformly distributed over the quartz substrate.

In the SEM image in Figure 65, the high density of nanowires was observed to emerge in the quartz plate outside the  $\text{Sr}_8\text{Ga}_{16}\text{Ge}_{30}$  region. The length was about 2 μm and the diameter was about 120 nm. The scale bar is 2 μm. In the SEM image in Figure 66, the zoom out image shows nanowires were grown between the powder particles. There is a difference in the diameter of the nanowires. Because some images are closer to powder particles, and others are farther away.

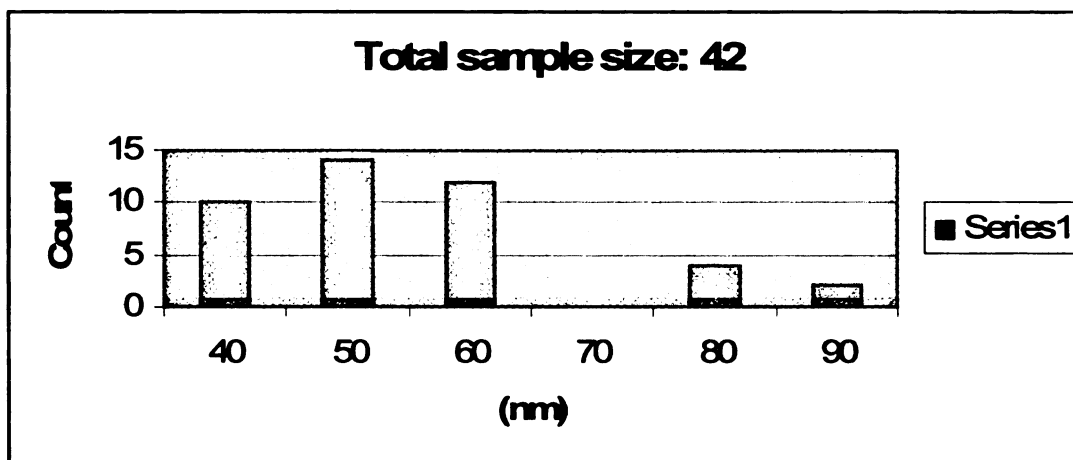




**Figure 65.** The length was about 2  $\mu\text{m}$  and the diameter was about 120 nm.



**Figure 66.** The scale bar is 20 $\mu\text{m}$ .



**Figure 67.** Histogram showing the diameter of nanowires. Total sample size: 42. Average diameter is 55.24 nm

The histogram shows the diameter distributions of the grown nanowires. The average dimension was about 55.2 nm in diameter.

### 3.3 Discussion

In experiments of growing nanowires from  $\text{Sr}_8\text{Ga}_{16}\text{Ge}_{30}$ , we have produced nanowires from  $\text{Sr}_8\text{Ga}_{16}\text{Ge}_{30}$  by simply mixing it with Au nanoparticles and using a local vapor confinement technique. Analysis of the nanowires shows we were not successful in growing  $\text{Sr}_8\text{Ga}_{16}\text{Ge}_{30}$  nanowires, instead  $\text{Ga}_2\text{O}_3$  nanowires were formed. A couple of factors are observed to have affected the results, and gold is one of them. It was shown that there was no growth of nanowires taking place without having gold nanoparticles mixed with the sample. From the images shown, the gold balls clearly appeared at the tips, which was an indication that the growth mechanism was the well-known vapor-liquid-solid mechanism. From the TEM analysis, the nanowires were found to be gallium oxide nanowires. Contrary to our expectation, strontium and germanium were

not present in the nanowires. In addition to gold, the second factor influencing the growing of nanowires from  $\text{Sr}_8\text{Ga}_{16}\text{Ge}_{30}$  is the vapor pressure. By confining the source  $\text{Sr}_8\text{Ga}_{16}\text{Ge}_{30}$  material between quartz plates and adding gold nanoparticles, a significant increase in the density of grown nanowires was observed. In addition, the diameter of wires became uniform and nanowire growth could be found over broad regions of the quartz substrate. Without the additional confinement on the source material, nanowires were only found in close proximity to the source material.

## **Chapter 4 Growth of Nanowires from Germanium**

One-dimensional semiconducting oxides nanostructures which have fascinating stability and optical properties have attracted much attention because of their potential applications in different fields such as optoelectronics and sensing. Germanium dioxide, as a promising material, has been extensively studied on its optical and electronic properties, and the growth of germanium dioxide nanowires has been studied by different methods. Thermal annealing of germanium under sub-atmosphere condition leads to the growth of a dense distribution of wires with diameters ranging from tens to hundreds of nanometers and lengths of up to tens of microns on the substrate surface. This study simply uses oxygen, which exists in the air, to react with germanium at certain temperatures to form nanowires. The products are characterized by scanning electron microscopy (SEM), transmission electron microscopy (TEM) as well as selected area electron diffraction (SAED) pattern. The observations show the nanowires are crystalline  $\text{GeO}_2$  nanowires.

### **4.1 Introduction**

Therefore, in order to meet the demands of further applications, it is imperative to make use of the effect by combining nanowires and related optical properties and specific sizes. Germanium dioxide is a blue luminescence material with a high refractive property, and low optical loss [52]. Such properties have found great interest in the fabrication of low loss optic fibers composed of  $\text{SiO}_2$  and  $\text{GeO}_2$ . Considering these

superior properties and their impact on the industry, germanium dioxide deserves further investigation

### Germanium Dioxide (GeO<sub>2</sub>)

This is the most common solid compound of germanium. Germanium dioxide takes shape in one amorphous and two crystalline modifications:

- 1) A glassy amorphous form, refractive index 1.607, density 3.64 g/(cm<sup>3</sup>) at 20° C.
- 2) A tetragonal rutile form, refractive index 2.05, density 6.24 g/(cm<sup>3</sup>) at 20° C.
- 3) White hexagonal quartz modification, refractive index 1.735, density 4.7 g/(cm<sup>3</sup>) at 18° C.

The tetragonal form is practically insoluble in water, while the hexagonal and the amorphous modifications have low solubilities; 0.45 and 0.52 % respectively, at 25° C. Aqueous solutions are acidic due to the formation of metagermanic acid, H<sub>2</sub>GeO<sub>3</sub>. The hexagonal modification converts to a tetragonal crystal system when heated at 350° C in water under pressure. Both crystalline forms convert to a glass-like amorphous GeO<sub>2</sub> when heated at 1100° C [53]. It is a stable, unreactive white powder which melts to a glass and can be used as a component of glass which is more refractive than the matching silicate glasses. It is readily obtained by the hydrolysis of GeCl<sub>4</sub>, generating a microcrystalline form of the hexagonal modification of GeO<sub>2</sub>, bearing the structure similar to that of low quartz. This is often called the “soluble” form that dissolves in cold water to the extent of 4g/l. In a similar fashion, the same crystalline modification is obtained by keeping GeO<sub>2</sub> glass at 1080° C until it devitrifies. The only other modification of GeO<sub>2</sub> is the “insoluble” or tetragonal form, which is obtained by the

hydrothermal conversion of the “soluble” form through heating with water at 355° C for 100 hours. The “insoluble” form is stable up to 1033° C, where it inverts slowly to the “soluble” form, which will melt at 1116° C [54].

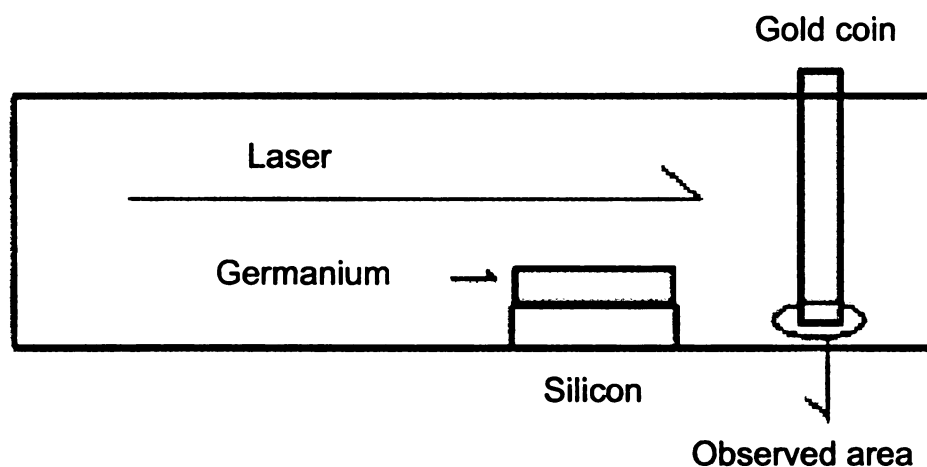
To produce GeO<sub>2</sub> nanowires, various mechanisms have been utilized, including physical evaporation [55], thermal treatment [56], carbon nanotube confined reaction of Ge [57], laser ablation [58], heating in oxygen environment [59], thermal oxidation [60], and carbothermal reduction reaction [61].

## **4.2 Experiments**

### **Experiment #1:**

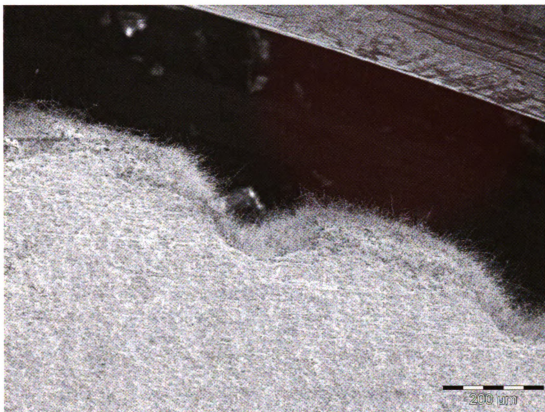
A layer of gold was deposited on a germanium wafer at 850° C. The germanium chunk was put on top of the silicon wafer and subsequently annealed to 850° C. After reaching 850°C, a KrF laser was used (500 mJ, 10 Hz for 90 seconds) to ablate a gold target. Room air was allowed to flow into the hot chamber for 10 minutes to increase the pressure to 350 Torr. Then the vacuum pump was turned on to evacuate the chamber, and the furnace was turned off until to cool down.

The experiment was conducted within a quartz tube (outer diameter, 90mm; length, 80 cm) heated by a horizontal tube furnace. The sample was put at the center of a quartz boat that was placed at the center of the quartz tube. The tube was evacuated to about 30 mTorr. Figure 68 shows the experimental setup.



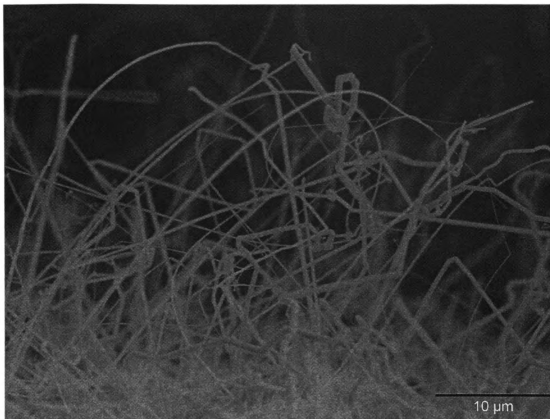
**Figure 68.** The experimental setup, for investigating the growth of  $\text{GeO}_2$  nanowires.

Figure 68 shows the setup and the observed area, of which the SEM images were taken. The SEM image in Figure 69 was taken in the observed area as shown in Figure 68. According to the setup system in Figure 68, the only opening for gas flow in this system is the gap between the gold coin and the tube. After the experiment, nanowires were found to emerge along the gap on side of the gold coin. The SEM image in Figure 69 shows the edge of the gold coin. The nanowires did not find on the germanium or silicon wafer. The nanowires were found on the surface and the edge of the gold coin.



**Figure 69.** The SEM image shows the edge of the gold coin. The scale bar is 200  $\mu\text{m}$ .

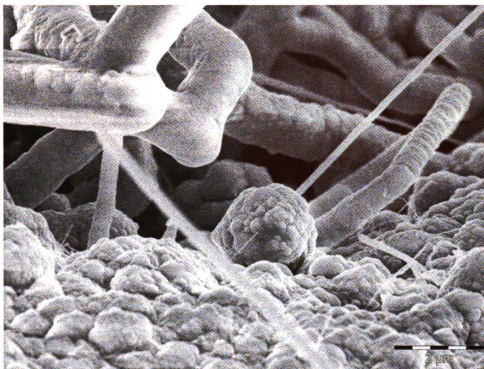




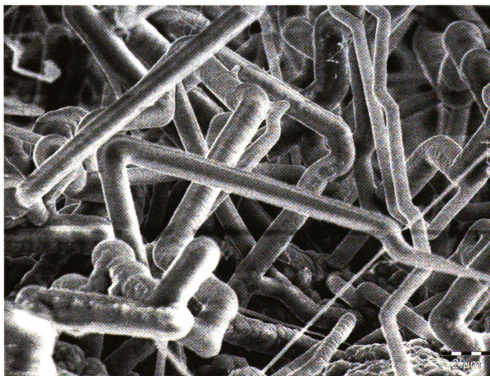
**Figure 70.** The SEM image of nanowires on the surface of gold coin. The scale bar is 10  $\mu\text{m}$ .

The SEM image in Figure 70 shows that the nanowires were over 30  $\mu\text{m}$  in length. The diameters of nanowires were between 100 to 1000 nm, and those with smaller diameters were found to be much straighter than the larger diameter wires. The larger diameter nanowires occasionally changed direction during their growth creating the kinked shape.

The SEM image in Figure 71 shows the wires at the edge of the gold coin. The diameters of the wires shown in Figure 71 ranged from 100 to 1000 nm and the larger wires were kinked. The smaller nanowires are more clearly seen in this image as straight and short in length.

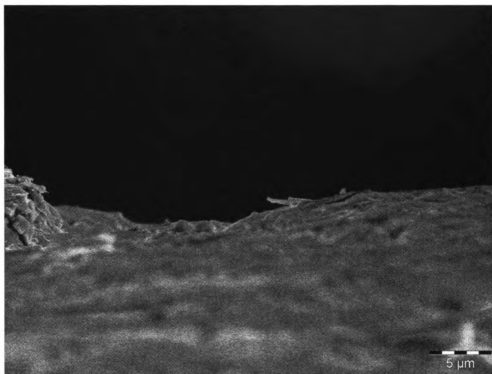


**Figure 71.** The SEM image shows the whiskers at the edge. The scale bar is 2  $\mu\text{m}$ .



**Figure 72.** The whiskers with kinked shape. The scale bar is 2  $\mu\text{m}$ .

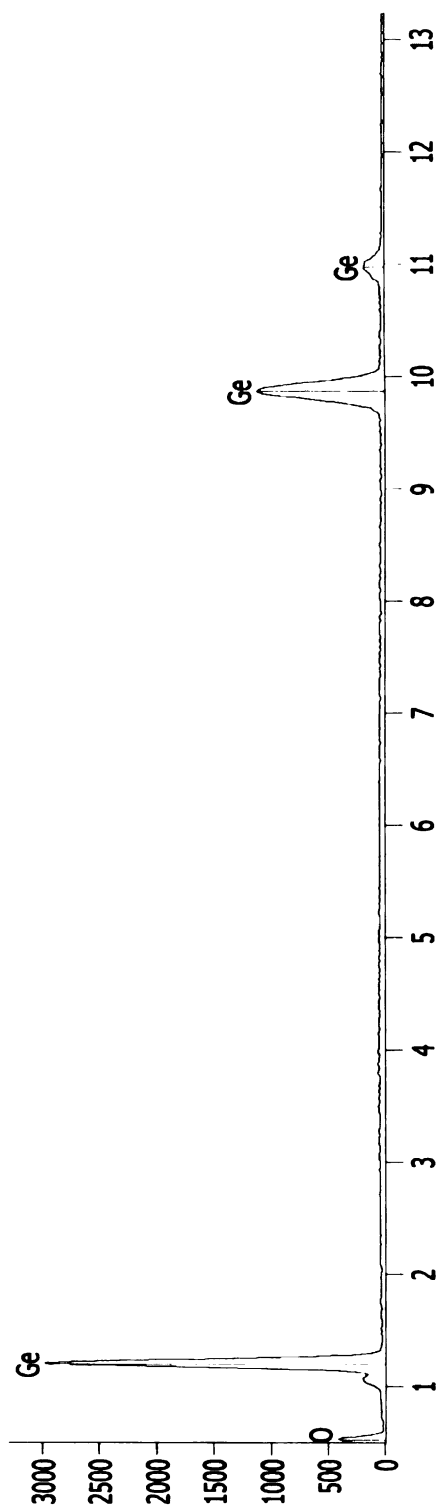
Figure 72 shows the SEM image of the germanium oxide nanowires. The kinked nanowires had an average diameter of 1  $\mu\text{m}$ . Between those large wires, there were some nanowires with an average diameter of 100 nm.



**Figure 73.** Away from the observed area, no nanowires were observed.

Figure 73 shows the SEM image taken at the edge of the gold coin that was far from the chamber exhaust opening. There were no nanowires observed in this area. From this observation it was hypothesized that germanium was volatilizing into the gas stream such that the edge of the gold coin that was exposed to the highest concentration of germanium (or germanium oxide) gas molecules was the location of nanowires growth.

Element	K-Ratio	Z	A	F	ZAF	Weight %	Weight % Error	Norm. Wt.% Err	Atom %	Atom % Error
Line										
C K	0.004	0.774	9.701	1.000	7.502	2.00	+/- 0.66	+/- 0.66	6.19	+/- 2.03
O K	0.076	0.816	5.268	0.999	4.293	23.98	+/- 0.51	+/- 0.51	55.83	+/- 1.18
Ge K	0.920	1.099	0.994	1.000	1.093	74.02	+/- 1.08	+/- 1.08	37.98	+/- 0.55
Ge L	0.000	0.000	0.000	0.000	0.000	---	---	---	---	---
Total						100.00			100.00	



**Figure 74.** EDS analysis on the nanowires.

In Figure 74 the EDS analysis on the nanowires showed the composition of nanowires were germanium and oxygen. The germanium to oxygen ratio was about 0.68 for an average composition of  $\text{GeO}_{2-x}$  with  $x = 0.53$ .

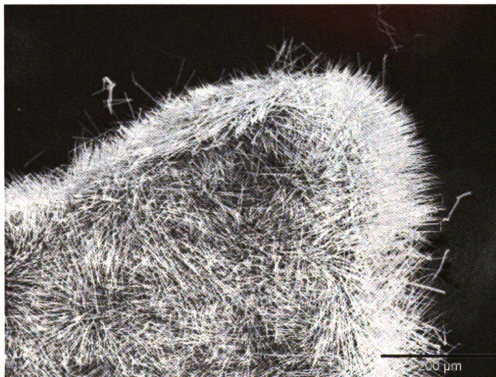
The germanium oxide nanowires and whiskers on the edge of the gold coin might indicate that the gold did play a role as metal catalyst. The following experiments were designed to test this assumption.

#### Experiment #2:

A layer of gold was deposited on top of germanium wafer at room temperature. The piece of germanium was placed on top of an uncoated silicon wafer and another piece of silicon wafer with gold deposited (~10nm thick) was put on top of it, subsequently annealed to 850° C. It was then left at 850° C for 40 minutes with Ar/H (95/5) flow at 200 sccm to reach 10 Torr. Then the Ar/H flow was shut off and room air was allowed to flow into hot chamber for 1 minute until a pressure 350 Torr was obtained. The vacuum pump was then turned on, and the furnace was turned to initiate the cool down.

The experiment was conducted within the same quartz tube heated by a horizontal tube furnace. The sample was placed at the center of quartz boat. The quartz boat was placed at the center of a quartz tube, which was evacuated to about 30 mTorr. A background gas of argon flow of 200 sccm traveled along the quartz tube, which was maintained in state throughout the entire reaction time. The pressure inside the tube increased from 30 mTorr to 150 mTorr after the argon gas entered the tube.

The SEM image in Figure 75 shows the silicon wafer with a layer of gold was covered with dense germanium oxide nanowires on its surface, which helps us to prove the assumption, which germanium oxide nanowires and whiskers on the edge of the gold coin might indicate that the gold did play a role as metal catalyst. Most of the nanowires were in very straight shape.



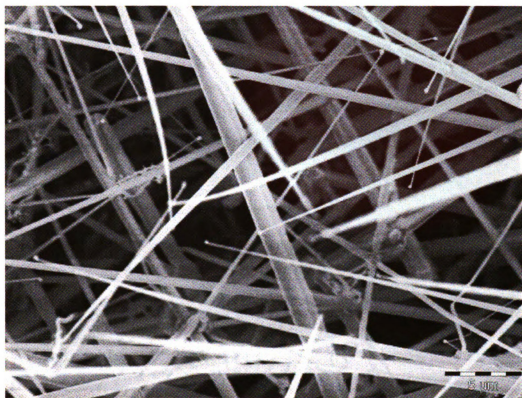
**Figure 75.** The silicon wafer was covered with dense germanium oxide nanowires.



**Figure 76.** The growth of nanowires on the edge of a silicon wafer. The scale bar is  $10\text{ }\mu\text{m}$ .

The SEM image in Figure 76 shows the growth of nanowires on the edge of the silicon wafer. The nanowires tapered off and the accompanied bright dots were at the tip. The gold dots at the tips clearly confirmed the VLS growth mechanism.

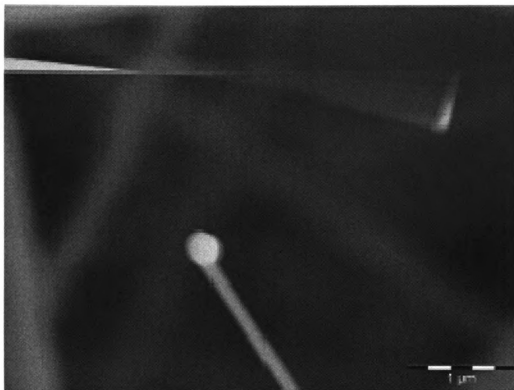
On the silicon surface that was coated with gold, a high density of nanowires were found with diameters that tapered to points at the tips which terminate at a gold dot as shown in Figure 77. Nanowires had diameters of  $90\text{ nm}$  at the tip; however, in some sections of the wires, the diameter was  $2\text{ }\mu\text{m}$ .



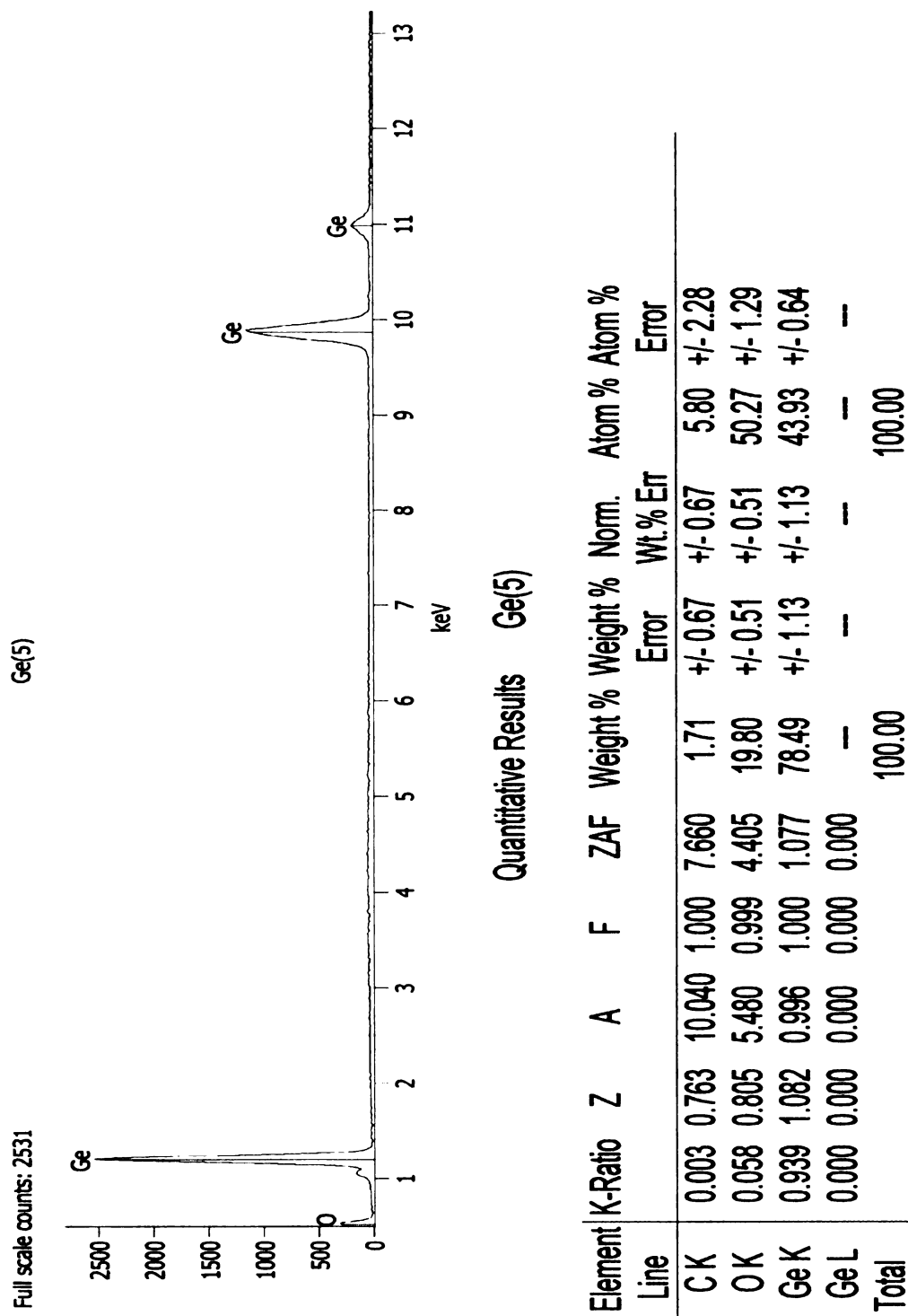
**Figure 77.** The gold balls were appeared at the tip of nanowires. The scale bar is 5  $\mu\text{m}$ .

The image of higher magnification is shown in Figure 78 where the growth of germanium oxide nanowires is observed. The diameter of nanowires was about 100 nm, and the diameter of the accompanied bright dots was 200 nm.





**Figure 78.** The image of a nanowire at a higher magnification (1  $\mu\text{m}$  scalebar).



**Figure 79.** EDS analysis on the nanowires.

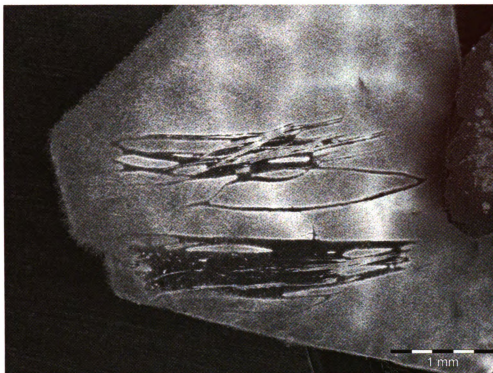
In the Figure 79 EDS analysis on the nanowires shows the composition of the nanowires were germanium and oxygen. The germanium to oxygen ratio was about 0.88.

The result shows the silicon wafer with a layer of gold was covered with dense germanium oxide nanowires on its surface. We wanted to verify that the growth mechanism was metal catalyst. So the following experiments were conducted.

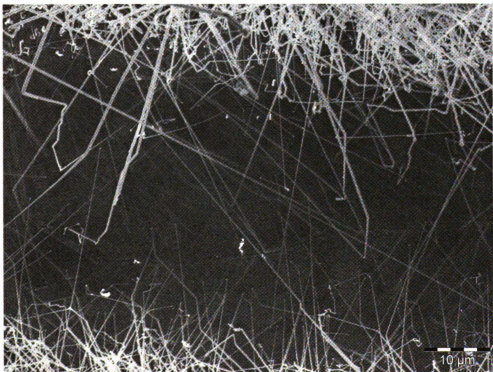
### Experiment # 3:

The experiment was designed to study the effects of gold on the growth of  $\text{GeO}_2$  nanowires. A 10 nm thick layer of gold was deposited onto a silicon wafer. A small area was then scratched to remove some of the gold. The scratched sample was then placed on top of a piece of germanium which was on top of a silicon wafer. The Si/Ge/Si(with scratched Au film) was heated in a quartz tube to  $850^\circ\text{C}$ . It was then left at  $850^\circ\text{C}$  for 40 minutes with Ar/H (95/5) flow at 200 sccm to reach 10 Torr. Then the Ar/H flow was shut off and room air was allowed to flow into the hot chamber for 1 minute until a pressure of 350 Torr was reached. The vacuum pump was then turned on, and the furnace was turned off.

The resulting images are shown in Figure 80 through Figure 82 and show that the gold was essential for the nanowire growth. The SEM image in Figure 80 shows the silicon wafer having 10 nm thick gold coated. Most areas on the surface were covered with a white wool-like layer, which was essentially made of germanium oxide nanowires. Before the experiment, tweezers were carefully used to scratch a few lines on the gold-coated layer. After the experiment, no growth of nanowires was observed along these lines.

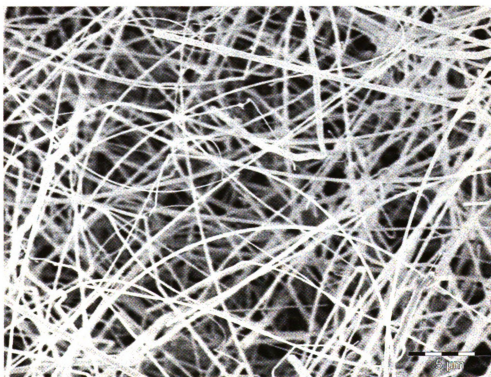


**Figure 80.** The silicon wafer only partially covered by nanowires (1mm scalebar).



**Figure 81.** A closeup image of a scratched region showing that the growth of nanowires only occurred in the gold coated areas. The scalebar is 10  $\mu\text{m}$

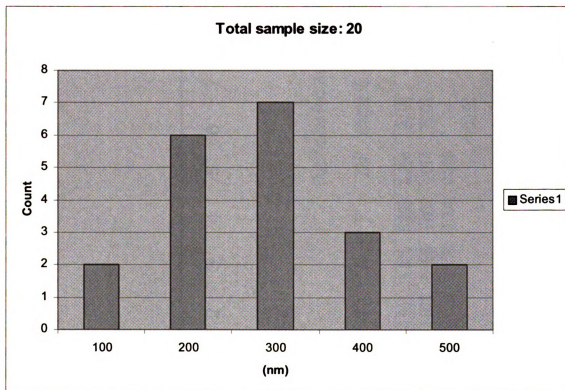
The SEM image in Figure 81 shows a dark region in the center where the gold layer was mechanically removed before heating the substrate. The wires in the growing region had long length that could be extended into the dark region. Some nanowires were over 40  $\mu\text{m}$  in length with diameters of less than 100 nm. Bright dots could also be found at their tips. Nanowires with larger diameters of 200-300 nm usually exhibited more kinking and bright dots at the tips could not be found.



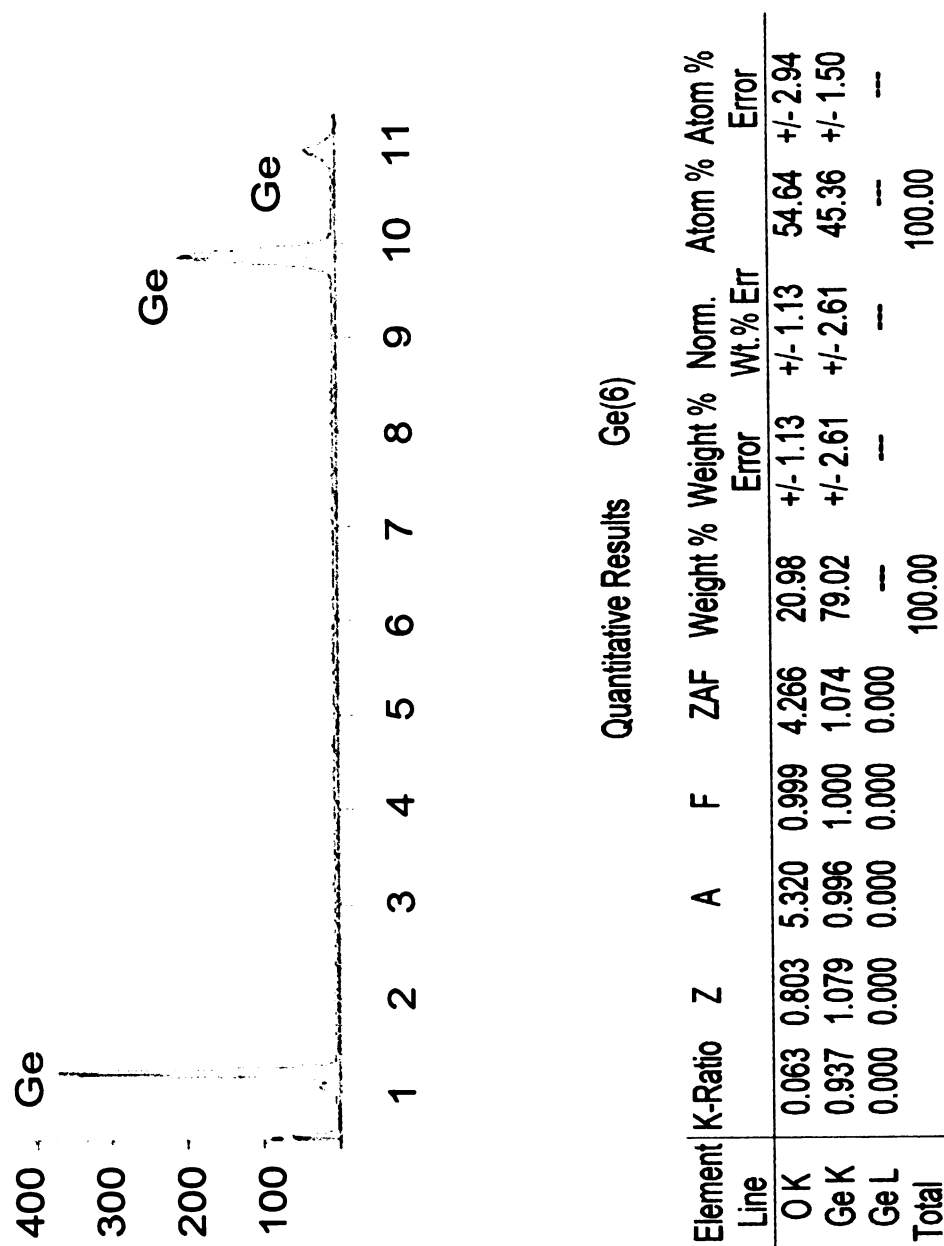
**Figure 82.** The dense of nanowires were observed on the surface of silicon wafer. The scale bar is 5  $\mu\text{m}$ .

The SEM image in Figure 82 shows that the nanowires grew in the gold-rich area. The diameters of nanowires ranged from 100 nm to 500 nm. The bright dots were found at the tips of nanowires with smaller diameters. The kinked shape was usually present in nanowires with big diameters.

The histogram in Figure 83 shows the diameter distributions of the grown wires. The average dimensions of the grown wires were about 285 nm in diameter. In Figure 84 EDS analysis on the nanowires showed the average composition to be  $\text{GeO}_{2-x}$  with  $x = 0.8$ .



**Figure 83.** Histogram showing the diameter of nanowires. Total sample size: 20. The average diameter is 285 nm.

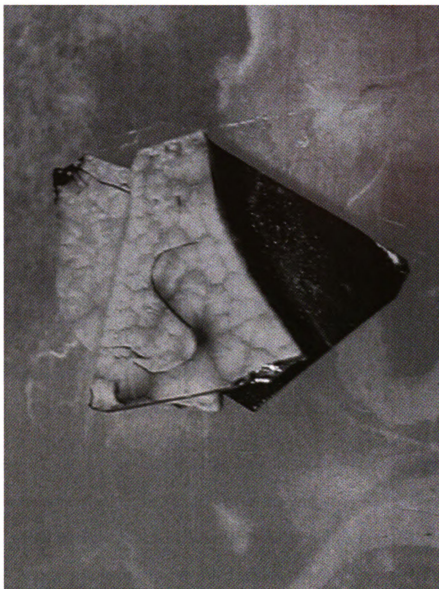


**Figure 84.** EDS analysis on the grown nanowires.

#### Experiment #4:

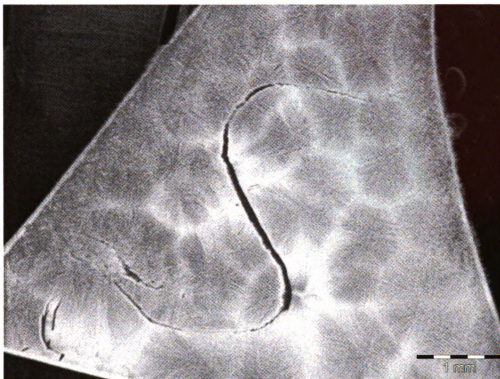
A piece of germanium was put on top of two silicon wafers, one is gold coated and the other is uncoated. Then a second piece of silicon with a gold coating (~10 nm thick) was placed on top of germanium, and the stack was subsequently annealed to 850° C. Before annealing, the gold coated substrate was scratched in the form of the character "S". Then the system was left at 850° C for 40 minutes with Ar/H (95/5) flowing at 200 sccm to reach 10 Torr. The Ar/H flow was then shut off and room air was allowed to flow into the hot chamber for 1 minute to reach a pressure of 350 Torr. Then the pump was turned on and the furnace turned off to allow the system to cool.





**Figure 85.** The image of the sample set.

Figures 85 through 87 show successively higher magnification of the top sample and demonstrate the control over growth location for the  $\text{GeO}_2$  nanowires. The “S” shaped scratch was formed using a diamond pen.

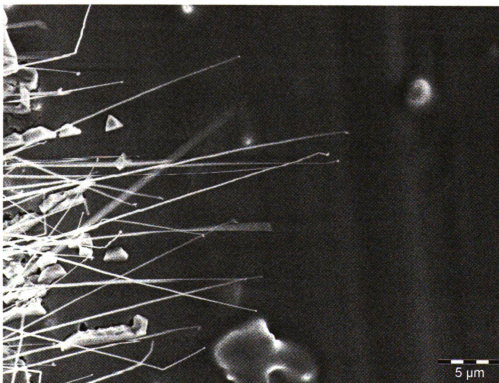


**Figure 86.** No growth happened in the “S” (1mm scale bar).

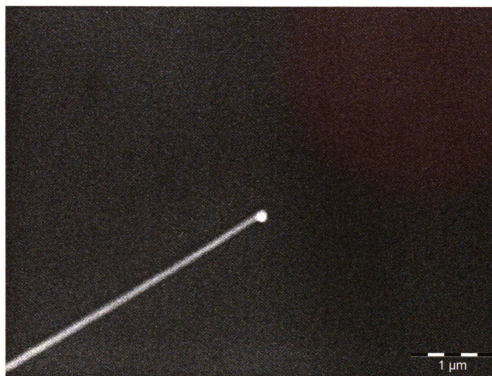
Figures 87 and 88 show different portions of the “S” and although nanowires extend over the scratched region, termination of the growth by removal of the gold is rather abrupt. Of the various nanowire materials studied in this thesis,  $\text{GeO}_2$  has shown the greatest control over location when using gold as the metal catalyst. The nanowires have lengths over  $20\text{ }\mu\text{m}$ , showing some tapering along the length of the wires, and a bright ball at the tip of each wire as in Figure 89. The diameter of the wire is approximately  $100\text{ nm}$  near the tip, with a  $150\text{ nm}$  diameter gold ball.



**Figure 87.** Dark region is no gold zone. The scale bar is 20  $\mu\text{m}$ .

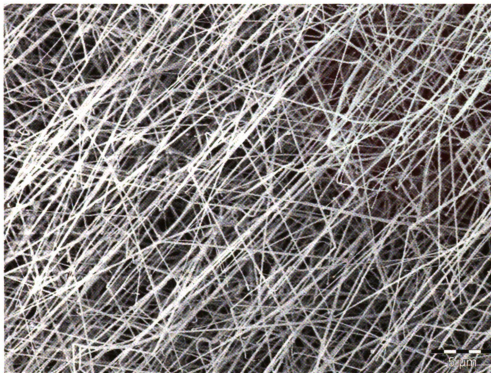


**Figure 88.** Nanowires extending into no gold zone. The scale bar is 5  $\mu\text{m}$ .

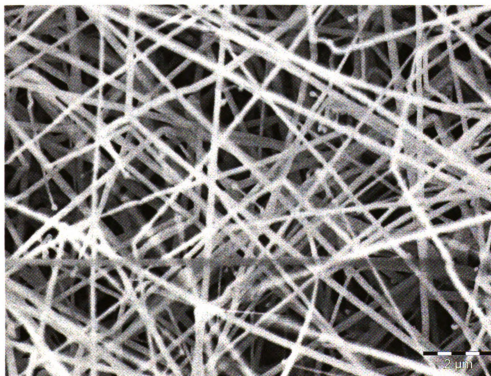


**Figure 89.** The nanowires had a bright dot at tip (1  $\mu\text{m}$  scalebar).

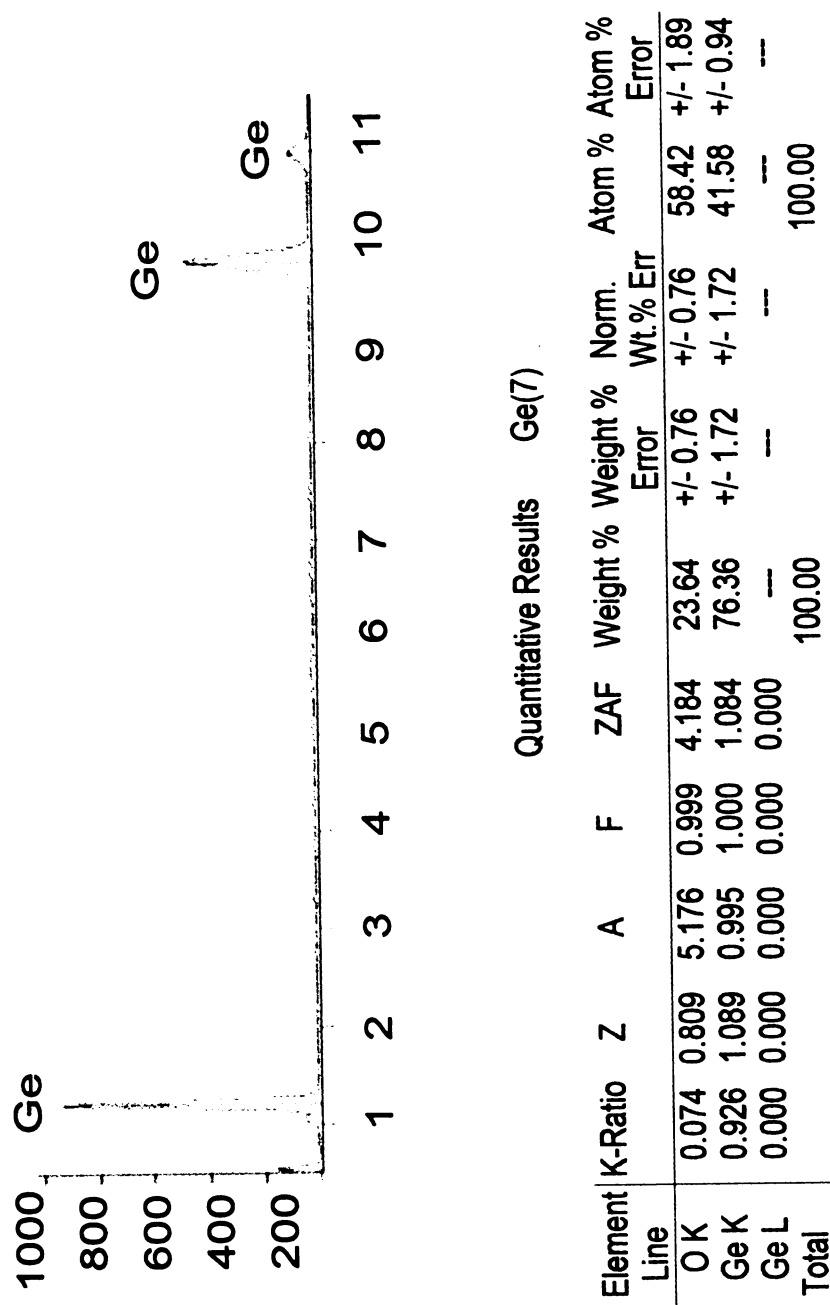
Far from the scratched region, the nanowires grew with high density as shown in Figure 90 and Figure 91. The diameters of nanowires ranged from 100 nm to 400 nm. EDS analysis of the nanowires in Figure 92 shows an average composition of  $\text{GeO}_{2-x}$  with  $x = 0.6$  suggesting that there is either a mixture of GeO and  $\text{GeO}_2$  nanowires, or some unoxidized germanium is being deposited. Further control over the oxygen partial pressure would be needed to investigate the compositional control of the nanowires, however it was found that nanowires did not grow when the pressure was maintained at 30 mTorr, and no room air was allowed into the chamber. It was thus concluded that both oxygen, and the metal catalyst (gold in this study) were required (in addition to the proper growth temperature) for successful nanowires growth.



**Figure 90.** Dense nanowires grown onto the surface (5  $\mu\text{m}$  scalebar).



**Figure 91.** Higher magnification SEM image of nanowires (2  $\mu\text{m}$  scalebar)..

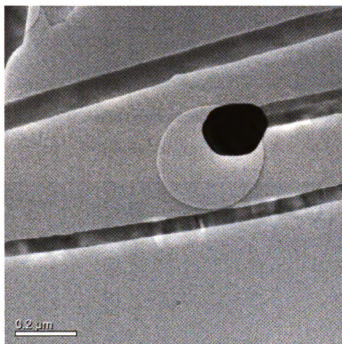


**Figure 92.** SEM EDS analysis on the nanowires.

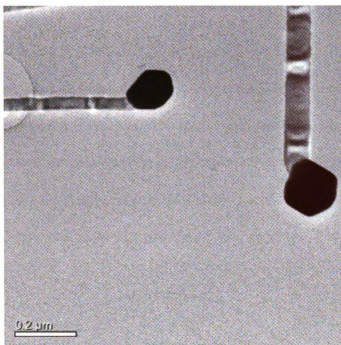


### TEM analysis

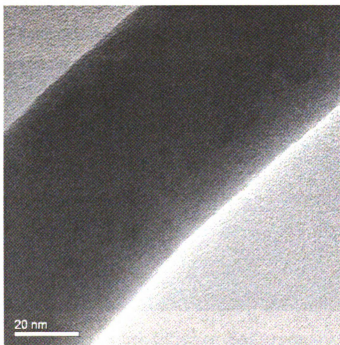
TEM samples were prepared by sliding a TEM copper grid on the surface of nanowire covered substrate. Many nanowires would break off and remain on the grid, and no post processing was needed. In some cases, the surface of a nanowire covered substrate was scraped with a razor blade, over a container of methanol. The methanol was then drawn into a pipette, and a small drop placed on a TEM grid. After evaporation, the TEM analysis was taken as shown in Figures 93 through 96.



**Figure 93.** TEM image shows the gold ball at the tip of the nanowires (0.2  $\mu\text{m}$  scalebar).

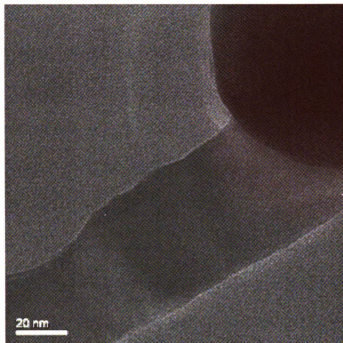


**Figure 94.** TEM image shows the nanowires have diameter about 40 nm (0.2  $\mu\text{m}$  scalebar).



**Figure 95.** TEM image shows the nanowires have diameter about 65 nm (20 nm scalebar).





**Figure 96.** TEM image shows the gold ball at tip of nanowires (20 nm scalebar).

Selective area electron diffraction (SAED) shows ordering in the nanowires, but was inconclusive for determining the orientation and lattice constant as shown below.



**Figure 97.** Selected area electron diffraction (SAED) pattern of nanowires.

### 4.3 Theory

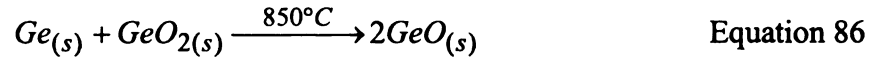
Germanium forms a wide range of binary compounds and eutectics with many metals and metalloid elements. In short, the metal is stable in air and water at ambient temperatures. Nonetheless, it reacts with oxygen at elevated temperatures engendering divalent and tetravalent oxides, GeO and GeO<sub>2</sub>. The amount of GeO<sub>2</sub> will grow with the increasing time of exposure to oxygen [62].

Germanium forms inorganic ionic and covalent compounds in both its +2 and +4 oxidation states [63]. Its +2 oxidation state is similar to that of a singlet state carbene in which Ge is sp<sup>2</sup> hybridized with a lone pair of electrons and an empty p orbital. This electronic configuration results in diverse structural types, which are determined mostly by steric factors ranging from V-shaped monomeric molecules to polymers. The stability of the +2 state is greater than Si and less than Sn. In its +4 oxidation state, Ge compounds are four-, five-, and six-coordinate. Some developments have been focused on the isolation of stable monomeric Ge<sup>IV</sup> compounds with an N or S double bond to germanium [63]. Germanium oxidation state +4 is more stable than the +2 oxidation state [53]. Therefore, germanium will oxidize easily in air to GeO<sub>2</sub>. Germanium dioxide has a high refractive index and infrared transmission, and is utilized in industrial glasses such as fiber optics.

We suggest that the process for the formation of the GeO<sub>2</sub> nanowires involves four steps. First, germanium is heated in the air and yields germanium (IV) dioxide, GeO<sub>2</sub> [64] as a thin layer on top of the germanium, Ge.



Second, the surface germanium dioxide continues to be heated with germanium while another chemical reaction takes place. The germanium dioxide,  $\text{GeO}_2$ , reduces to germanium monoxide,  $\text{GeO}$ . The metal also reduces the tetravalent oxide to the divalent oxide once heated at elevated temperatures

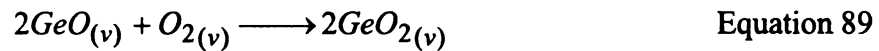


$\text{GeO}_2$  by itself is stable even under the condition of higher temperatures, but, when it comes to contact with Ge,  $\text{GeO}_2$  reacts with Ge at  $> \sim 710^\circ\text{C}$ , converts to  $\text{GeO}$ , and then sublimes.

Third, it is known that  $\text{GeO}$  can be removed from Ge surfaces through thermal annealing in a vacuum. Then  $\text{GeO}$  starts to vaporize above  $\sim 710^\circ\text{C}$ .



Fourth,  $\text{GeO}$  oxidation in air to  $\text{GeO}_2$  is rapid above  $550^\circ\text{C}$  [63]



The gold liquid droplet is a preferred location for deposition from the vapor, which causes the liquid to become supersaturated with  $\text{GeO}_{2(s)}$  nanowires growing from the gold seed on top of the silicon wafer via the vapor-liquid-solid mechanism [65]. The presence of a liquid layer in contact with the growing crystal has important consequences. The surface of the liquid has a large accommodation coefficient and is therefore a preferred site for deposition. Hence, the liquid becomes supersaturated with materials supplied from the vapor, and the crystal growth occurs through precipitation at the solid-

liquid interface. For a condensation reaction, the growth rate  $J$  (*atoms/cm<sup>2</sup> sec*) of an extensive crystal surface can be estimated from gas kinetics as:

$$J = \alpha \sigma \rho_0 (2\pi mkT)^{-\frac{1}{2}} \quad \text{Equation 90}$$

where  $\alpha$  is the accommodation coefficient,  $\sigma = (p - p_0)/p_0$  is the supersaturation of the vapor in which  $p$  is the vapor pressure, and  $p_0$  is the equilibrium vapor pressure of the solid at temperature  $T$ . The fraction of approaching atoms which become accommodated on the growing surface is  $\alpha$  [66].

#### 4.4 Discussion

After germanium (melting point: 938.3 °C) was exposed to air for 1 minute at 850°C, large quantities of white wool-like wires were found on top of the patterned silicon wafer on which a 10 nm thick layer of gold had been deposited, then scratched. The SEM images show that GeO<sub>2</sub> nanowires grew only where the gold was deposited. The SEM images also show the diameters of nanowires varied from 50 nm to several hundred nanometers, and they were tens of microns in length. TEM analysis showed more definitively the gold tips at the ends of the nanowires, and indicated ordering of the atoms in the nanowires.

#### 4.5 Conclusion

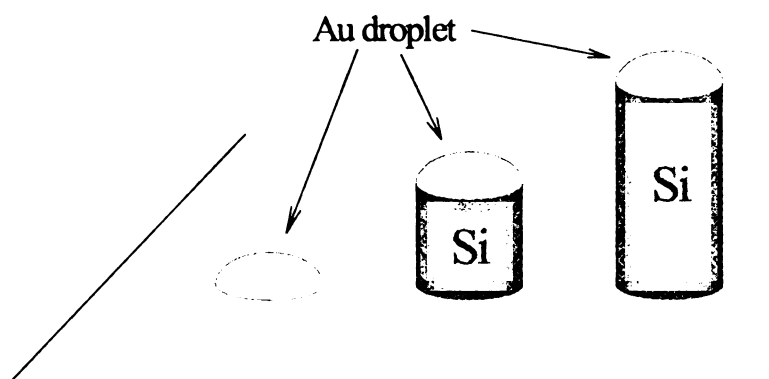
In summary, the thermal treatment of the germanium at 850° C under air flow led to a series of reactions forming nano- and microwires with diameters ranging from tens to hundreds of nanometers, and whose lengths were up to tens of microns on the substrate

surface. In contrast to other methods, the manipulation of controlling lower temperature and shorter reaction time appears to have evoked these chemical reactions. Moreover, the longer exposure to air resulted in the formation of nanowires with larger diameters. From these findings, it could be concluded that since nanowires only grow on the gold surface, the VLS mechanism plays an important role in the growth of nanowires. The presence of gold at the tip of the wire, as verified by EDS analysis, however the presence of oxygen during growth is also essential for growth of the nanowires.

## Chapter 5 Gold pattern experiment

### 5.1 Introduction

In the vapor-liquid-solid (VLS) technique, a metal is chosen based on the phase diagram between that metal and the nanowire materials of interest. As an example, the phase diagram for silicon and gold is shown in the previous section. If the system is raised in temperature above the eutectic point ( $\sim 360^\circ\text{C}$ ), a molten alloy is formed. Since the sticking coefficient of a liquid is very high, a preferential deposition of silicon at this location can occur at higher deposition temperatures where the sticking coefficient of silicon on silicon can be reduced. As the alloy is supersaturated with silicon, the solid silicon drops out to form the next layer of nanowires, and the molten alloy is pushed to the top of the wire.



**Figure 98.** Gold droplets form an alloy with silicon. The alloy has a eutectic point near  $360^\circ\text{C}$ , above which it is molten.

In the VLS technique, the location of the nanowires can be controlled by controlling the location of the metal droplet. Reported here are the results of

investigating various patterns etched through silicon dioxide to determine if a preferential location for the metal droplets could be found within the pattern.

## **5.2 Experiment**

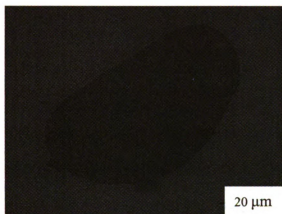
A series of experiments were devised to investigate the effects of the control over the location and size of gold particles on silicon (111) substrates. It is well known that the deposition of gold onto substrates containing defects can result in a “decoration” of those defects by gold particles. This is caused by the reduction in free energy when the droplets as described in Figure 3 are located at a step edge on the substrate. At such locations a larger portion of the total droplet surface is governed by  $\gamma_{fs}$ . Therefore, it is expected that the gold particles will preferentially reside at these step edges or at the corners of step edges where the free energy is even further reduced.

In these experiments, the silicon substrates were first oxidized. The oxide layers were then patterned through standard lithography processes, as described in the “Buffered Etches” section. Five different shapes were patterned through the oxide layer. Gold was then either deposited on the substrate at room temperature, followed by an annealing step, or it was deposited onto the substrate at a high temperature of deposition. Various temperatures were investigated with results shown below.

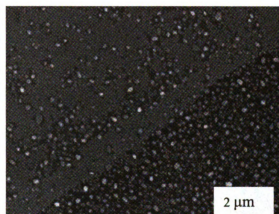
## **5.3 Gold Deposited at Room Temperature**

An oxide layer was first grown to a thickness of 100 nanometers, and then patterned. A gold layer was then sputter deposited at room temperature to a thickness of 10.5 nanometers, and the wafer was subsequently annealed to the temperature indicated.

Figure 99 through Figure 104 show the resulting SEM images. Due to the surface tensions, Au will ball up to form surface droplets as shown in the figures. The diameter of the Au ball in this experiment varied from  $0.1\text{ }\mu\text{m}$  to  $0.5\text{ }\mu\text{m}$ . Based on the phase diagram, the balls were an alloy of gold and silicon when annealed to these temperatures. Figures 99, 103, and 104 show the gold preferentially coalesces at and near the holes through the oxide layer.



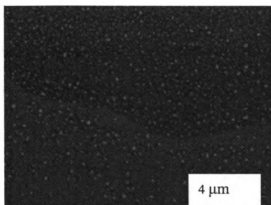
**Figure 99.** The darker location is Si and the lighter locations are  $\text{SiO}_2$ . The scale bar is  $20\text{ }\mu\text{m}$ .



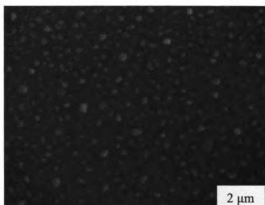
**Figure 100.** The area identified in this image is near the edge of the half-circle pattern. The scale bar is  $2\text{ }\mu\text{m}$ .

Figure 99 through Figure 104 show the silicon wafer with  $10.5\text{ nm}$  of Au followed by a  $550^\circ\text{C}$  annealing for 5 minutes. The darker regions in these images correspond to the silicon surfaces, and the lighter regions to the  $\text{SiO}_2$  films. The density of Au balls is seen to be higher on Si than the  $\text{SiO}_2$  locations.

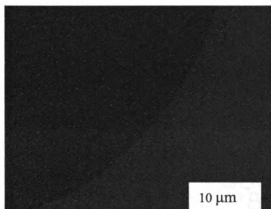




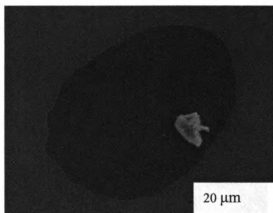
**Figure 101.** The image is near the edge of the half-circle pattern. The darker location is Si and the lighter locations are SiO<sub>2</sub>. The scale bar is 4 μm.



**Figure 102.** The image is inside the pattern. The background is Si, and the white dots are Au. The scale bar is 2 μm.



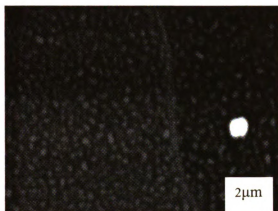
**Figure 103.** The dark part is Si and the light ball is Au. This area is inside the pattern. The scale bar is 10 μm.



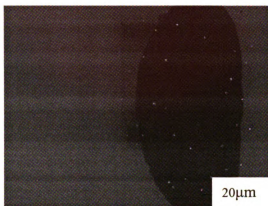
**Figure 104.** This is a half-circle pattern. The white chunk is silicon. The scale bar is 20 μm.

Figure 105 through Figure 107 are SEM images of the silicon wafer with a deposited layer of Au at room temperature. The thickness of the Au layer was 10.5 nanometers, and the silicon wafer was annealed at 620° C for 5 minutes. At this annealing temperature, larger Au balls (about 500 nm diameter) were observed at silicon locations

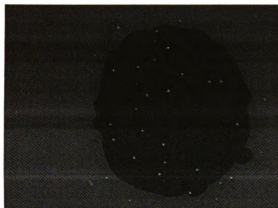
on the substrates, which suggests a larger surface diffusion occurring on the silicon dioxide surface. The average diameter of the Au particles was estimated from these images to be 100 nm.



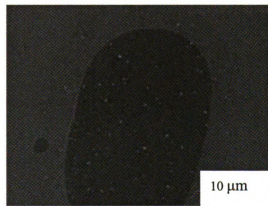
**Figure 105.** The average diameter of the Au balls was 100 nm. The scale bar is 2  $\mu\text{m}$ .



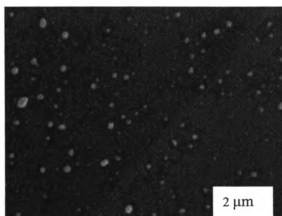
**Figure 106.** This is a half-circle pattern. The scale bar is 20  $\mu\text{m}$ .



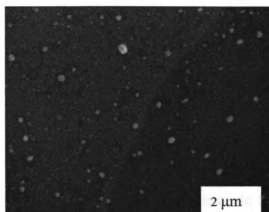
**Figure 107.** The darker location is Si and the lighter locations are  $\text{SiO}_2$ .



**Figure 108.** 10.5 nm of sputter deposited Au followed by an annealing at 700° C for 5 mins. The scale bar is 10  $\mu\text{m}$ .

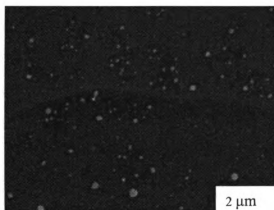


**Figure 109.** The image is near the edge of the half-circle pattern. The scale bar is 2  $\mu\text{m}$ .

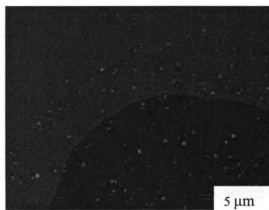


**Figure 110.** The image is near the edge of the half-circle pattern. The scale bar is 2  $\mu\text{m}$ .

Figure 108 through Figure 112 are SEM images of the silicon wafer with a 10.5 nm thick sputter deposited layer of Au at room temperature. The silicon wafer was then annealed at 700° C for 5 minutes. Some large Au balls of about 500 nm diameter were seen at silicon locations. This suggests a higher sticking coefficient in the silicon regions and a high surface diffusion of Au. The average diameter of the Au particles v<sup>2</sup>  $\mu\text{m}$  than 100 nanometers.



**Figure 111.** The image is near the edge of the pattern. The dark location is Si and white dots are Au. The scale bar is 2  $\mu\text{m}$ .

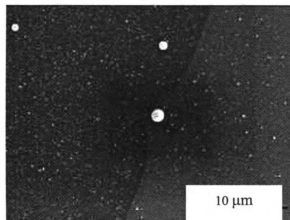


**Figure 112.** The dark location is Si. The scale bar is 5  $\mu\text{m}$ .

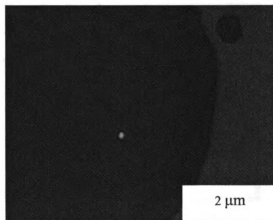
From Figure 99 through Figure 112, three different annealing temperatures were investigated in order to determine the morphological influence of temperature on gold balls. Larger Au balls were observed in the silicon regions of the substrates for higher annealing temperatures; however, in all cases, the gold was evenly distributed throughout the silicon regions and did not preferentially collect at the Si-SiO<sub>2</sub> edges. This could be ascribed to the relatively thin oxide layers used, and the annealing temperatures investigated.

#### 5.4 Gold Deposited at High Temperatures

From Figure 113 through Figure 122, the SiO<sub>2</sub> layer on the silicon wafer was first patterned and subsequently placed inside a tube furnace system. The temperature was then raised to 700° C, and Au was deposited by pulsed laser deposition (PLD) for 1 minute. The substrate was then maintained at 700° C for 5 minutes before reducing power to the tube furnace.

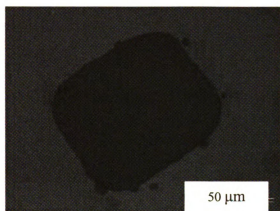


**Figure 113.** The Au ball was observed to be in the gap as a bridge. The scale bar is 10 μm.

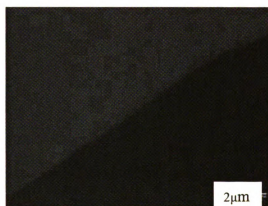


**Figure 114.** The area in this image is in the edge of pattern. The scale bar is 2 μm.

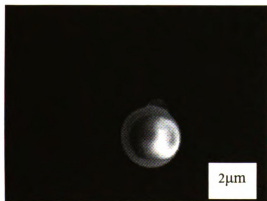
Similarly, it was found that gold did not preferentially locate at the silicon – silicon dioxide edges; rather, it was distributed evenly on the surface. It appears that silicon dioxide layers did show pits and holes through the oxide at locations where it was not patterned. Gold preferentially deposited at silicon locations, and not on the oxide layer. We are, therefore, in the process of investigating thicker oxide films both to increase the step height between Si and SiO<sub>2</sub> and to avoid pinholes through the oxide films and the degradation of the oxide films at higher temperatures.



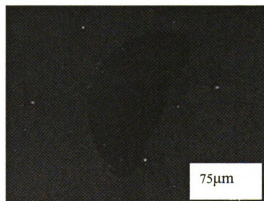
**Figure 115.** The SEM image shows the square pattern. The scale bar is 50 μm.



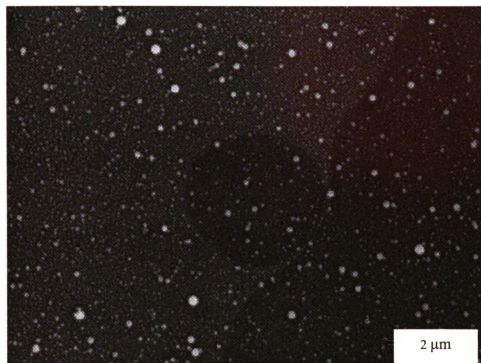
**Figure 116.** The SEM image shows the edge of pattern. The scale bar is 2 μm.



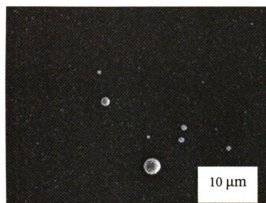
**Figure 117.** The Au ball was found outside the pattern. The scale bar is 2 μm.



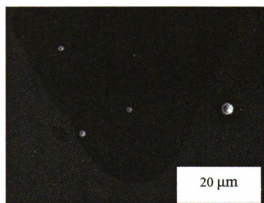
**Figure 118.** The SEM image shows gold ball scattered outside the pattern. The scale bar is 75 μm.



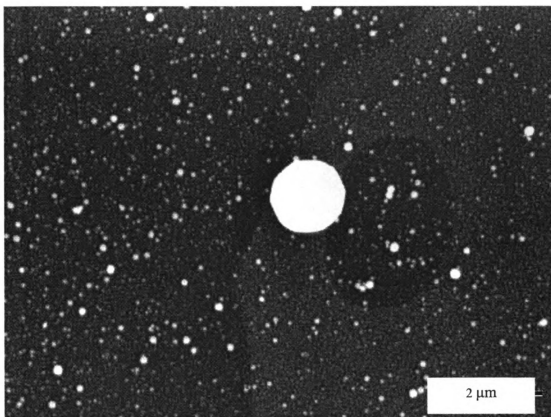
**Figure 119.** This gap is not big enough to have a big Au ball produced in the gap. The scale bar is 2  $\mu\text{m}$ .



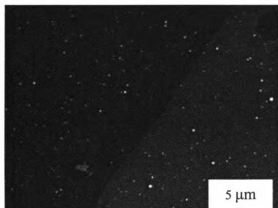
**Figure 120.** The Au balls are inside the pattern. The scale bar is 10  $\mu\text{m}$ .



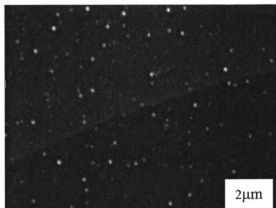
**Figure 121.** The image is near the edge of the pattern. The scale bar is 20  $\mu\text{m}$ .



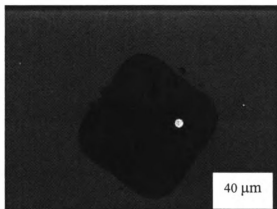
**Figure 122.** The temperature was raised to 700° C and Au was deposited by pulsed laser deposition (PLD) for 1 minute. The substrate was then maintained at 700° C for 5 minutes before reducing power to the tube furnace. The shape of the Au ball looks like a bridge. The scale bar is 2  $\mu\text{m}$ .



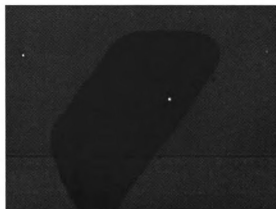
**Figure 123.** The image is taken near the edge of the pattern. The scale bar is 5  $\mu\text{m}$ .



**Figure 124.** The image is taken near the edge of the pattern. The scale bar is 2  $\mu\text{m}$ .



**Figure 125.** The temperature was raised to 700° C and Au was deposited by pulsed laser deposition (PLD) for 1 minute and reducing power immediately. The scale bar is 40 μm.

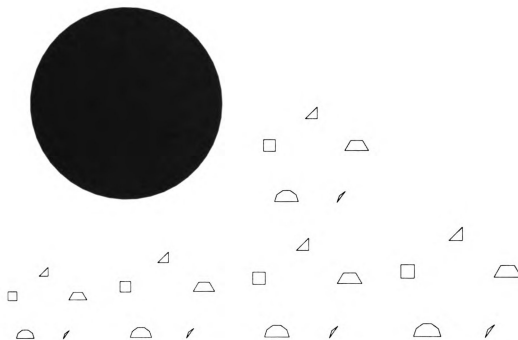


**Figure 126.** The temperature was raised to 700° C and Au was deposited by pulsed laser deposition (PLD) for 1 minute and reducing power immediately.

Figure 125 and Figure 126 were obtained using laser ablation of gold for 1 minute. After this deposition, the temperature was rapidly decreased. These figures show that the number of large Au balls has decreased relative to the experiments where the substrate was maintained at 700° C for 5 minutes after the deposition.



## ***Mask design***



**Figure 127.** The mask designed for patterning the SiO<sub>2</sub> layer using a positive photoresist (Shipley 1813).

We have 110 sets in this mask design (Figure 127). The resolution of this mask is 5080 dpi. The mask was first drawn in AutoSketch, and then we converted it to a pdf file with 5080 dpi. The file was sent to a local company, Info Tech, for print.

## **5.5 Conclusion**

Initial investigations aiming at controlling the location and size of the gold metal catalyst particles on the surface of silicon have shown a preferred deposition of Au onto silicon locations, particularly for the depositions of Au on the substrates at higher

temperatures. The expected preferential deposition of Au at the edges between silicon and silicon dioxide was not observed under the conditions studied. Further studies are under way to investigate thicker oxide films and a broader range of deposition temperatures.

## **Chapter 6 Germanium Oxide Nanobridge**

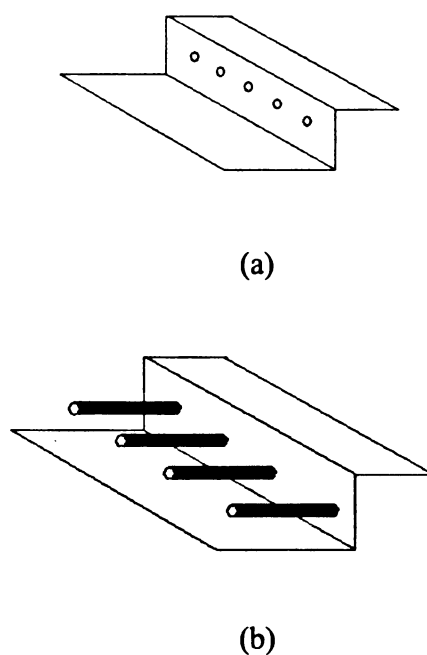
This chapter aims at investigating the lateral growth of high density metal-catalyzed germanium oxide nanowires and the bridging of nanowires between two vertical silicon sidewalls, which can be developed as electrodes used for an electronic device. A variety of methods to produce metal-catalyzed nanowires were used. After the catalytic metal was placed on the vertical silicon surfaces, a thermal annealing process was initiated to grow nanowires and to eventually form 'nanobridges'. Nanobridges have certain unique properties, such as a high surface-to-volume ratio and the capability of connecting two electrodes, which allow them to be effectively used as nanosensors.

### **6.1 Introduction**

Possessing a high surface-to-volume ratio renders free-standing nanostructures very sensitive to the charged species absorbed on their surfaces. More specifically, this property makes them especially attractive for sensor applications. The lateral growth of GaAs nanowires by metalorganic vapour phase epitaxy (MOVPE) on a GaAs substrate has been reported [67,68]. The lateral growth of silicon nanowires between two silicon surfaces through chemical vapour deposition (CVD) also has been reported [69]. Moreover, using one-dimensional nanostructures to synthesize semiconducting oxides that have the feature of stability, and optical properties of interest has attracted much attention. This has led to the investigations of their potential applications in different fields, such as optoelectronics, being used as detecting tips for atomic force microscopy (AFM), and sensing. Germanium dioxide, as a promising material, has been extensively

studied regarding its optical and electronic properties, and the growth of germanium dioxide nanowires has been studied through different methods. Thermal annealing of germanium under the sub-atmosphere condition leads to the growth of densely distributed wires with diameters ranging from tens of nanometers to hundreds of nanometers, and their lengths are up to tens of microns on the substrate surface. In the previous chapter, the growth of germanium oxide nanowires has been discussed in detail. In this chapter, the focus is on the lateral growth of germanium dioxide nanowires. Using semiconductor nanowires, researchers have succeeded in demonstrating nanowire sensors for biological species [70]. In the current research, the underlying mechanism for nanowire sensors is a field effect [71]. Researchers have used a fluid flow method to assemble nanowires into parallel arrays and clusters, and electrical contacts were defined by e-beam lithography. The approach of connecting electrodes and nanowires one at a time cannot be used for manufacturing devices, although it is useful for understanding the characteristics of nanowires. Hence, the mass self-assembling technique is necessary to enable germanium oxide nanowires to bridge between electrodes.

In this chapter, the lateral growth of metal-catalyzed germanium oxide nanowires is reported, from one vertical Si plane to the other vertical plane. By using a large number of such 'nanobridges' in parallel, the desired high-surface area can be obtained in a small volume. Nanowires should grow laterally from one sidewall toward the opposing sidewall of the trench. The surface-to-volume ratio is key to the performance of nanosensors. Therefore, the distance between the two vertical surfaces plays an important role. In the example of this chapter, the distance between the two vertical surfaces ranges from 50 to 70  $\mu\text{m}$ .



**Figure 128.** Schematic diagrams of (a) metal catalyst and (b) lateral nanowire growth.

## 6.2 Experiment

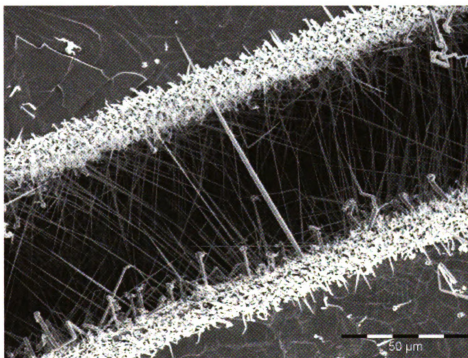
### Experiment #1:

A piece of germanium was placed on top of a silicon wafer. Another piece of silicon wafer with gold deposited ( $\sim 10$  nm thick) was put on top of the germanium and the stack was annealed to  $850^\circ\text{C}$ . It was then left at  $850^\circ\text{C}$  for 40 minutes with an Ar/H (95/5) flow of 200 sccm to reach 10 Torr. Then the Ar/H flow was stopped and room air was allowed to flow into the hot chamber for 1 minute to reach pressure 350 Torr. Then the pump was turned on, and the furnace was turned off in order to cool.

The experiment was conducted within a quartz tube (outer diameter, 90mm; length, 80 cm) heated by a horizontal tube furnace. The sample was put at the center of a quartz boat placed in the middle of the quartz tube, which was pumped down to about 30 mTorr.

## Result

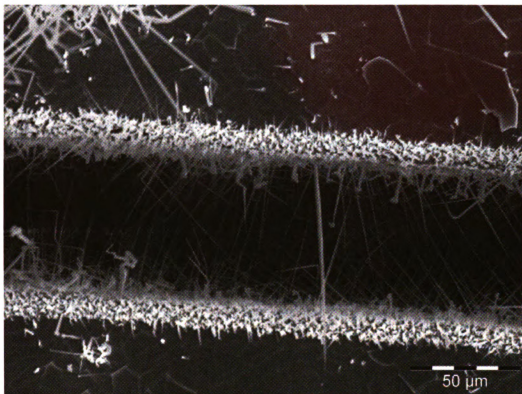
Photoresist was spun on the (110) silicon wafer and patterned, and a KOH etch was used to form trenches of various widths. Before removing the photoresist, a gold film was deposited to coat the inside of the trenches. The photoresist was then removed along with any gold layer on top of the photoresist and germanium oxide nanowires grown as described above. The SEM image in Figure 129 shows that the germanium oxide nanobridge grew across the 70  $\mu\text{m}$  trench.



**Figure 129.** The nanowires grew across the trench. The scale bar is 50  $\mu\text{m}$ .

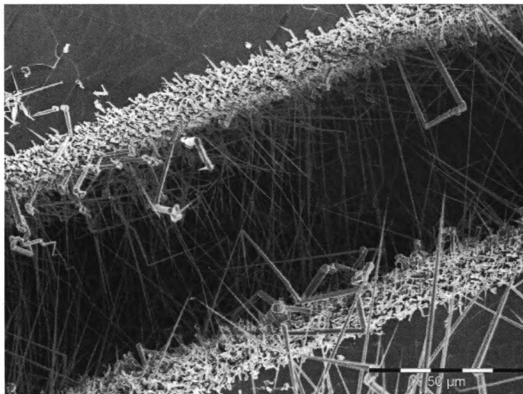
The gold was deposited on both sidewalls of trenches and the germanium oxide nanowires grew predominantly only where the gold was deposited. From the image, the nanowires grew in preferred directions that were almost perpendicular to each other, and most nanowires were very straight. There were also some whiskers with larger diameters

and shorter lengths growing on the sidewalls. The diameter of the whiskers was about 2  $\mu\text{m}$ .



**Figure 130.** Nanowires grew across the 70  $\mu\text{m}$  wide trench. The scale bar is 50  $\mu\text{m}$

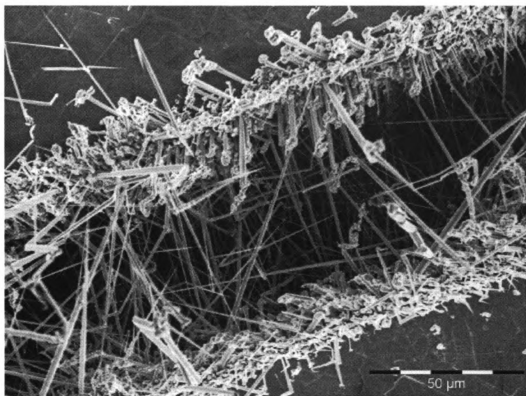
Figure 129 and Figure 130 show the SEM images of germanium oxide nanowires growing across the trench 70  $\mu\text{m}$  in width to form nanobridges. The gold was deposited on the sidewall of the silicon wafer trench only. Therefore, the growth of nanowires mainly took place inside the trench where gold was deposited, and little to no growth can be found outside of the trenches.



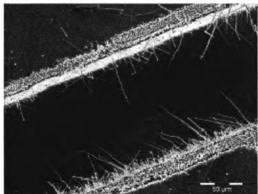
**Figure 131.** Dense nanowires grew across the trench. The scale bar is 50  $\mu\text{m}$ .

Figure 131 shows the SEM image of a high density of germanium oxide nanowires growing across the silicon wafer trench. The shorter nanowires, which did not grow across the trench, show bright dots at the tip. Most nanowires were straight and long enough to bridge the 70  $\mu\text{m}$  trench. Several larger diameter whiskers were found along the sidewall and exhibit more kinking along the length of the wire. These larger whiskers can be more clearly seen in Figure 132 where it is also easily observed that many wires are also at an angle up and out of the trench.

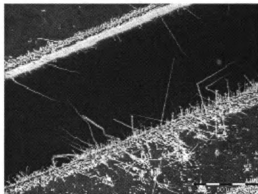




**Figure 132.** The whiskers with large diameters grew on the side wall. The scale bar is 50  $\mu\text{m}$ .

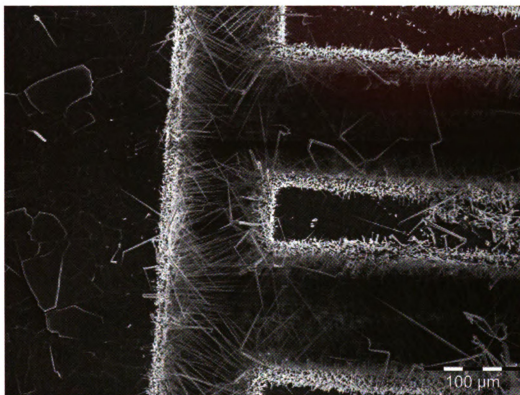


**Figure 133.** The scale bar is 50  $\mu\text{m}$ .



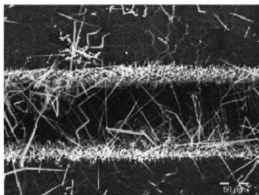
**Figure 134.** The scale bar is 50  $\mu\text{m}$ .

Figure 133 and Figure 134 show the SEM images of germanium oxide nanowires growing in a wider trench, which was 85  $\mu\text{m}$  in width. The density of nanowires inside wider trench had lower density than that in narrower trench.

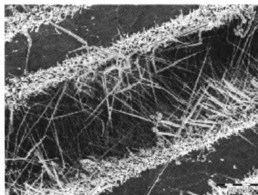


**Figure 135.** The nanowires grew in the region with different widths.

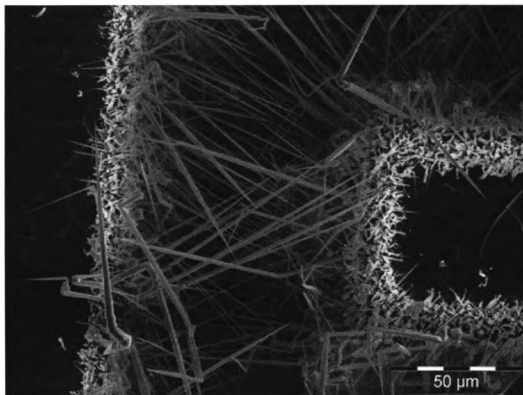
The SEM image in Figure 135 shows that the nanowires grew inside trenches of different widths. In this region, nanowires growing in the narrower trench tended to exhibit higher density and longer length. This phenomenon was also observed at the corner of the center island where the nanowires had higher density and longer length in the narrow trench than in the wider trench. The widths of these trenches were 80 and 115  $\mu\text{m}$ , respectively.



**Figure 136.** Nanowires inside the trench. The scale bar is 50 μm.



**Figure 137.** Nanowires inside the trench. The scale bar is 50 μm.



**Figure 138.** Nanowires grew along the corner.

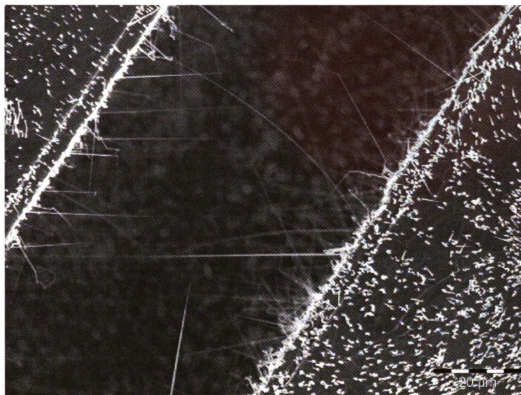
Figure 136 and Figure 137 show the SEM images of nanowires growing inside the trench. The SEM image in Figure 136 shows that the whiskers with the larger diameters grew in the upper portion of the trench (near the surface of the substrate). The SEM

image in Figure 137 illustrates the kinked whiskers with larger diameters emerged in the upper part of the trench while in the bottom part, nanowires with smaller diameters were observed. Figure 138 shows the SEM image of the germanium oxide nanobridge intersecting with the trench.

#### Experiment #2:

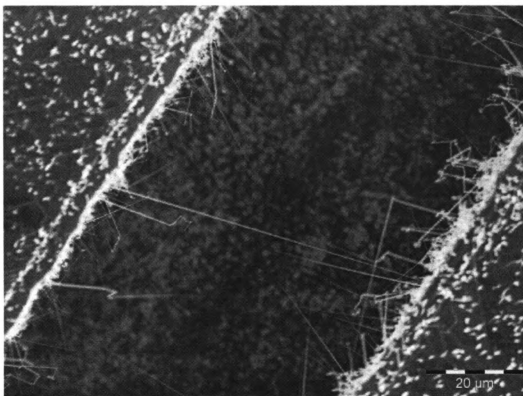
Gold nanoparticles were applied on the silicon wafer before the experiment. The germanium was placed on top of a silicon wafer and another piece of silicon wafer with gold nanoparticle (20 nm) was placed on top of the germanium, and the stack of samples was subsequently annealed to 850° C. Then the system left at 850° C for 40 minutes with Ar/H (95/5) flow at 200 sccm to reach 10 Torr. The Ar/H flow was then stopped and room air was allowed to flow into the hot chamber for 1 minute to reach pressure of 350 Torr. The vacuum pump was then turned on, and the furnace turned off to cool the chamber.

## Result



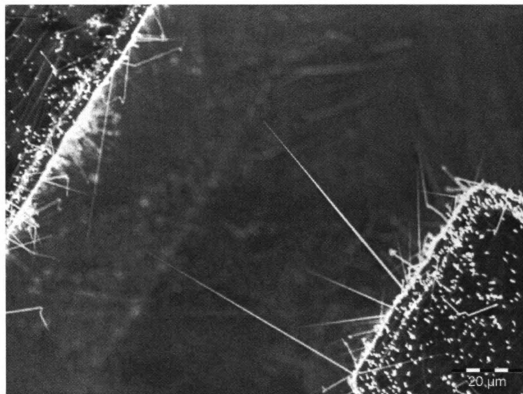
**Figure 139.** The growth of nanowires in the trench.

The SEM image in Figure 139 shows the nanowires grew on the sidewall of the trench. The scale bar is 20  $\mu\text{m}$ . The gold nanoparticles (20 nm) were applied to the top of the silicon surface before the experiment.



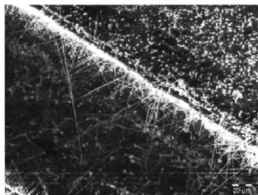
**Figure 140.** The SEM image shows nanowires grew across the trench.

Figure 140 is the SEM image of germanium oxide nanowires growing inside the trench. The scale bar is 20  $\mu\text{m}$ . A few germanium oxide nanowires made it across the trench. After the sample was exposed to the air for 1 minutes, the nanowires grew. Compared with the 10 nm gold deposited on the surface, the density of germanium oxide nanowires was lower in certain areas of the silicon wafer.

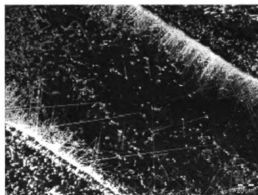


**Figure 141.** The nanowires grew across the 80 wide trench.

The SEM image in Figure 141 shows the growth of nanowires from the center island (lower right of the image) toward the sidewall of the trench. The nanowires tapered off to a point.

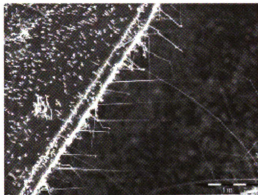


**Figure 142.** The scale bar is 20 μm.

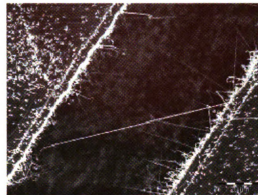


**Figure 143.** The scale bar is 20 μm.

From Figure 142 through Figure 145, it appears that only a few nanowires crossed the trench. Most nanowires were shorter than 20  $\mu\text{m}$  in length.



**Figure 144.** The growth of nanowires in the trench.



**Figure 145.** The scale bar is 20  $\mu\text{m}$ .

## Discussion

The nanowires grown from the gold nanoparticles (20 nm) had lower density compared with those grown from the gold layer with 10 nm thickness. Diameters of the nanowires appears much more uniform by using the gold nanoparticles, and the larger whiskers near the surface of the trench sidewalls were not observed when the gold nanoparticles were used. A high density of nanowires can be seen at the surfaces of the trench sidewalls, with a few nanowires exhibiting much higher growth rates and extending across the trench.

## Experiment #3:

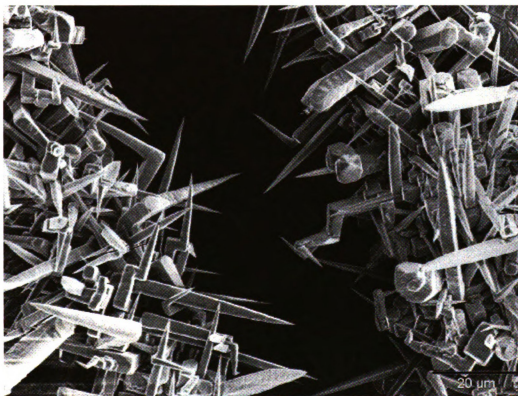
A layer of gold was deposited on the silicon wafer at high temperature. The piece of germanium was put on top of the silicon wafer and subsequently annealed to 850° C. After reaching 850° C, room air was allowed to flow into hot chamber to reach pressure



400 Torr. Then the KrF laser was used at 500 mJ, 5 Hz for 90 seconds to ablate the gold target. The system was then left at 850° C for 8 minutes with Ar/H (95/5) flow at 200 sccm. Then the pump was turned on, and the furnace was turned off to cool.

## Results

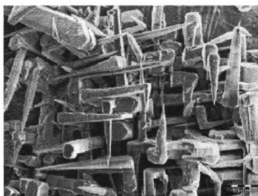
The SEM image in Figure 146 shows that the whiskers grew on the sidewall of the trench. Many whiskers show 90° bends along the length of the wire, suggesting a tetragonal crystal structure. The dimension of these whiskers was about 4  $\mu\text{m}$  in width.



**Figure 146.** In the SEM image of whiskers grew across the trench. The scale bar is 20  $\mu\text{m}$ .

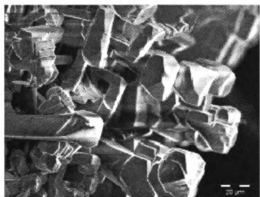


**Figure 147.** The scale bar is 10  $\mu\text{m}$ .

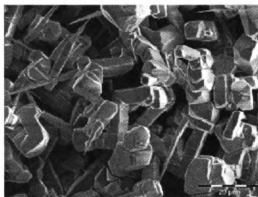


**Figure 148.** The scale bar is 10  $\mu\text{m}$ .

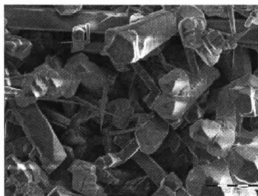
Figure 147 and Figure 148 are the SEM images of germanium oxide whiskers growing on top of the silicon wafer. Half of the whiskers in the images tapered off along the crystal structure to a point while the remainder abruptly terminate in their growth.



**Figure 149.** The scale bar is 20  $\mu\text{m}$ .



**Figure 150.** The scale bar is 20  $\mu\text{m}$ .



**Figure 151.** The scale bar is 20  $\mu\text{m}$ .



**Figure 152.** The scale bar is 20  $\mu\text{m}$ .

Figure 149 through Figure 152 show the SEM images of germanium oxide whiskers growing on top of the silicon surface. Many of the whiskers in these images show sharp  $90^\circ$  corners on one or more of their edges in cross-section.

### **Discussion**

The germanium oxide whiskers grown from the laser ablated gold target had larger diameters than previous results and appeared with many  $90^\circ$  edges. The size of these wires make such observations easier to identify. Also seen, are approximately half of the wires tapering to a point, with the others abruptly terminating growth. For the later wires, the geometry of the cross sections can be clearly seen.

### **6.3 Conclusion**

In another experiment of growing germanium oxide nanowires on top of the pre-pattern silicon wafer, the control of the growth of nanowires was recognized to be important. By placing gold on the sidewalls of the trench, the lateral growth of germanium oxide nanowires produced the first germanium oxide nanobridge, which is deemed as a significant breakthrough in the nanowire research. The nanobridge can be formed with different lengths and diameters by using different methods to place gold on the sidewall and controlling the time exposed to the air.

## Chapter 7 Conclusion

In this study, the tube furnace system allowed the experiments to take place in a wide range of operating environments: the pressure regions could vary from  $10^{-3}$  to 500 Torr, and the temperature range could reach as high as  $1000^{\circ}\text{C}$ . This wide operating range allowed us to investigate a variety of materials, such as gallium arsenide, indium antimonide,  $\text{Sr}_8\text{Ga}_{16}\text{Ge}_{30}$ , and germanium, and thus to speculate, for future studies on the conditions under which nanobridges made from these materials can be produced.

In the gallium arsenide nanowires growth experiment, the nanowires only emerged when an additional gold layer was deposited on top of the piece of gallium arsenide. The EDS analysis showed that the nanowires were actually gallium oxide nanowires. To our knowledge, this is the first observation of gallium oxide nanowires that have been synthesized through the simple thermal annealing of gold deposited on GaAs. The absence of gold balls at the tips of the nanowires suggests the growth mechanism may not be VLS-based. Instead, the solid-liquid-solid mechanism might be more appropriate to explain the growth mechanism. Since the Pauling electronegativity of Au is higher than that of the elements of Group V, arsenic is absent and Au acts as an oxidizing agent and displaces the less electronegative elements of Group V by combining the highly electropositive Group III metals. In addition, gold plays a major role in determining the quantity of gallium oxide nanowires. The gallium arsenide without the gold layer showed no trace of nanowire growth. The diameters of gallium oxide nanowires were affected by varying the growth temperature. The experiment at lower temperatures produced nanowires with larger diameters. From these results, two factors are identified

to affect the growth of gallium oxide nanowires: the thickness of gold and the temperature.

In the  $\text{Sr}_8\text{Ga}_{16}\text{Ge}_{30}$  nanowire growth experiment, we produced the nanowires from  $\text{Sr}_8\text{Ga}_{16}\text{Ge}_{30}$  by simply mixing it with Au nanoparticles and using a local vapor confinement technique. No growth of nanowires took place without the presence of gold nanoparticles. In the images shown in chapter 5, the gold balls appeared at the tips, which was an indication that the growth mechanism was the well-known vapor-liquid-solid mechanism. From the TEM analysis, the nanowires were found to be gallium oxide nanowires, and, strontium and germanium were not present in the final component of these nanowires. In addition to gold, the second factor influencing the growth of nanowires from  $\text{Sr}_8\text{Ga}_{16}\text{Ge}_{30}$  was vapor pressure. After a piece of quartz plate was added on top of the sample, the quantity of nanowires dramatically increased. Nanowires thus grew after a piece of quartz plate was added. Most importantly, these newly formed nanowires had uniform diameters.

In the experiment of growing nanowires from germanium, the germanium nanowires were grown using the gold mediated VLS growth mechanism. After a series of chemical reactions, germanium oxide nanowires were produced below its melting point. There are two critical factors that affected the growth of nanowires. First, gold was an important factor. Our experiment showed the absence of gold resulted in no growth of nanowires; however, the presence of gold at the tip of wires, as verified by the EDS analysis, suggested the VLS growth mechanism. Second, oxygen was also critical in the nanowires growth process: No growth will occur if oxygen is not involved in the

system. Additionally, the size of nanowires was determined by the time they were exposed to air at high temperature.

In another experiment of growing germanium oxide nanowires on top of the etched silicon wafer, control of the growth of nanowires was important. By placing gold on the sidewall of the trench, the lateral growth of germanium oxide nanowires produced the first germanium oxide nanobridge: a breakthrough in our nanowire research. By using different methods to place gold on the sidewalls and controlling the time exposed to the air nanobridge can be formed with different lengths and diameters.

In the nanoscale world, the study of materials involves the selection of appropriate mechanisms, as well as the considerations of the interference from different variables. Even a small change in the experiment condition will influence the result of the growth to some degree.

## **Chapter 8 Scanning Electron Microscope**

Initially commercialized in 1965, the scanning electron microscope (SEM) has been identified as an exceedingly valuable instrument in terms of scientific contributions. In general, the popularity and advantages of SEM can be demonstrated in various ways. For instance, SEM has a large depth of field, in which the sample can be precisely focused at one time. Also, its magnification is up to four hundred times greater than that of a light microscope.

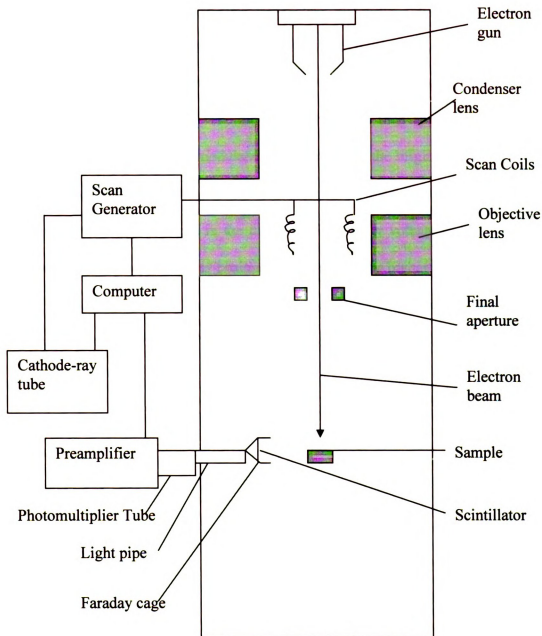
Currently the resulting image quality derived from the SEM can be much greater due to its depth of field. The resolution of SEM is comparatively higher than that of a light microscope, the feature that enables the sample to be investigated at a higher magnification than what is possible while using a light microscope. Specifically, this instrument has a wide range of magnification, normally between about 10x and 100,000x.

### **Theory of SEM Operation**

A basic diagram of an SEM is shown in Figure 1. The electron gun, which is located at the upper part of the column, produces an electron beam. The top portion is the electron source, a hair-thin and V-shaped filament of fine tungsten wire. It is being heated by passing a high voltage and low amperage current. Electrons boiling off it are divided along the column as a tightly coherent beam, aimed directly at the specimen. The beam accrues through the anode and is condensed by the condenser lens, followed by the step of being focused as a very finely-tuned point on the specimen via the objective lens.



The cohesiveness and direction of the beam is controlled by electromagnetic lenses.



**Figure 1.** Schematic of an SEM [72]

The electron beam is deflected back and forth by a magnetic field which is produced by coils. The coils are located within the objective lens, and are energized by the scan generator. This varying voltage is produced by the scan generator.

When a beam of electrons strike on an object, it affects other electrons to be loosely attached to the object itself. These secondary electrons, primarily collected by the detector near the specimen, scatter in directions determined by the angle of incidence of the beam, and by the surface topography of the specimen. The signals are converted to a voltage, and then amplified. The amplified voltage is then applied to the grid of the cathode-ray tube (CRT) and modulates the intensity of the brightness of the spot on the CRT. This modulation is meant to demonstrate that the brighter spot on the CRT is produced by a larger voltage in the detector. This larger voltage is created by a larger number of secondary electrons positioned comparatively higher on the sample surface. Then, the SEM image is composed of thousands of spots characteristic of varying intensity on the face of a CRT that corresponds to the topography of the sample [72].

## **Everhart-Thornley Detector**

The Everhart-Thornley detector is a major component of the SEM. In short, the innovative Everhart-Thornley detector has made the formation of images using the secondary electron signal possible. Moreover, the corresponding result is higher in terms of potential resolution when using this signal.

The frontal facet of the detector is mainly made of a structure called Faraday cage or collector screen. By definition, since the Faraday cage either takes the form of a wire-mesh or a metal ring, it is usually maintained at a positive potential on the order of a few hundred volts, which is intended to efficiently collect nearly all of the secondary electrons emitted from the sample. The scintillator placed at the end of the Faraday cage has a thin conductor coating so as to be maintained at a higher positive potential of several kilovolts. If the secondary electrons are inside the Faraday cage, they will speed up by the force of highly positive electrical charge applied to a scintillator acting as a collector. When the secondary electrons hit the scintillator, light is generated thereafter and is directed towards the photomultiplier through the light pipe. Then the photomultiplier outputs a signal proportional to the number of secondary electrons collected.

Photons which enter the photomultiplier tube collide with the first electrode, inducing it to emit electrons. Then inside the tube, the electrons leap back and forth among a series of charged plates, and the number of electrons is increased in a cascading way, which eventually creates a gain of  $10^6$  electrons with each bounce. Subsequently, the output voltage of the photomultiplier is amplified to a larger degree by the preamplifier, whose output voltage finally modulates the intensity of the spot on the CRT.

There is one factor influencing the output signal from the electrons: the position of the scintillator. In normal situation, it is located line-of-sight with the sample. Due to this variable, the backscattered electrons that regularly are too active to be deflected to a large degree by a 200 V potential will also output a signal in the detector, even under the condition that a negative potential is applied to the Faraday cage. In this situation, we term it as a pure backscattered electron detector. By adjusting the cage potential, the tweaking of the topographic contrast given by the detector is made possible.

Typically, the Everhart-Thornley detector can detect most of the secondary electrons that depart from the surface of the specimen since these electrons are low in energy, and can be deflected simply through angles of extremely large size. Moreover, the detector can identify the backscattered electrons, which are openly moving toward the scintillator. Due to the high energy carried, however, the backscattered electrons are not easily deflected.

The Faraday cage is a required tool for shielding the electron beam from the 12,000-V positive electrical charge on the scintillator. The absence of the cage will cause the charge to deflect the electron beam. Nonetheless, since the action of the 12,000-V force field is limited by the Faraday cage that is external to this field, the beam of electrons is impacted merely by the 300-V force field of the Faraday cage itself [72].

The main function of scintillator is to convert the secondary and the backscattered electrons into a burst of light.

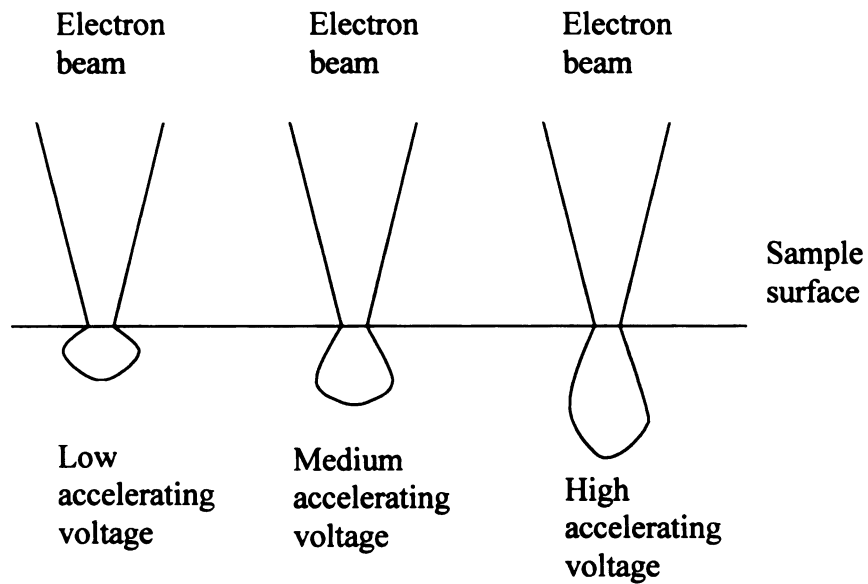
## **The Display Output**

The display output produces the image in the form of a television-type picture on a CRT and the images from the SEM are produced on the CRT. The CRT beam is not static. Rather, it swings back and forth across the face of the tube and its swing is synchronized with that of the electron beam in the column. A SEM usually has two types CRTs, one of which is for recording while the other is for viewing. The viewing CRTs exhibit a delay of approximately several seconds after the scan moves across the screen. As the image persists for a while, it is easy to be observed. However, in usual cases, the viewing CRT is exceptionally coarse-grained and with poor resolution. With this consideration, the work of photography is often achieved via a recording CRT that has a superior grain as well as the higher resolution. A camera is mounted in front of the CRT, and the image is recorded line by line. [72].

## **Specimen-Beam interactions**

Specimen interaction is what makes Electron Microscopy possible. When a beam of electrons hits on an object, it knocks other atoms loose from the object itself. The interactions generate diverse secondary products, such as electrons of different energy, and x-rays. The main purpose of these secondary products is to produce the images of the sample as well as to collect additional data from the sample. That information can use to form the secondary electrons image, backscattered electrons images and EDS analysis.

When the electron beam arrives to the surface of the sample, some of the electrons keep moving into the sample. The electrons which move inside the sample might be interacting with the sample atoms. The interaction between electron and sample atoms would give the sample atoms energy to scatter. At the same time, the electrons energy would lose because the energy is used for scattering the sample atoms. And that also changes the direction of the electron movement. Because of many interactions, the atoms might gradually lose energy. The interaction is a scattering process where no sharply defined limits exist regarding the boundary of the scattering. A defined limit may be placed upon the incident electron energy left as well as on the region of the interaction specified. Thus the illustration would focus on the area where the interactions occur with most possibility. Typically, the interaction is identified as pear-shaped. However, from the samples observed, the volume, both in terms of the measurement of depth and width, of the interaction change directly with the accelerating voltage, as shown Figure 2, and inversely with the average atomic number of the sample.

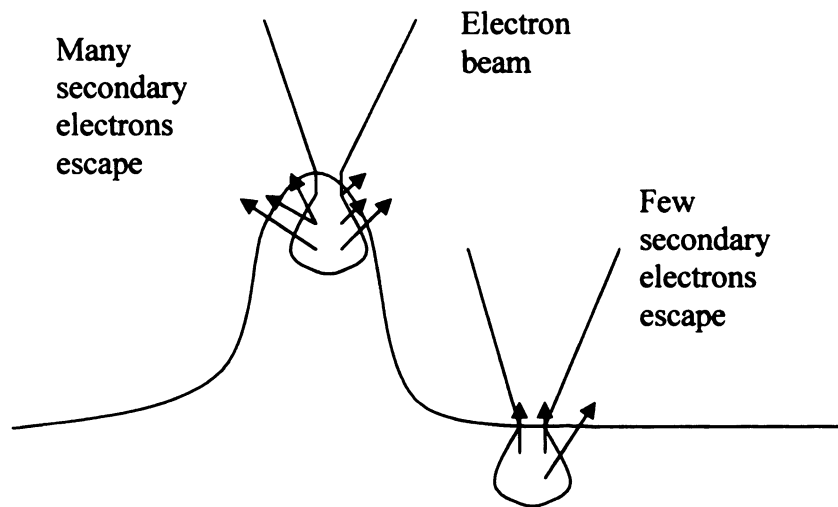


**Figure 2.** Interaction-volume variation with accelerating voltage.

The interactions between incident electrons from the electron beam and the sample atoms are described to be both elastic and inelastic. Elastic interactions take place between incident electrons and the nucleus of atoms of the sample that are distinguished by a large-angle deflection of the incident electron. Meanwhile, the minor energy loss by the incident electron is also observed. On the other hand, inelastic interactions occur between the incident electrons and the orbital shell electrons of the atoms of the sample, which are characterized by a small-angle deflection of the incident electron [72].

### Secondary Electrons Produce the Standard SEM images

In scanning electron microscopy, an inelastic interaction is responsible for producing secondary electrons, which are mostly created by interactions between incident electrons and weakly bound conduction-band electrons in the atoms of the sample.



**Figure 3.** Secondary electrons escape, edge effects, and image production [72].

Because the average energy of secondary electrons is about 3 eV to 5 eV, which is evaluated as low energy, secondary electrons are thus attracted easily by the positive high voltage on the Faraday cage. This attraction can detect all secondary electron in all directions. From the standard image in the SEM, it could be observed that secondary electrons are the main components. The creation of Secondary electrons occurs in the entire region of the specimen-beam interaction. Nonetheless, due to their characteristically low energy, they are strongly absorbed by the sample while only those produced near the surface of the specimen can break out with the aid of the decreased path to the surface. There are, therefore, two factors influencing the contribution of



secondary electrons in the SEM image: the absorption and escape of secondary electrons. These factors can dictate whether secondary electrons are capable of producing a predominantly topographical image in the SEM. It is found that small projections on the sample surface occupy the areas with a shorter path length of the escape of secondary electrons than do the flat areas as shown in Figure 3. These protruding areas emerge brightly on the image. Since the escape of secondary electrons takes place with a small volume among the total amount of the specimen-beam interaction, the image of the secondary electron is able to provide the image of highest resolution [72].

### **X-ray Analysis**

During the specimen-beam interactions, a beam of electrons impinges on an object; it knocks other atoms loose from the object itself. The interactions generate diverse secondary products, such as electrons of different energy, and x-rays. That information can use to form the secondary electrons image, backscattered electrons images and EDS analysis. In terms of the origin, x-rays are produced from the whole area of the specimen-beam interaction, found as secondary electrons; back scattered electrons, and Auger electrons. Nonetheless, x-rays are photons, rather than electrons. Furthermore, they have a much lower probability of losing their energy due to inelastic scattering. X-rays are produced in the electron microscopes, such as SEM and TEM. Accessory attachments enable the detection and analysis of x-rays, which can be used to determine the presence, amount, and distribution of the elements in the sample. What renders x-ray analysis beneficial is that there is no need to destroy the sample. Moreover, it is complete on a spatial basis, which means that there is a comparison of composition available between one part and an adjacent part within a sample.

Unlike many analytical techniques, x-ray analysis is not as sensitive comparable to neutron activation, atomic absorption, and inductively coupled plasma spectroscopy, which have limits of detectability measured in parts per million or better. Typically, the value of concentration of a specific element that can be detected for an entire sample in an SEM is 0.08% by weight, while the counterpart for a thin section in the TEM is 0.004% [72].

It can be defined that x-rays originate from inelastic scattering as a vacancy existing in an inner orbital shell packed with an electron from a shell of higher energy. It is this difference of energy between the shells that is emitted in the form of an x-ray. The element of the energy and the wavelength of the x-ray created is the main attribute. Its energy and wavelength are related by the equation  $\lambda = 1.2398/E$ , where  $\lambda$  is the wavelength in nanometers, and E is the energy in keV. In fact, the actual energy of x-rays might change, ranging from 2 to 3 eV based on the Heisenberg Uncertainty Principle.

Each x-ray produced is given a name based on the name of the shell (K, L, M, N) where the vacancy was created as well as on the number of orbital shell jumps made by the electron that filled the vacancy. Essentially, an element often produces more than one type of x-ray because multiple beam electrons strike the sample with each producing a different type of interaction. Each type of x-ray is called a line. If there are sufficient x-rays of a given line, an x-ray line peak in the spectrum analyzed is created. Each x-ray line has a representative energy and wavelength, and those x-rays from a given shell are termed as a family, such as the K family line and the M family line.

In order to remove an electron from a given shell, the beam of electrons must have certain energy, called the critical excitation energy, especially under the condition that the

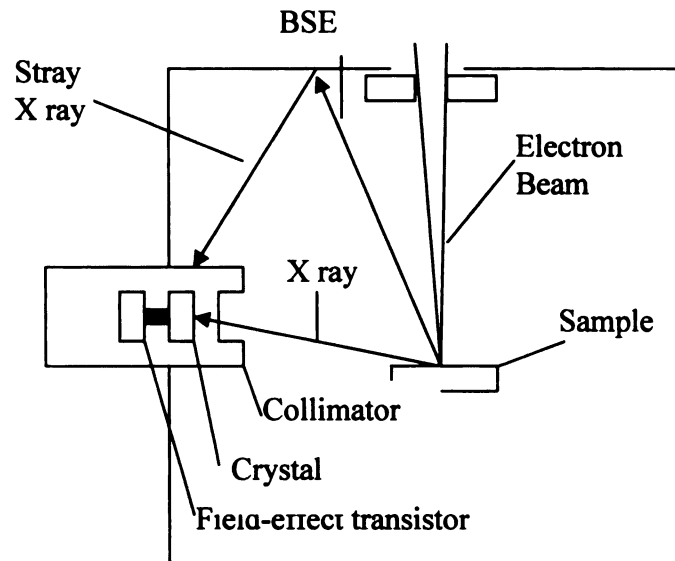
energy is not sufficient, resulting in no production of x-ray lines from that shell (or subshell). The energy of the beam is decided by the accelerating voltage of the electron microscope.

While conducting analyses of these specific elements, critical excitation energy differences between elements will lead to differences in the analytical spatial resolution. In thick samples the beam of electrons eventually will lose all of their energy, however in thin sections only a small percentage of the energy is lost. The differences between the analytical spatial resolutions of the various elements are more discernible in whole samples than they are in thin sections. Thus, the main differences in the analytical spatial resolution for different elements are primarily ascribed to the greater variation in energy of the beam electrons in thick samples.

Additionally, the production of characteristic x-rays is accompanied by the creation of noncharacteristic x-rays. These x-rays are collectively called background x-rays, continuum x-rays, or bremsstrahlung x-rays, which are produced following the deceleration of the beam electron when it enters the coulombic field between the nucleus and the tightly bound electrons. The energy of the background x-rays varies from zero to the energy of the electron beam. Usually, in a normal spectrum, characteristic x-ray peaks are placed on top of the background x-rays [72].

### Measuring the energy of x-rays

The elements in a sample can be determined by measuring the energy of the x-rays produced. The measurement of energy is called energy-dispersive spectroscopy (EDS). The EDS detector attaches to the column of an electron microscope. A number of components, including collimator, window, detector crystal, field-effect transistor, and a liquid nitrogen dewar, comprise the detector as shown in Figure 4 [72].



**Figure 4.** Schematic of an EDS detector attached to an SEM [72].

## **Peak Identification**

Peaks will be automatically specified during the spectrum accumulation. Nonetheless, to identify a more accurate peak, a number of things need to be considered,

1. Confirm that only these seven elements are excluded: H, He, Li, Fm, Md, No, Lr.
2. Ensure that the peak intensities match those of the displayed lines, such as  $K\alpha$  and  $K\beta$  pairs.
3. Select a small peak. In order to observe all the possible fits for the designated peak, it is necessary to check from Be to  $Z^+$ . If any of the displayed KLM lines approach the peak, then it is imperative to investigate the match and decide if it is a valid match.

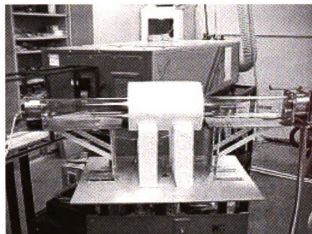
## **Discussion**

To avoid misidentifying by software in the use of EDS identification, the steps as mentioned earlier need to be followed to obtain the accurate data. Moreover, since the default line is not always the best, another necessary step is to determine if the best KLM line was used in the quantitative analysis calculation. Thus, it is necessary to select the line with highest counts that will be beneficial to acquire the quantitative analysis with more accuracy.

## Chapter 9 System set up

The photograph of the furnace system are shown in Figure 157. The outer diameter of the ceramic furnace is 10 inches while the inner diameter is 4 inches. The 48-inch long quartz tube housing the substrate and the target has a diameter of 85mm. The ends of the quartz tube are covered with the air-cooled end caps made of stainless steel. The vacuum was provided by the Tri-Scroll roughing pump (dry pump). A ConvecTorr vacuum gauge from Varian was used to measure the pressure inside the tube. A K-type thermocouple was placed between the quartz tube and the furnace, and was connected to a PID fuzzy logic-based controller. The sample and target were placed on top of a quartz boat that was placed inside the tube near the center of the furnace. The laser beam then passed into the furnace through the fused silica optical window, near the Ar gas inlet.

The following figures show the Autosketch drawings and the photographs for the stainless steel end caps that were designed and manufactured for the furnace system. The figures below show the drawings and the photographs of the optical-side endcap, which was designed to accommodate the transmission of laser into the furnace as well as the gas inlet. The second endcaps shows the gas outlet for a vacuum port to the chamber.



**Figure 157.** Quartz tube furnace system





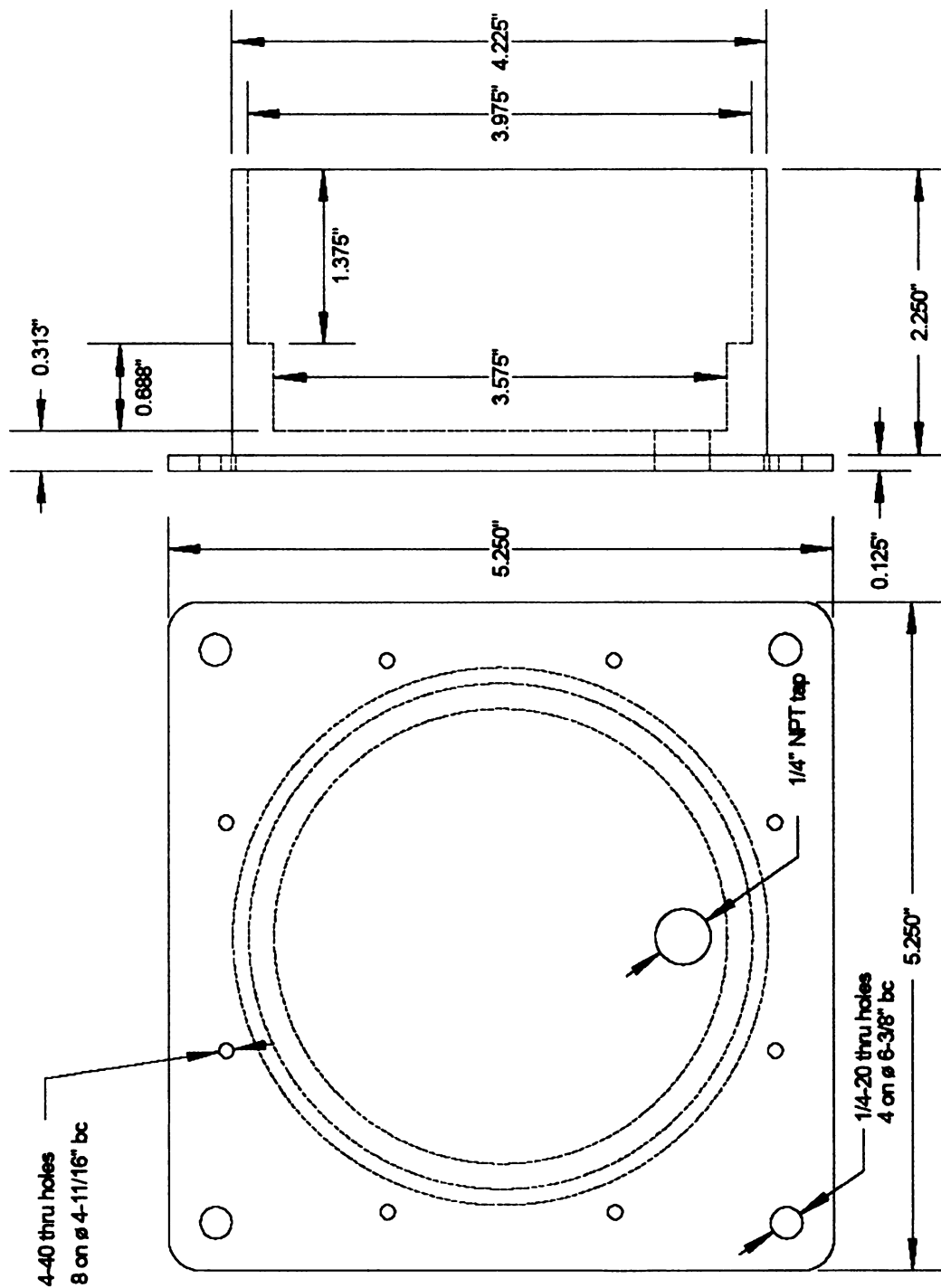


Figure 159. Autosketch of endcap

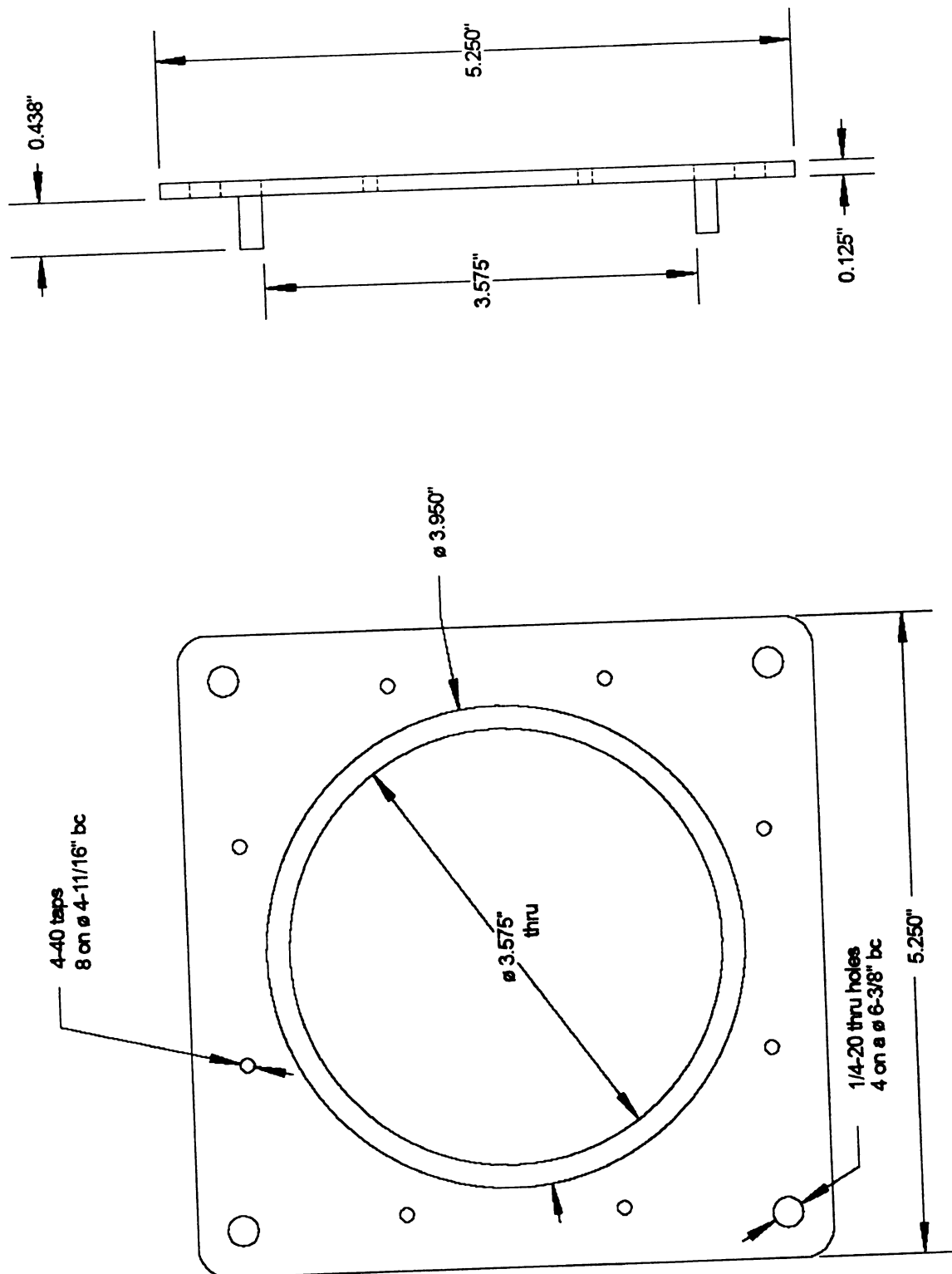
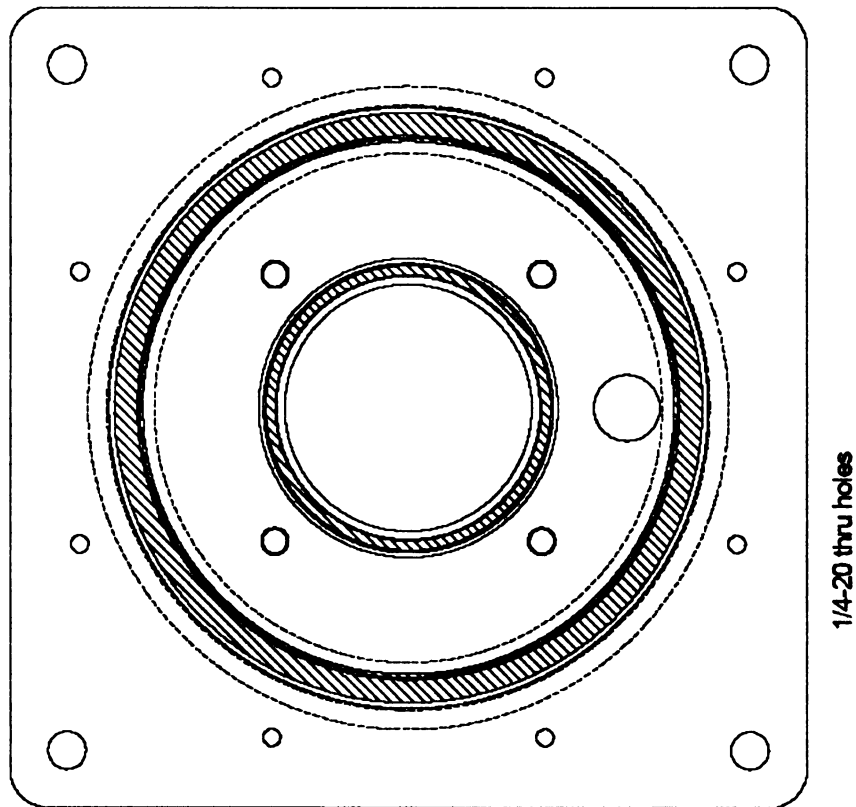
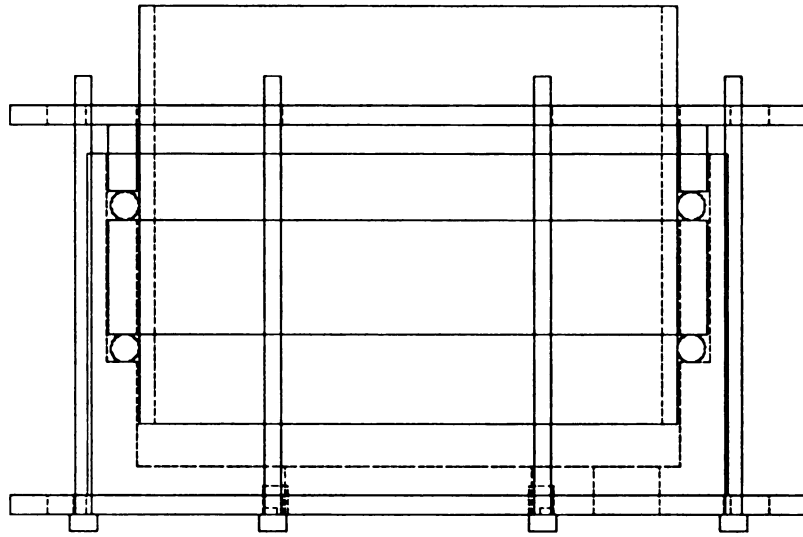


Figure 160. Autosketch of endcap



**Figure 161.** Autosketch of endcaps assembled

## APPENDIX A

### Systems/Components Specifications

This section describes the components that have been used during the research. It is separated into several categories according to the list shown below. Components that relates to vacuum are treated entirely under Vacuum Technology in Section E.

1. Furnace system
2. KrF Excimer Laser
3. Optics

#### 1. Furnace system

The quartz tube was used to house the substrate/target in the furnace system. The inside diameter of the tube was 85mm. Some of the key properties of the quartz tube are good thermal shock and stress resistance, low thermal conductivity, good strength, wear resistant, and most importantly, usable at high temperature. Some other properties are listed below.

**Table 6.** Properties of quartz tube

Density	2.2 g/cm <sup>3</sup>
Thermal Conductivity	1.4 W/mK
Coefficient of Thermal Expansion	5.5 x 10 <sup>-7</sup> /C
Maximum Use Temperature	1683 °C
Manufacturer	Technical Glass Products, Inc

## 2. KrF Excimer Laser

The Lamda Physik LPX 210i KrF Excimer Laser is used to ablate the targets inside the furnace. The specifications for this laser are listed below.

**Table 7.** Specifications for Lamda Physik 210i KrF Excimer Laser

Wavelength (nm)	248
Maximum Repetition Rate (Hz)	100
Pulse Duration (ns)	25
Beam Dimension (mm <sup>2</sup> )	5-12 x 23
Average Power(W)	65

## 3. Optics

The optics used in the experiment comprises of a UV-graded optical materials which includes plano-convex lens, laser mirror, fused silica optics window and Plexiglas beam box.

### a. Plexiglas Beam Box

The purpose of the UV-graded beam box is to protect the researchers during the laser ablation. The specifications are listed below.

Material	UV blocking plexiglas
Dimension (inches)	48 x 7.25 x 14.25

**Table 8.** Beam box specifications

b. Optics Window

Deep UV optics window was used to couple the laser into the furnace system. The specifications are listed below.

Material	Deep UV grade fused silica
Surface Quality	40-20
Wavelength (nm)	0.2 - 2 $\mu\text{m}$
Nominal Flange Diameter	3.7 inches and 2.75 inches
Manufacturer	Insulator-Seal

**Table 9.** Specifications for the optical window

c. Plano-Convex Lens

The round UV-graded fused silica plano-convex lens is used to direct and focus the laser beam onto the target. The specifications are listed below.

**Table 10.** Specification for the plano-convex lens

Material	UV-grade fused-silica
Wavelength (nm)	248
Diameter (inches)	2
Surface Quality	60-40
Manufacturer	Oriel Optics

d. Laser Mirror

The laser mirror was used to redirect the laser beam in the experiment conducted in the furnace system. The specifications are listed below.

Material	UV grade fused silica
Dimension (diameter x thickness)	2 x 0.375 inches
Surface finish	20-10 laser grade polish
Reflectance (248 nm)	> 97% (45°AOI)
Manufacturer	Acton Research Corp

**Table 11.** Specification for the high power UV laser mirror

e. Optical Stand

The two aluminum optics stand was used to support the lens and the mirror. A single piece of the optics stand is shown in Figure. The specifications are listed below.

Material	Aluminum
Dimension (inches)	24 x 2.65

**Table 12.** Specifications for the aluminum optics stand

## **APPENDIX B**

### **Vacuum Technology**

#### **1. Pressure Units**

The System International (SI) pressure unit is Pascal (Pa). It corresponds to  $1 \text{ N/m}^2$ . A unit of pressure unit commonly used is torr, where pressure of one atmosphere at the sea level ( $0^\circ\text{C}$ ) corresponded to 760mm in height of mercury column. The following relationship are used for pressure conversion from one unit to another.

$$1 \text{ torr} = 133.3\text{Pa}$$

$$1 \text{ atm} = 1.013 \times 10^5 \text{ Pa} = 760 \text{ torr}$$

#### **2. Vacuum pump**

The Dry scroll roughing pumps are used to provide the vacuum in the system.

#### **3. Pressure Measurement**

##### **a. Vacuum gauge controller.**

The senTorr<sup>TM</sup> vacuum gauge controller was used to monitor the pressure level inside the system.

##### **b. Thermocouple Gauge**

Thermocouple gauge are rated to measure the pressure in the range of atmosphere down to  $10^{-3}$  torr. In this study, ConvecTorr<sup>TM</sup> thermocouple gauge from Varian is used as shown.



## APPENDIX C

### Germanium Dioxide

Its erythropoietic effect, the possible bacteriocidal or fungicidal effect of organogermanium compounds, prompts the stimulation of the formation of red blood cells (erythrocytes) by injections of  $\text{GeO}_2$ , this was first reported in 1922, raising a series of interest in the treatment of anemia. The effect appears to vary with individuals and with the kind of anemia being treated. Moreover, the curing results are merely temporary. In all cases, the effect is less evident than with repeated small doses of arsenic trioxide. Nonetheless, the consequent danger of poisoning also is comparatively less. Based on the hypothesis that the low solubility of  $\text{GeO}_2$  in water might be blamed for the marginal and inconsistent results, higher levels of germanium in the form of the highly soluble dimethylgermanium oxide were administered to hamsters. While these demonstrated the non-toxic behavior of  $(\text{CH}_3)_2\text{GeO}$ , the effect on erythrocyte levels was inconclusive.

## APPENDIX D

### Buffer Etches

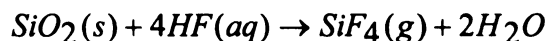
To fabricate the windows through the oxide layer, a standard lithography technique was used. A positive photoresist (Shipley 1813) was used, followed by a buffered hydrofluoric acid etch of the  $\text{SiO}_2$  film to open windows through the oxide layer to the silicon substrate.

It is important to note that  $\text{SiO}_2$  is an amorphous material, which etches equally well in all directions, exhibiting isotropic etching. In other words, when an oxide etch depth of 1nm is required, a lateral etch of 1nm will also occur. Furthermore, the thickness of any subsequently deposited layer is directly impacted by the wall shape and slope angle of the etched  $\text{SiO}_2$ . The controllable parameters in wet etching are time, temperature, solution concentration, and solution recirculation.

The etching mechanism of  $\text{SiO}_2$  has been described by Prigongine, et al. as follows:

- |      |  |
|------|--|
| I.   | Protons are adsorbed to oxygen on the surface featuring the strongest basicity, which functions as the proton acceptor.  |
| II.  | Oxygen which adsorbs the proton needs the valence electron.  |
| III. | Oxygen obtains the valence electron from neighboring silicon which has many electrons.   |
| IV.  | As silicon gives the valence electron to oxygen, the electron density around silicon decreases. Consequently the silicon-oxygen bond gets weaker, and the bond is eventually broken. |

- V. When the silicon-oxygen bond is broken, silicon becomes positive.
- VI. As a result,  $\text{HF}_2^-$  is coordinated to facilitate etching.



Hydrogen fluoride (HF) is rarely used at full strength because of the consequent high etch rate, which is difficult to control. In our experiment, we used 1:8 HF to ammonium fluoride ( $\text{NH}_4\text{F}$ ).

In a study of various dilute HF solutions, in which  $\text{NH}_4\text{F}$  was used as a buffering agent, Judge used the conditions and constants described by Mesmer and Baes to determine the effect of the solution composition on the etch rate of undoped  $\text{SiO}_2$ . The results of this study are presented in Table 13.

**Table 13.** Calculated Concentrations and Associated Etch Rates.

Calculated Concentrations				$\text{SiO}_2$	<i>Etch</i>
				<i>Rate</i>	
$M \times 10^3; T = 25^\circ\text{C}$				$^\circ/\text{min}$	
$[\text{HF}]$	$[\text{HF}_2^-]$	$[\text{F}^-]$	$[\text{H}^+]$		
13	87	677	0.0255	44.34	

41	159	409	0.129	87.12
81	189	242	0.435	112.26
109	191	182	0.778	124.08
175	173	102	2.24	133.92
266	128	49.4	7.01	118.26

Using  $\text{NH}_4\text{F}$  to dilute the etchant is common in the semiconductor industry and is frequently termed Buffered Oxide Etch (BOE). Parisi and his coworkers found that the activation energy for the dissolution of  $\text{SiO}_2$  in BOE solutions was 9.9 kcal/mole. Furthermore, based on their empirical results, they determined that the depth etch rate ( $\gamma$ ) could be approximated by the following rate equation:

$$\gamma = 4.5 \times 10^9 [\text{HF}] \exp(-4980/T)$$

where  $\gamma$  is in angstroms per minute,  $[\text{HF}]$  is the molar concentration of HF, and  $T$  is the absolute temperature in degrees Kelvin. This equation is valid for etchant solutions with molar concentrations of HF between 0.9 and 3.8 moles per liter and within the temperature range of 25 to 55° C.

The taper of the resulting slope is a function of the depth etch rate and the lateral etch rate ( $\gamma_e$ ). The angle  $\theta$  that the taper forms with the wafer surface is given by

$$\sin \theta = \gamma / \gamma_e$$

A variety of factors have a direct influence on the lateral etch rate. These factors include the type of the photoresist used and the condition of the exposed

oxide/photoresist interface prior to the etching. In addition, if a wetting agent is used, a correlation between the lateral etch rate and the HF concentration or temperature cannot be precisely defined, given the variety of influences on this etch rate. However, it has been discovered that the edge profiles of the taper follow the trend of increasing with higher molarity.

## References

- 1 Published in the February 1960 issue of Caltech's *Engineering and Science*, and available at <http://www.zyvex.com/nanotech/feynman.html> (09/06/2005).
- 2 An excellent summary of many research efforts can be found at:  
<http://www.nano.gov/html/research/rnews.html> (09/06/2005).
- 3 B. Messer, J. H. Song, and P. Yang, "Microchannel Networks for Nanowire Patterning," *J. Am. Chem. Soc.*, vol 122, pp 10232-10233, July 2000.
- 4 C. M. Lieber, "One-Dimensional Nanosturctures: Chemistry, Physics & Applications", *Solid State Communications*, vol 107, pp 607-616, 1998.
- 5 Y. Liu, K. Ishii, T. Tsutsumi, M. Masahara, T. Sekigawa, K. Sakamoto, H. Takashima, H. Yamauchi, and E. Suzuki, "Systematic Electrical Characteristics of Ideal Rectangular Cross Section Si-Fin Channel Double-Gate MOSFETs Fabricated by a Wet Process," *IEEE Transactions on Nanotechnology*, vol. 2, no. 4, pp. 198-204, 2003.
- 6 Givargizov, E. I., "Growth of whiskers by the vapor-liquid-solid mechanism," In E. Kaldis, Ed., *Current Topics in Materials Science*, vol. 1, pp. 79-145, 1978.
- 7 A recent definition of nanotechnology is "Nanotechnology is the understanding and control of matter at dimensions of roughly 1 to 100 nanometers, where unique phenomena enable novel applications. Encompassing nanoscale science, engineering and technology, nanotechnology involves imaging, measuring, modeling, and manipulating matter at this length scale. At the nanoscale, the physical, chemical, and biological properties of materials differ in fundamental and valuable ways from the properties of individual atoms and molecules or bulk matter. Nanotechnology R&D is directed toward understanding and creating improved materials, devices, and systems that exploit these new properties." This definition can be found at :  
<http://www.nano.gov/html/facts/whatIsNano.html> (10/03/05).
- 8 M. H. Dvoret, D. Esteve, and C. Urbina, "Single-electron transfer in metallic nanostructures" *Nature*, vol. 360, pp. 547, 1992.

- 9 A. P. Alivisatos, "Semiconductor Clusters, Nanocrystals, and Quantum Dots" *Science*, vol. 271, pp 933, 1996.
- 10 B. Gilbert, F. Huang, H. Zhang, G. A. Waychunas, and J. F. Banfield, "Nanoparticles: Strained and Stiff." *Science* 305: 651-654, 2004.
- 11 M. A. Ratner and D. Ratner, "Nanotechnology," Prentice Hall PTR, Nov. 8 2002.
- 12 X. Duan, Y. Huang, R. Agarwal and C. M. Lieber, "Single-Nanowire Electrically Driven Lasers," *Nature* 421, 241-245 (2003).
- 13 M. Law, J. Goldberger, and P. Yang, "Semiconductor nanowires and nanotubes," *Annu. Rev. Mater. Res.* Vol. 34, pp. 83-122, 2004.
- 14 L.D. Hicks and M.S. Dresselhaus, *Phys. Rev. B* 47, p. 12727, 1993.
- 15 Y.-M. Lin and M.S. Dresselhaus, *Phys. Rev. B* 68, 075304, 2003.
- 16 H. J. Dai, E. W. Wong, Y. Z. Lu, S. S. Fan, and C. M. Lieber, "Synthesis and Characterization of Carbide Nanorods" *Nature*, Vol. 375, pp769, 1995.
- 17 J. Hu, T. W. Odom, and C. M. Lieber, "Chemistry and Physics in One Dimension: Synthesis and Properties of Nanowires and Nanotubes" *Acc. Chem. Res.* Vol. 32 pp 435, 1999.
- 18 H. Namatsu, Y. Watanabe, K. Yamzaki, T. Yamaguchi, M. Nagase, Y. Ono, A. Fujiwara, and S. Horiguchi, "Fabrication of Si single-electron transistors with precise dimension by electron-beam nanolithography," *J. Vac. Sci. Technol. B*, Vol. 21, (1), Jan/Feb 2003.
- 19 X. Duan, and C. M. Lieber, "General synthesis of compound semiconductor nanowires," *Advanced materials*, Vol. 12, No. 4, pp298-302, 2000.
- 20 R. S. Wagner, W. C. Ellis, "Vapor-Liquid-Solid Mechanism of Single Crystal Growth," *Applied Physics Letters*, vol. 4, no. 5, pp. 89-90, 1964.

- 21 J. Westwater, D. P. Gosain, S. Usui, "Si Nanowires Grown via the Vapour-Liquid-Solid Reaction," *Physica Status Solidi. A*, vol. 165, pp. 37-42, 1998.
- 22 E. I. Givargizov, A. N. Stepanova, L. N. Obolenskaya, E. S. Mashkova, V. A. Molchanov, M. E. Givargizov, I. W. Rangelow, "Whisker Probes," *Ultramicroscopy*, vol. 82, pp. 57-61, 2000.
- 23 I. W. Rangelow, F. Shi, P. Hudek, P. Grabiec, B. Volland, E. I. Givargizov, A. N. Stepanova, L. N. Obolenskaya, E. S. Mashkova, and V. A. Molchanov, "Micromachined ultrasharp silicon and diamond-coated silicon tip as a stable field-emission electron source and a scanning probe microscopy sensor with atomic sharpness," *Journal of Vacuum Science and Technology B*, vol. 16, no. 6, pp. 3185-3191, 1998.
- 24 J. Hu, T. W. Odom, C. M. Lieber, "Chemistry and Physics in One Dimension: Synthesis and Properties of Nanowires and Nanotubes," *Accounts of Chemical Research*, vol. 32, no. 5, pp. 435-445, 1999.
- 25 E. I. Givargizov, "Growth of Whiskers by the Vapor-Liquid-Solid Mechanism," Chapter 3 in *Current Topics in Materials Science*, Volume 1, ed. E. Kaldis, north-Holland Publishing Company, 1978.
- 26 R.-Q. Zhang, Y. Lifshitz, S. T. Lee, "Oxide-Assisted Growth of Semiconducting Nanowires," *Advanced Materials*, vol. 15, no. 7-8, pp. 635-640, 2003.
- 27 *Fundamentals of Semiconductor Processing Technology*, Badih El-Kareh, pp. 142
- 28 *Fundamentals of Microfabrication*, M. J. Madou, CRC Press, Mar. 13, 2002.
- 29 *Handbook of Physical Vapor Deposition (PVD) Processing*, D. M. Mattox, William Andrew Inc., Mar. 1. 1998.
- 30 *Handbook of Nanophase and Nanostructured Materials*, Z. L. Wang, Y. Liu, and Z. Zhang, Springer, pp204, 2002.
- 31 *Pulsed Laser Deposition of Thin Films*, ed. D. B. Chrisey and G. K. Hubler, New York, John Wiley & Sons, Inc, 1994.



- 32 [http://www.photonics.cusat.edu/Research\\_Laser%20Induced%20Plasma.html](http://www.photonics.cusat.edu/Research_Laser%20Induced%20Plasma.html)  
(as 10/03/05)
- 33 *Pulsed Laser deposition of thin films*, D. B. Chrisey. Chap. 6.
- 34 *Phase transformations in Metals and Alloys*, D.A. Porter.
- 35 R. S. Wagner, W. C. Ellis, "Vapor-Liquid-Solid Mechanism of Single Crystal Growth," *Applied Physics Letters*, vol. 4, no. 5, pp. 89-90, 1964.
- 36 E. I. Givargizov, "Fundamental Aspects of VLS Growth," *Journal of Crystal Growth*, vol. 31 pp20-30, 1975.
- 37 J. Westwater, D. P. Gosain, S. Tomiya, S. Usui, and H. Ruda, "Growth of Silicon nanowires via gold/silane vapor-liquid-solid reaction," *Journal of vacuum science & Technology B*, vol. 15, no. 3, pp. 554-557, 1997.
- 38 B. Bokhonov, and M. Korchagin, "In situ investigation of stage of the formation of eutectic alloys in Si-Au and Si-Al systems," *Journal of Alloys and compounds*, vol. 312, pp 238, 2000.
- 39 N. Wang, Y. H. Tang, Y. F. Zhang, C. S. Lee, I. Bello and S. T. Lee, "Si nanowires grown from silicon oxide," *Chemical Physics Letters*, Vol. 299, Issue 2, pp 237-242, Jan. 1999.
- 40 Rui-Qin Zhang, Yeshayahu Lifshitz, Shuit-Tong Lee, "Oxide-Assisted Growth of semiconducting Nanowires," *Advanced materials*, 15, no.7-8, April 17, 2003.
- 41 N.-G Ma, C.-J. Deng, P. Yu, M. Aravind, and D. H. L. Ng, "Formation of MgO Nanorods in the reaction zone of a Mg-CuO powder mixture by *in-situ* reaction," *Philosophical Magazine*, Vol. 84, No. 1, pp 69-80, Jan. 2004.
- 42 P. Gao and Z. L. Wang, "Self-Assembled Nanowire-Nanoribbon Junction Arrays ZnO," *The journal of physical chemistry B*, Vol. 106, Num. 49, pp12653-12658, Dec. 2002.

- 43 *The science and engineering of microelectronic fabrication*, S. A. Campbell, Oxford university press, 2001.
- 44 X. Duan and C. M. Lieber, "Synthesis and optical properties of gallium arsenide nanowires," *Applied Physics Letters*, Vol. 76, pp. 1116-1118, 2000.
- 45 J. Hu, T. W. Odom, and C. M. Lieber, "Chemistry and Physics in One Dimension: Synthesis and Properties of Nanowires and Nanotubes," *Acc. Chem. Res.*, Vol. 32, pp.435-445, 1999.
- 46 X. Duan and C. M. Lieber, "Laser-Assisted Catalytic Growth of Single Crystal GaN Nanowires," *J. Am. Chem. Soc.*, vol. 122, pp. 188-189, 2000.
- 47 W. S. Shi, Y.F. Zheng, N. Wang, C.S. Lee, and S. T. Lee, "Synthesis and microstructure of gallium phosphide nanowires," *J. Vac. Sci. Technol. B*, Vol. 19, pp.1115-1118, 2001.
- 48 C. T. Tsai, and R. S. Williams, "Solid phase equilibria in the Au-Ga-As, Au-Ga-Sb, Au-In-As, and Au-In-Sb ternaries," *J. Mater. Res.*, Vol. 1, Num. 2, Mar/Apr 1986
- 49 M. B. Panish, *J. Electrochem. Soc.* Vol. 114, pp517, 1967.
- 50 J. R. Arthur, "Surface stoichiometry and structure of GaAs," *Surface Science*, Vol. 43 num. 2, pp449-461, 1994.
- 51 Y. Zhang, P. L. Lee, G. S. Nolas, and A. P. Wilkinson, "Gallium Distribution in the clathrates  $\text{Sr}_8\text{Ga}_{16}\text{Ge}_{30}$  and  $\text{Sr}_4\text{Eu}_4\text{Ga}_{16}\text{Ge}_{30}$ ", *Applied Physics Letters*, Vol. 80, pp2931-2933, 22 April, 2002.
- 52 K. Saito and A. J. Ikushima, "Reduction of light-scattering loss in silica glass by the structural relaxation of "frozen-in" density fluctuations", *Appl. Phys. Lett.*, vol. 70 (26), pp.3504-3506, June 1997.
- 53 P. Patnaik, *Handbook of inorganic chemicals*, New York : McGraw-Hill, c2003

- 54 J. C. Bailar, Jr., H. J. Emeléus, Sir Ronald Nyholm and A. F. Trotman-Dickenson, *Comprehensive inorganic chemistry*, Pergamon Press; distributed by Compendium Publishers [Elmsford, N.Y., 1973]
- 55 Z.G. Bai, D.P. Yu, H.Z. Zhang, Y. Ding, Y.P. Wang, X.Z. Gai, Q.L. Hang, G.C. Xiong, and S.Q. Feng, "Nano-scale  $GeO_2$  wires synthesized by physical evaporation", *Chemical physics letters*, vol. 317, pp504-509, Feb. 2000.
- 56 P. Hidalgo, B. Mendez and J. Piqueras, " $GeO_2$  nanowires and nanoneedles grown by thermal deposition without a catalyst", *Nanotechnology*, vol. 16, pp2521-2524, Sep. 2005.
- 57 Y. Zhang, J. Zhu, Q. Zhang, Y. Yan, N. Wang, and X. Zhang, "Synthesis of  $GeO_2$  nanorods by carbon nanotubes template", *chemical physics letters*, vol. 317, pp. 504-509, Feb. 2000.
- 58 Y. H. Tang, Y. F. Zhang, N. Wang, I. Bello, C. S. Lee, and S. T. Lee, "Germanium dioxide whiskers synthesized by laser ablation", *Applied physics letters*, vol. 74 (25), pp. 3824-3826, Feb. 1999.
- 59 H. Y. Dang, J. Wang, and S. S. Fan, "The synthesis of metal oxide nanowires by directly heating metal samples in appropriate oxygen atmospheres", *Nanotechnology*, vol. 14, pp738-741, May 2003.
- 60 J.-Q. Hu, Q. Li, X.-M. Meng, C.-S. Lee, and S.-T. Lee, "Synthesis and nanostructuring of patterned wires of  $GeO_2$  by thermal oxidation", *Advanced materials*, vol. 14, no. 19, pp1396-1399, Oct. 2002.
- 61 X. C. Wu, W. H. Song, B. Zhao, Y. P. Sun, and J. J. Du, "Preparation and photoluminescence properties of crystalline  $GeO_2$  nanowires", *Chemical physics letters*, vol. 349, pp210-214, Oct. 2001.
- 62 K. Prabhakaran, and T. Ogino, "Oxidation of Ge(100) and Ge(111) surfaces: an UPS and XPS study," *Surface Science*, vol. 325, pp.263-271, 1995.
- 63 R. B. King., *Encyclopedia of inorganic chemistry*, Chichester ; New York : Wiley, c1994.

- 64 C.A. Jacobson, *Encyclopedia of chemical reactions*, New York, Reinhold Pub. Corp., 1946-59.
- 65 R.S. Wager, and W.C. Ellis, "Vapor-liquid-solid mechanism of single crystal growth," *Applies physics letters*, vol. 4, pp89-90, March 1964.
- 66 A. P. Levitt, *Whisker technology*, New York, Wiley-Interscience 1970.
- 67 K. Haraguchi, K. Hiruma, T. Katsuyama, K. Tominaga, M. Shirai, and T. Shimada, "Self-organized fabrication of planar GaAs nanowhisker arrays", *Appl. Phys. Lett.*, Vol. 69, pp 386-387, 1996.
- 68 K. Haraguchi, K. Hiruma, K. Hosomi, M. Shirai, and T. Katsuyama, "Growth mechanism of planar-type GaAs nanowhiskers", *J. Vac. Sci. Technol. B*, Vol. 15, pp 1685-1687, 1997.
- 69 M. S. Islam, S. Sharma, T. I. Kamins, and R. S. Williams, "Ultrahigh-density silicon nanobridges formed between two vertical silicon surfaces", *Nanotechnology*, Vol. 15, pp L5-L8, 2004.
- 70 W. U. Wang, C. Chen, K.-H. Lin\*, Y. Fang\*, and C. M. Lieber, "Label-free detection of small-molecule-protein interactions by using nanowire nanosensors", *Perceedings of the National Academy of Sciences of the united States of America*, Vol. 102, pp3208-3212, 2005.
- 71 Y. Cui, and C. M. Leber, "Functional Nanoscale Electronic Devices Assembled Using Silicon Nanowire Building Blocks", *Science*, Vol. 291, pp 851-853, 2001.
- 72 *Scanning and Transmission Electron Microscopy*, S. L. Flegler, J. W. Heckman, Jr, and K. L. Klomparens, New York, Oxford University Press 1993.

MICHIGAN STATE UNIVERSITY LIBRARIES



3 1293 02845 1452